SLAC – PUB – 3561
CALT – 68 – 1015
January 1985
(M)

PROPOSAL FOR THE MARK II AT SLC*

SLAC COLLABORATION

Stanford Linear Accelerator Center
Stanford University, Stanford, California, 94305

Caltech – LBL – U.C. Santa Cruz – University of Colorado
– University of Hawaii – Johns Hopkins University
– University of Michigan
Collaboration

Submitted for Publications

---

* Work supported in part by the Department of Energy, contract DE-AC03-76SF00515.

Abstract

This proposal represents a planning document for upgrading the Mark II as the first detector for SLC. We review the physics potential, plans for upgrade of the detector, the expected performance, schedule, and budgets.

We expect the plans will evolve and change. This document should be viewed as our best present knowledge of all the various aspects of this project of developing the Mark II into the first detector for SLC.

Table of Contents

1. Overview

We propose in this document a plan for upgrading the Mark II to become the first detector for the SLAC Linear Collider. This upgrade is built on a large amount of existing and well proven hardware and software as well as a great deal of experience at SPEAR and PEP.

The proposed upgrades are specifically designed to meet the requirements to exploit the exciting Z° physics that will be available at SLC. The key to our plan for this upgrade are the following requirements: (1) the upgraded detector (Mark II/SLC) will be sufficiently powerful and general to make a full study of Z° physics as well as search for unexpected new phenomena, and (2) the essential upgrades will have benefited from a year of checkout and data taking at PEP.

Before discussing the Mark II/SLC, it is useful to give a brief discussion of the desirable properties of a detector to be used in an early exploration of Z° physics at the SLC.

The physics which we consider as the natural domain of such a detector would encompass the following areas: (1) Measurement of Z° mass and width and determination of the number of light neutrinos, (2) Tests of standard model electroweak predictions in dilepton ($e^+e^-,\mu^+\mu^-,\tau^+\tau^-$) final states, including τ polarization, (3) Search for t-quarks (if as yet undiscovered), (4) Search for Higgs via the decay $Z^\circ \rightarrow l^+l^-H^\circ$, (5) QCD tests via multi-jet studies, (6) Search for new or unexpected phenomena beyond the standard model.

The most essential capabilities for a detector which could reasonably attack the above problems would include the following: (i) charged particle tracking with adequate resolution and solid angle, (ii) electromagnetic calorimetry with sufficient energy resolution, segmentation, and solid angle (iii) ability to separate and measure energies of electrons or muons or preferably both in the midst of large hadronic components, (iv) overall flexibility and measurement capabilities to recognize new phenomena. (v) precision vertex measurement capability.

We now discuss these in just a little more detail:

(i) As emphasized in the SLC Workshop Report [1.1]. Charged particle tracking with a precision σ_p/p of better than 0.5p% is desirable over a solid angle close to 90% of 4π. Pattern recognition must be adequate to give high tracking efficiency.

(ii) Energy resolution in the electromagnetic calorimeter of about $0.15/\sqrt{E}$ is desirable for τ polarization, Higgs detection and neutrino counting (via $e^+e^-\to\gamma\nu\bar{\nu}$) experiments. Good segmentation (<40 mr) and a large solid angle are also important.

(iii) Lepton identification for tracks in hadronic events with hadron rejection at the level of better than 1/100 is required for the Higgs search and for the t-quark search. Lepton identification in the midst of multi-jet events, which can provide valuable handles on flavor identification, requires hadron rejection at the level of 1/500 or better.

(iv) The search for new phenomena makes desirable such capabilities as velocity measurements to tag very slow particles, flexibility with respect to charged and neutral triggers, and large solid angle for both tracking and calorimetry to avoid missing significant charged or neutral particles in unusual events.

(v) Precision vertex measurement to permit detection of very short flight paths is a capability which would match especially well the SLC interaction region properties, and would help provide flavor identification of heavy quark jets, and improved lifetime measurement of hadrons with b quarks. For the efficient recognition of D decay products an impact parameter error of about 20μm or less in the extrapolation of a track to the beam line is required. If confidence about technology and backgrounds permitted it, one would want to have such a device as early as possible in the SLC operation.

1.1 The Detector (Mark II/SLC)

The Mark II detector upgraded for SLC is shown in figures 1.1 and 1.2. The primary components are briefly discussed below and more completely in Section 3.

(1) A conventional solenoid provides a field of at least 5kG. A new coil to replace the present coil which shorted in 1982 will be installed during summer 1984. A new motor driven door system will allow access to detector components and the occluded portions of the beam line.

(2) A new cylindrical drift chamber, based on a multi-sense-wire cell structure, capable of meeting the tracking requirements for SLC will be installed in summer 1984. With vertex constraint, precision σ_p/p^2 of 0.12% GeV^{-1} is achieved over 65% of 4π solid angle. In addition, pulse height measurement of the sense wire signals will provide dE/dx measurements.

(3) Electromagnetic calorimetry will be provided over the angular range $\cos\vartheta < 0.7$ by the present octagonal array of finely segmented liquid argon modules.The forward region will be covered by a new set of end cap calorimeters This 36 layer, Pb/proportional tube chamber is expected to give $\sigma/E \approx 18\%/\sqrt{E}$ for $1 \text{ GeV} \leq E \leq 50$ GeV.

(4) A new time of flight system segmented into 96 scintillators will be installed at a radius of 1.5 m. A nominal resolution of ~ 200 picoseconds or better should be obtained.

(5) Muon identification is provided by a system of steel absorbers followed by layers of proportional tubes, the system covering 55% of 4π.

HORIZONTAL CROSS SECTION

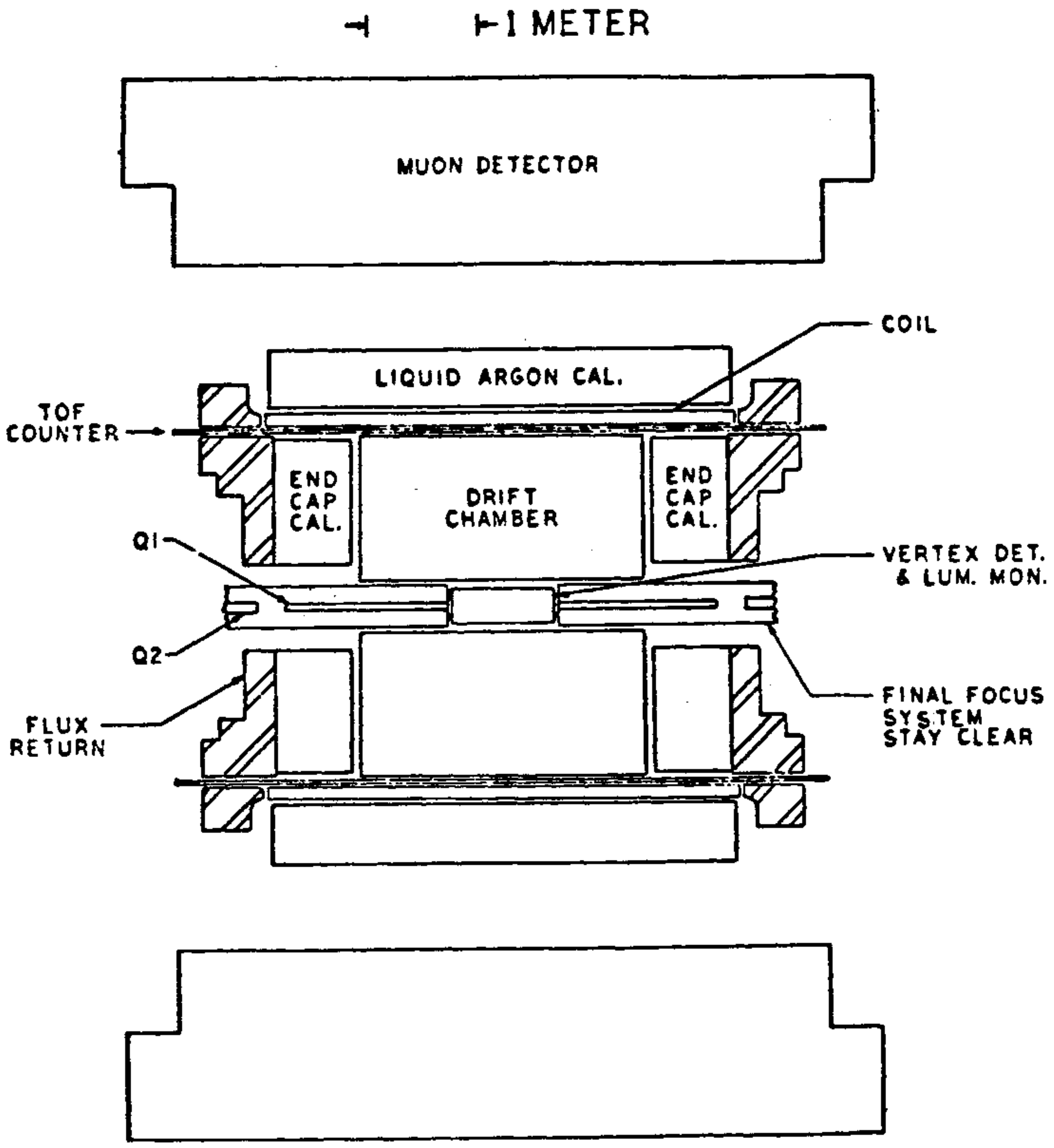

Figure 1.1 Plan view of the Mark II detector for SLC.

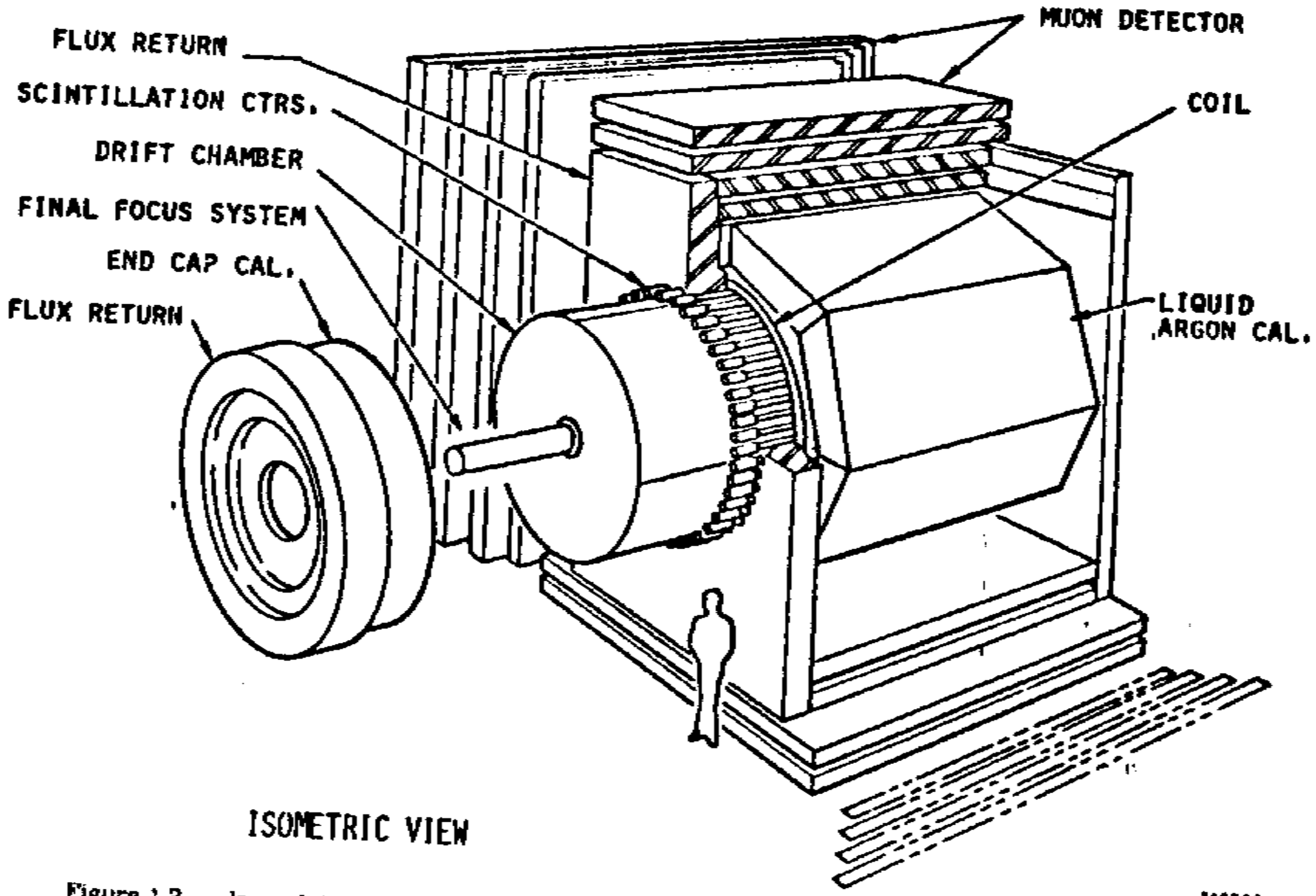

Figure 1.2 Isometric view of the Mark II detector for SLC

(6) A precision vertex detector will be employed at SLC and various options are under study.

(7) A small angle monitor system will be used to determine the luminosity and to remove backgrounds in the neutrino counting experiment.

In addition to these detector components, the primary and secondary triggers are variable input, programmable devices which can accommodate a considerable amount of information from various detector components to provide a very flexible capability. In terms of data analysis, there is a fully developed system of off-line software for data reduction, event reconstruction, analysis and Monte Carlo simulation.

The major features of the upgrade are the construction of a new drift chamber and of new endcap calorimeters. This will involve the use of existing, proven techniques so as to ensure that we can achieve our goals and also to meet the time constraints associated with a meaningful checkout at PEP followed by a timely arrival at SLC. The improvements over the present PEP tracking capability will consist of (1) better momentum resolution for high energy tracks through more sense-wire layers and somewhat greater radial tracking distance, (2) improved pattern recognition through multi-hit electronics and careful cell design and (3) dE/dx measurement capability through appropriate cell design and electronics principally to provide substantial electron-hadron separation over and above that provided by the calorimetry. The implementation of new endcap shower counters, along with the existing liquid argon barrel counters, will provide good electromagnetic calorimetry over nearly the complete solid angle.

In addition to these major improvements, we also propose to replace the TOF system with a new set of scintillators, light pipes, etc. with twice the azimuthal granularity. This upgrade is motivated by the increased multiplicity at SLC and the deteriorated performance of the present system.

Finally, we propose the construction of two devices especially for SLC operation. These will be designed and built on that time scale and are (i) a small angle monitor (SAM) for luminosity measurement and (ii) a precision vertex detector properly matched to SLC for tagging of short-lived particles.

1.2 The SLC INTERACTION REGION

We have spent considerable effort investigating the requirements for the SLC IR as they pertain to the Mark II. The main thought to bear in mind is that the first detector at the SLC must maintain, as closely as possible, the configuration which it had at PEP. If this is violated then the notion of a PEP tested device can easily evaporate. In addition, every effort must be made to permit a rapid and trouble-free installation because the idea that the first detector be late for usable SLC collisions is unacceptable. Priority in the SLC IR design must be given to the first detector to ensure these objectives are met. In particular, remembering the difficult PEP experience, the IR must be completed in a timely fashion.

When we speak of the SLC IR, we think of the area which encompasses the experimental service pads, the counting house and the floor space for the detector (on-line and off-line locations). In the case of the SLC all but the floor space for the detector reside at the local ground level; the IR pit is 17 m below this local ground level. This means that the mounting of the installation is done 17 m above the installation area itself and this presents very different problems than we are accustomed to.

The present IR design is shown in Fig. 1.3. We use this present design as a means of illustrating our specific needs. The pit has two garages—the off beam line positions—and one on beam line slot. The notion here is a push-pull situation. The first question which arises is who goes in which location? We have looked into this and find that for ease and speed of installation the west pit is clearly superior. These being important criteria, we argue strongly for this choice.

There are many compelling reasons why the LEACH at the SLC should maintain the same position relative to the detector as it has at PEP. The cable plant

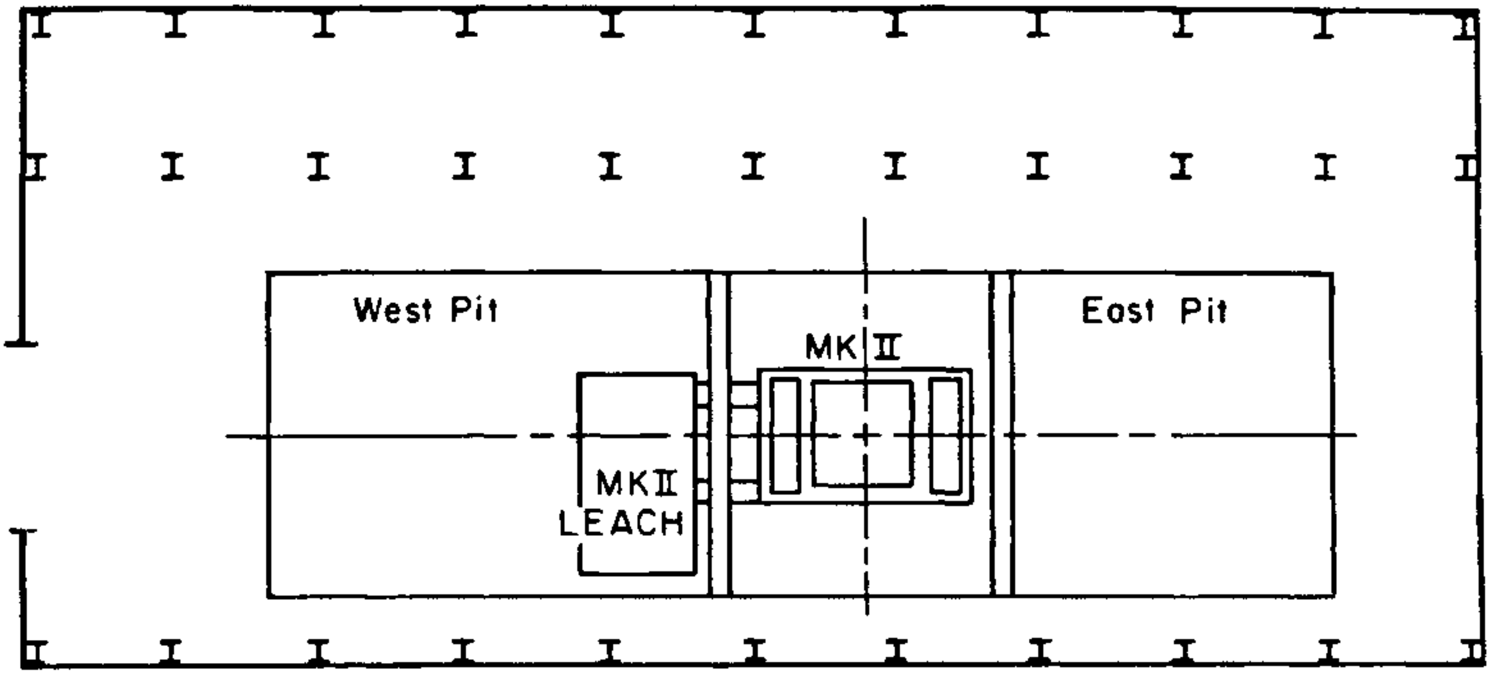

(a) "IN" POSITION

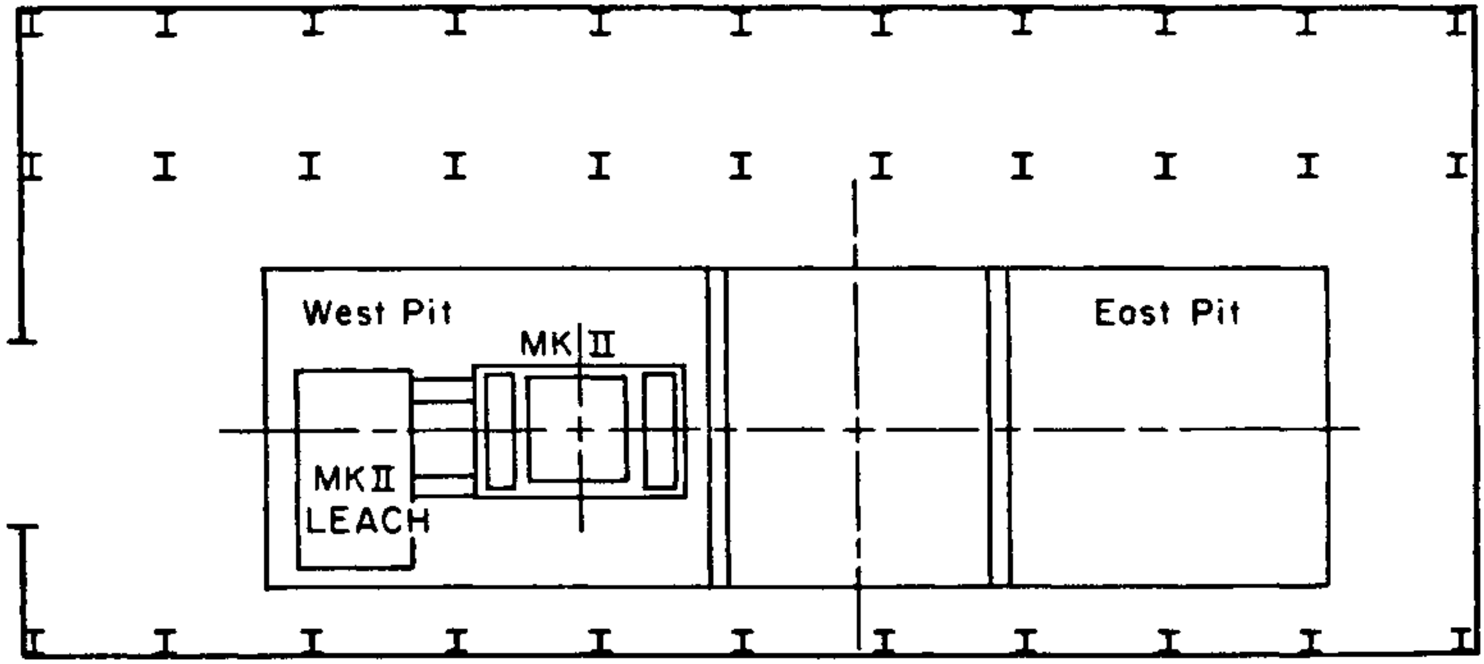

(b) "OUT" POSITION

Figure 1.3 The SLC pit with the Mark II detector and LEACH.

can remain identical if this is done. There is a platform above the LEACH which provides, amongst other things, cryogenic servicing for the detector. If the LEACH/detector orientation is preserved, this cryogenic plant can be transferred, without modification, to the SLC. The cryogenics group has estimated that replacing this cryogenics plant would cost $250K. These examples plus the desire for a smooth and timely installation convinces one quickly that the present LEACH/detector orientation should be preserved.

The argon dewar from which we fill the liquid argon counters must be placed at the pit floor level. The problem with placing it 17 m above the device is that (a) the modules are not protected against a liquid head of that magnitude and (b) emptying the modules will require pumping of the liquid against the 17 m head. The cryogenics group has recommended strongly that these worrisome problems be avoided.

The pit floor space required by the Mark II is shown in Fig. 1.3. The transverse size of the garage (23 m) is determined by the preservation of the present LEACH/detector orientation. The longitudinal size of the IR pit (17 m) is determined by the space required for the extraction, if needed, of either the central section of beam pipe or the central detector package (coil, drift chamber and TOF counters). The detector is shown both in the in (a) and out (b) positions.

The crane capacity required for the installation is 50 tons. During normal operation a 5 ton capacity would be adequate. In all likelihood, we will install the Mark II at the same time as installation is proceeding on the second detector. Sharing a crane under these circumstances will slow down the installation considerably and we recommend that there be two 25-ton cranes running on the same rails. This will afford the possibility of a 50 ton lift if it is ever needed. The apron on the west side from which the installation is mounted should be at least

10 m in transverse extent. The counting house space required is the same as at PEP where we have a two story building, each story having about 110 m^2 of floor space. The lower floor houses the computer, and the control center for the experiment and the cryogenics. The upper level has an electronics test setup, work benches, a conference room, and toilet facilities. There seems no reason to change substantially from this successful setup--certainly we could not live comfortably with less than 100 m^2 per floor.

This covers the major issues associated with the SLC IR hall. We emphasize again that attention should be given to these requests so that the Mark II can arrive at the SLC on time as a timely, PEP checked-out device.

2. Physics Motivation

We propose to upgrade the Mark II detector as the first detector for SLC, motivated by the rich physics that will be available in the region of the Z°. We are dedicated to being ready to do the early physics, as soon as the usable luminosity is attained, and, in addition, will have the capability in the Mark II to do much of the physics requiring both larger luminosity and more sophistication in a detector.

The physics potential of the SLC has been reviewed in depth in the proceedings of the SLC Workshop [1.1] and elsewhere. Rather than review that physics here, we comment briefly on several areas that are likely to have high priority in early running at SLC, and in addition, give more detailed discussions of a few physics topics that illustrate the capabilities of the Mark II detector.

2.1 Measurement of Z° Mass and Width

Achievement of good measurements of mass and total width of the Z° depends more on monitoring and controlling of the SLC machine parameters and on the availability of a good measurement of luminosity than they do on the detailed properties of the detector. The interpretation of the total Z° width in terms of neutrino generations, however, also requires careful measurement of the branching fractions of the Z° into (i) quark pairs, (ii) charged lepton pairs, and (iii) any fundamental objects, other than quarks and leptons, which also give rise to charged particles. It is only after one fully understands all contributions to the Z° width from states containing charged secondaries that one can hope to establish the contribution from neutrino generations. The identification of these various contributions in itself leads to important physics issues which are discussed.

2.2 Studies of Charged Lepton Pairs

Studies of the angular distributions, asymmetries, and polarizations of final-state charged lepton pairs provides some of the most direct tests of the standard Weinberg-Salam model of weak interactions. Measurements of these quantities provide information on the Z° couplings to the various lepton pairs. The availability of longitudinally polarized electrons at the SLC will provide further information through the measurement of longitudinal asymmetries. For electron and muon pairs, momentum resolutions based on the tight vertex constraints are applicable (dashed curve in Fig. 3.3a). This implies a momentum resolution of better than 6% for each track for 65% of 4π, reducing to 20% at $\cos\vartheta = 0.85$. For the tau pairs, the finite decay length requires a looser vertex cut (dot-dashed curve in Fig. 3.3). However, because of the lower momenta of the charged tau secondaries, momentum resolution remains good. Coverage with electromagnetic calorimetry over 90% of 4π allows good separation of e^+e^- from $\mu^+\mu^-$. The angular resolutions which lead to p_t errors of ~50 MeV/c over 90% of 4π allow straightforward separation to $\tau^+\tau^-$ from e^+e^-, $\mu^+\mu^-$.

To relate these numbers to physics issues we give one example. Consider the measurement of V_μ/A_μ through determination of the longitudinal asymmetry A_L of dimuon production for the case that an electron polarization is ± 0.5. We integrate over events with negative muons in the forward hemisphere (SLAC-247, pp. 30-31). For 10^4 total $Z^\circ \to \mu^+\mu^-$ events distributed equally among the two electron polarizations, we would obtain $\sigma(V_\mu/A_\mu) = 0.022$ for a perfect detector with 4π solid angle, and $\sigma(V_\mu/A_\mu) = 0.032$ for our proposed detector which has $(\cos\vartheta)_{\max} = 0.85$.

The shape of the pion momentum spectrum from the $\tau^\pm \to \pi^\pm\nu$ decay mode is such that it is possible to measure the τ polarization. The momentum resolution is sufficient for this measurement ($\sigma_p/p^2 = 0.5\%$ GeV^{-1} is required), and the electromagnetic calorimetry, dE/dx, and muon system will separate other τ decay modes from the single pion final state (about 50:1 rejection of leptons is required).

New sequential charged leptons of mass less than $m_z/2$ will be readily identifiable through the detection of noncollinear $e^{\pm}\mu^{\mp}$ pairs. The main geometrical restriction is the 55% of 4π coverage of the muon system. This search procedure has already successfully been used with the Mark II at PEP to set lower limits to the mass of any new sequential lepton above 13 GeV/c^2. In summary, the upgraded Mark II will be very well matched to the requirements of the lepton pair physics at the Z°.

2.3 QCD Tests and Multijet Analysis

The study of quark and gluon jets from Z° decay will provide good opportunities for further tests of QCD, and possible verification of the three-gluon gauge coupling through the study of four-jet events. The most persuasive tests of the three-gluon coupling are in fact likely to come from toponium studies, and if toponium is within the energy range of the SLC, it is even conceivable that some operation will be in that regime.

The impact of the use of various drift-chamber/calorimeter combinations on the global aspects of jet analysis was examined in the Parameters Section of Ref. 1.1 and is shown in Table 2.1. Referring to the table, model 2 is very close to our proposed upgraded detector, whereas model 1 is a device whose properties come about as close to those of an ideal detector as one can imagine. Model 3 differs from model 2 in that the detector has no endcaps.

The results in the table indicate that the percentage of the total energy that is seen and the reconstruction efficiency of three clusters from 3-jet events for that for model 2 are roughly equivalent to the nearly ideal model 1 and much better than that for model 3. For the other parameters considered the three detectors are all rather similar. We conclude that our proposed detector will perform multijet analyses nearly as well as a detector with essentially ideal geometry and energy resolution.

TABLE 2.1

The table summarizes the results of a study of jet axis direction resolution ($\delta\vartheta_j$) and jet energy resolution (δE_j) for three-cluster events. Also shown is the fraction of energy detected (E_{seen}) and the fraction of produced three-jet events which are reconstructed as three clusters (ε_{3jet}). The index j is 1 for the fastest jet, 2 for the intermediate jet and 3 for the slowest jet.

Model 1: Charged tracking over 95%; $\Delta p/p^2 = 0.25\%$ GeV^{-1}. Photon tagging over 98% , $\Delta E/E = 10\%/\sqrt{E}$, 2 cm (5 cm) strips (towers). Barrel detector is 4 m long at $R = 1.5$ m, rest endcaps.

Model 2: Charged tracking over 86%; $\Delta p/p^2 = 0.5\%$ GeV^{-1}.Photon tagging over 98%; $\Delta E/E = 15\%/\sqrt{E}$, 5 cm (15 cm) strips (towers). Barrel detector is 3 m long, at $R = 1.5$ m, rest endcaps.

Model 3: Same as model 2 except no endcap photon detection.

		$\delta\vartheta_1$	$\delta\vartheta_2$	$\delta\vartheta_3$	δE_1	δE_2	δE_3	E_{seen}	ε_{3jet}
		degrees	degrees	degrees	percent	percent	percent	percent	percent
Perfect Detector		1.2	1.6	3.4	1.6	4.7	12.0	90	78
Model 1	Strips	1.8	2.3	4.8	2.4	7.2	15.0	76	65
	Towers	2.0	2.5	4.8	2.5	7.2	15.0		
Model 2	Strips	1.9	2.4	4.2	2.8	7.2	17.3	72	63
	Towers	2.4	2.9	4.9	2.9	7.2	18.0		
Model 3	Strips	2.0	2.5	5.2	5.6	7.1	18.6	63	45
	Towers	2.5	3.0	5.6	5.8	7.0	18.7		

2.4 Searches for Exotic Objects

A. $Z^\circ \to s_l^+ + s_l^-$

We define here $s_l^\pm$ as the supersymmetric scalar analog of the corresponding lepton $l^\pm$. This process will occur with branching ratio about half of that for $Z^\circ \to + l^+ l^-$ if $s_l^\pm$ exists and has mass $< m_z/2$. The $s_l^\pm$ will decay into $l^\pm$ plus unseen photinos, and the signatures will be highly non-collinear pairs of charge conjugate leptons with substantial missing momentum and energy. The important features of the proposed detector in identifying this process are (a) good lepton identification and hadron rejection, (b) good energy and angular resolution, (c) large solid angle coverage by the calorimeter to help establish the existence of missing momentum and energy.

B. $Z^\circ \to p^+ + p^-$

The particles $p^\mp$ are hyperpions or charged Higgs, and are pseudoscalars with masses less than $m_z/2$. They are detected through their decays into fermion pairs, for example, $t\bar{b}$, $c\bar{s}$ or $\tau\nu_\tau$. The analysis depends on branching ratios into hadrons and leptons, but will be similar to that already published for the PEP energy range by the Mark II group.

C. $Z^\circ \to$ free quarks or $Z^\circ \to$ massive stable charged objects

The combination of time-of-flight and dE/dx measurements in the drift chamber should allow detection of massive stable objects with fractional or integral charge. For integral charge, such objects would be detected if their velocity were appreciably less than c.

2.5 Applications of Vertex Detection

The ability to tag the presence of weakly decaying particles in the 10^{-13} sec lifetime range will further strengthen the capability of the Mark II detector to pursue many areas of physics. For example, t quarks, Higgs particles, and hyperpions are all expected to produce charm and τ particles in their decay chains. Therefore, vertex tags should improve signal-to-background ratios in identifying these particles and provide valuable information on the decay modes. Another application will be decays of the Z° into c and b quarks, which will provide large samples of charmed and bottomed hadrons, for which precise lifetime measurements can be made.

2.6 Detection of Semileptonic Decays of Heavy Quarks

We have carried out a simulation of the detection of semileptonic decays of heavy quarks. For this study, we have used 1) charged tracking programs and simulated raw data to evaluate how well we reconstruct the charged tracks and 2) our standard liquid argon algorithms to measure the probability that a hadron is misidentified as an electron ($P_{h \to e}$).

We use a Monte Carlo simulation program for $Z^\circ \to$ hadrons, where Z° hadronic decay events are produced according to the standard quark branching fractions with $M_{Z^\circ} = 89$ GeV/c^2. The QCD matrix elements are those of the Ali et al. model [2.1] which has been widely used at PEP/PETRA. We have chosen to use the heavy quark fragmentation functions ($d\sigma/dZ$, $Z = E_{\text{hadron}}/E_{\text{beam}}$) shown in Fig. 2.1. These fragmentation functions have the form [2.2]

$$\frac{d\sigma}{dZ} \propto \frac{1}{Z} \cdot \frac{1}{\left[1 - \frac{1}{Z} - \frac{\varepsilon}{(1-Z)}\right]^2}$$

where $\varepsilon_{\text{charm}} = 0.3$, and $\varepsilon_{\text{bottom}} = 0.04$ come from the Mark II measurements at PEP. ε_{top} scaled according to the mass^{-2}, is taken to be 0.002. (It should be noted that these fragmentation functions lead to harder lepton spectra than those assumed for the SLAC SLC Workshop). Semi-leptonic branching fractions are typically ~10%. Unless otherwise stated, the top mass was assumed to be 25 GeV/c^2.

The detector was assumed to have the proposed drift chamber geometry and raw data hits were created with the appropriate errors. We have used the present, somewhat rudimentary, version of our tracking program to reconstruct the charged tracks. For the issue of hadron rejection all charged tracks and photons are "tracked" through the liquid argon modules using an EGS simulation. The exact geometry of the liquid argon detectors is known to the EGS

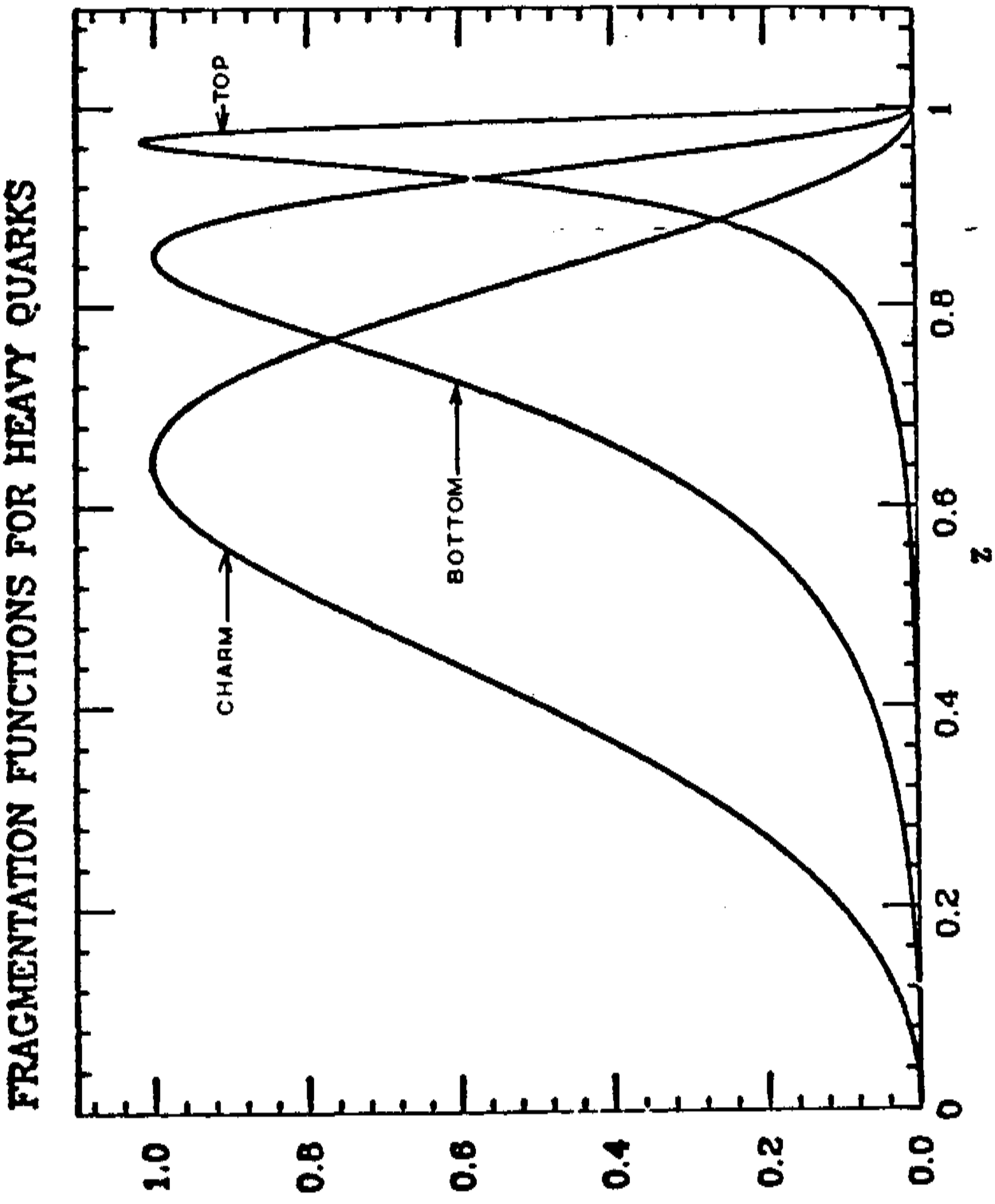

Figure 2.1 Fragmentation functions for heavy quarks

simulation so that raw (strip by strip) data are produced. We have considerable experience with this simulation procedure and know it to be a very accurate representation of the module response for electrons and photons. Having assigned the deposited energy in this way, we have run our PEP electron/hadron separation algorithm on all charged tracks. The $P_{h\to e}$ is obtained by counting the fraction of hadrons which are called electrons by this procedure. These numbers are discussed later [2.4].

The Mark II has carried out a successful analysis of b and c semi-leptonic decays at PEP [3,4]. In this analysis we obtained relatively pure samples of b and c quarks because of our good charged tracking and our good hadron rejection. We follow the same approach for this analysis. Hence, we consider events with at least one tagged electron, and then analyze these events in P/P_t space where P is the total lepton momentum and P_t is the lepton transverse momentum relative to the thrust axis ($q\bar{q}$ axis).

We have made a comparison between the response of a perfect charged particle detector and the charged particles reconstructed according to the procedure outlined above. From this study, we conclude that although the measurements are not all perfect reproductions of the Monte Carlo, they give a reasonably faithful representation of the information. The jet momenta, energies, and mass-squared numbers are for the most part rather good measurements of the actual quantities. The dE/dx information gives $e-\pi$ separation at the $\geq 3\sigma$ level for about 75% of the leptons.

We have further demonstrated that the reconstructed events preserve the produced information from a more refined analysis using all events which satisfy the following cuts:

1) Total visible energy in charged tracks within $|\cos\vartheta| < 0.85$ is greater than 35 GeV. This is intended to remove events concentrated along the beam line.

2) Thrust axis, as constructed from the tracked charged particles, has $|\cos\vartheta| < 0.75$.

We include all events ($q\bar{q}$, $q\bar{q}g$, and $q\bar{q}gg$) which satisfy these cuts and examine the lepton P/P_t plot for the <u>generated</u> events (Figs. 2.2a, 2.3a) as well as the <u>reconstructed</u> events (Figs. 2.2b and 2.3b). Fig. 2.2 (2.3) corresponds to leptons arising from bottom (top) quarks. The statistics in Figs. 2.2 and 2.3 are somewhat limited, but the trends are clear. Figs. 2.2b and 2.3b arising from the drift chamber reconstruction are faithful representations of the Monte Carlo inputs of Figs. 2.2a and 2.3a. The proposed drift chamber is fully adequate, even with the present preliminary tracking algorithms, for the task of analyzing these semi-leptonic decay events.

The heavy quark semileptonic decays can be reconstructed by use of the dE/dx measurement capabilities of the drift chamber. Fig. 2.4a-c shows the calculated ratios, $\Delta E/\sigma$, of electron-pion dE/dx difference in units of standard deviations for electrons from c, b and t decays, respectively. Approximately 75% of electrons have $\Delta E/\sigma$ larger than 3 and 50% have $\Delta E/\sigma$ larger than 4. If we assume that we will "miss" our design goal of $\sigma = 6.9\%$ by 25%, then ~65% of the electrons have $\Delta E/\sigma$ larger than 2. We now look in detail at the physics which one would obtain from such a measurement.

Table 2.2 defines the problem. The population by electrons of the P/P_t space is shown separately for the electrons in events in which the primary quark was c, b, or t. P_t is defined relative to the closest parton direction as produced in the Monte Carlo. This is not ideal because in a realistic analysis one would measure P_t relative to the reconstructed thrust axis. For the two-jet events

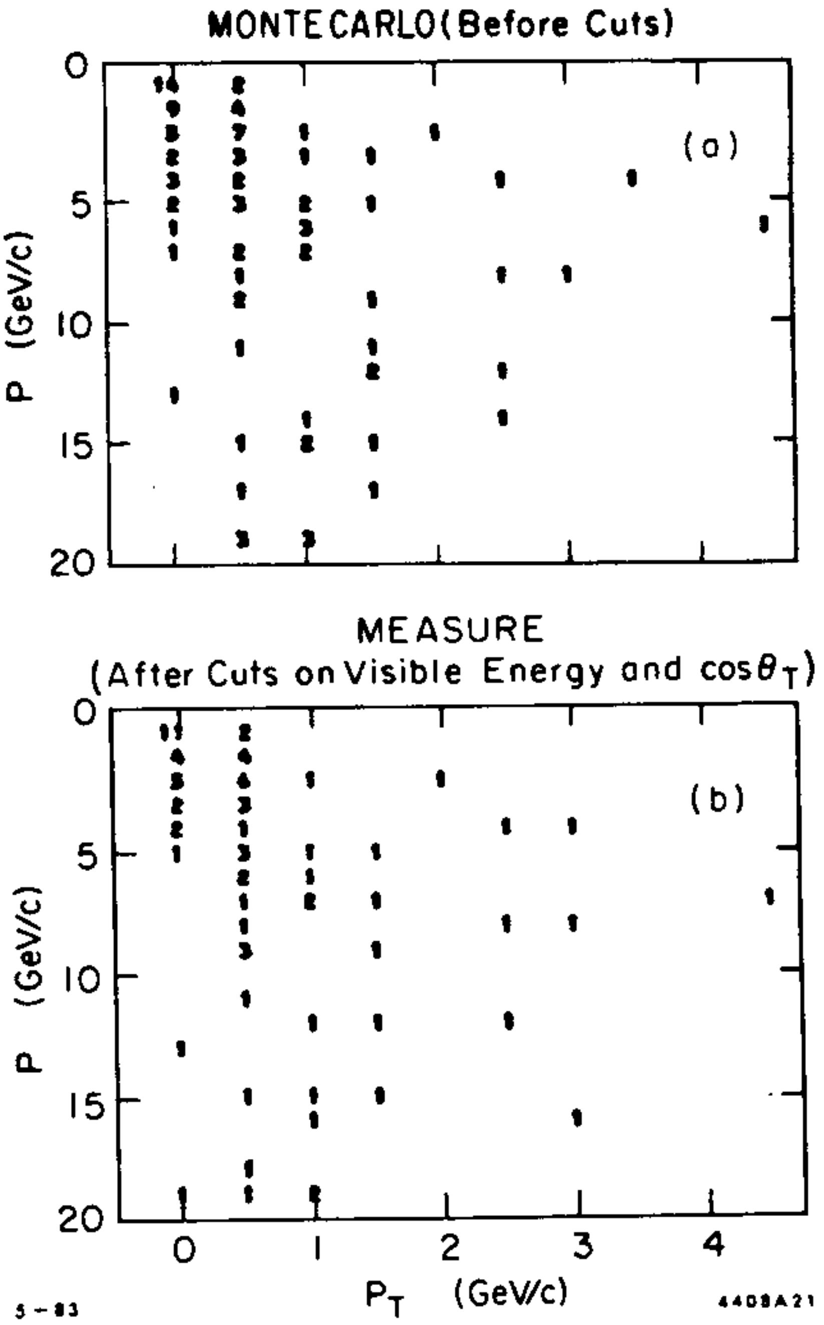

Figure 2.2 Comparison of Monte Carlo generated and reconstructed events for B-decays.

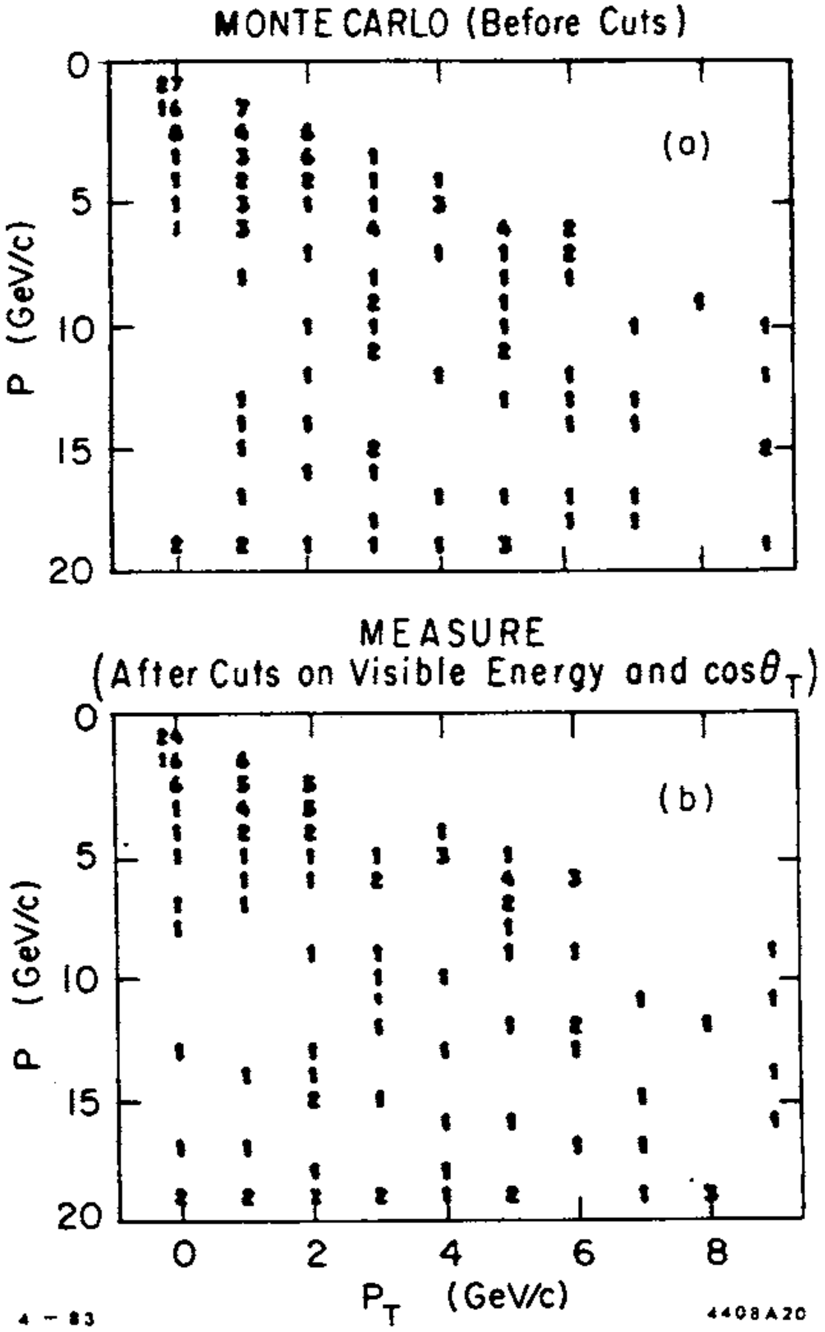

Figure 2.3 Comparison of Monte Carlo generated and reconstructed events for T-decay.

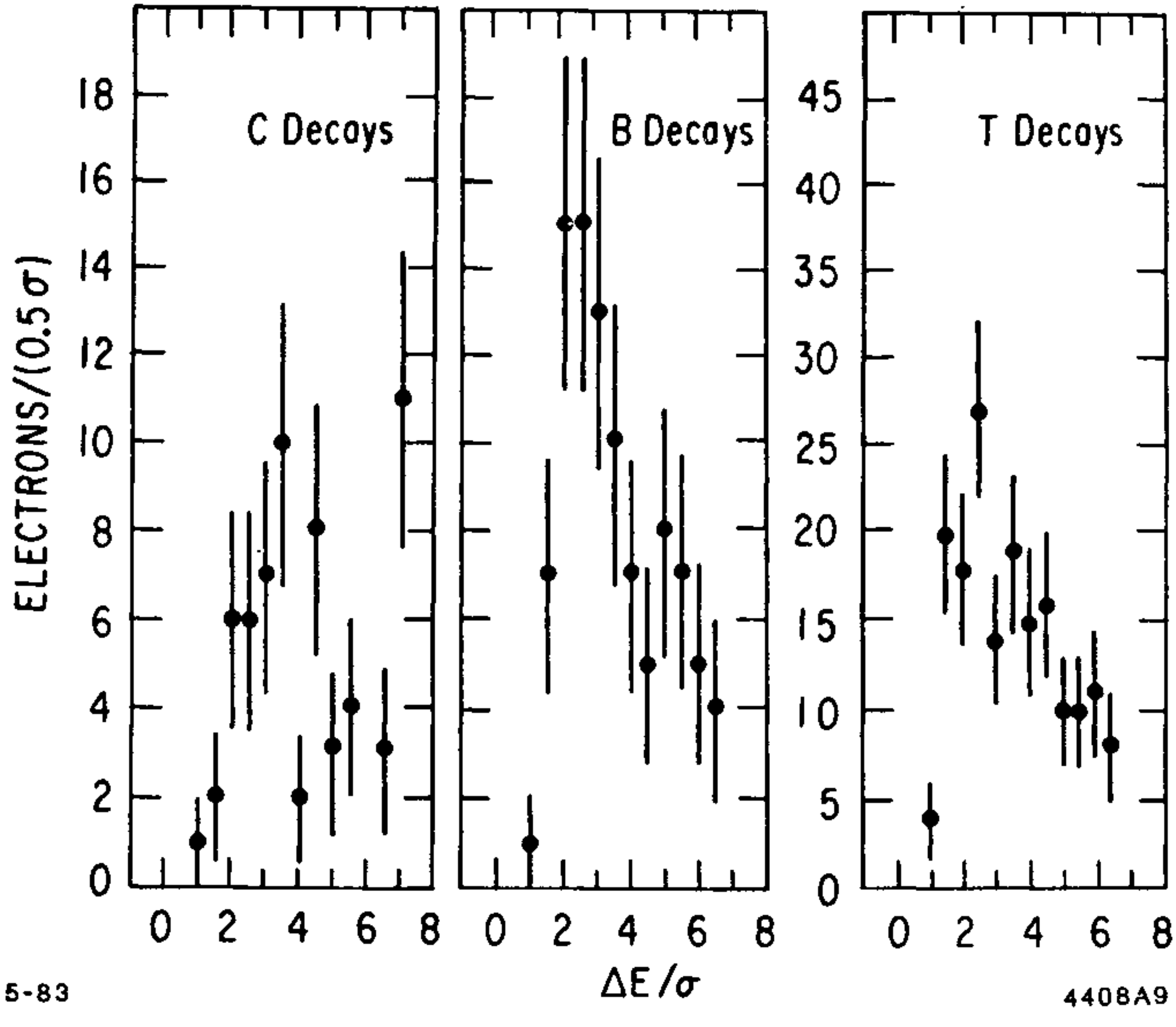

Figure 2.4 Electron/Pion separation from dE/dx measurements.

TABLE 2.2

Signal Populations for Electrons from Charm, Bottom and Top Quarks

P/P_T	0-0.5 (GeV/c)	0.5-1	1-1.5	1.5-2	2-2.5	2.5-3	3-3.5	3.5-4	4-4.5	>4.5
1-3 (GeV/c)	45	1								
	52	19	4							
	27	74	63	35	12	6				
3-5	29	8								
	21	25	6	2						
	7	6	22	16	14	13	11	6	5	7
5-7	19	9								
	11	13	5	2						
	1	6	2	3	8	9	10	8	3	18
7-9	14	13								
	5	6	10	4						
	2	2	1	1	4	2	3	3	4	16
9-11	9	12								
	6	6	4	4	1					
	0	1	1	2	1	1	3	2	0	15
11-13	9	7								
	3	5	4	3	1					
	1	0	1	2	1	2		4	3	14
13-15	6	5								
		2	5	1	2					
		0	0	1	0	0	2	0	2	10
15-17	4	5								
		5	2	1	1					
		1	0	0	0	0	0	1	2	14
>17	4	8								
		8	13	5	1					
		1	0	0	2	4	5	2	1	42

($M_t = 25$ GeV/c^2) KEY: Charm
Bottom
Top

TABLE 2.3

Hadron Populations and Hadron Misidentification Probabilities

P/P_T	0-0.5 (GeV/c)	0.5-1	1-1.5	1.5-2	2-2.5
1-3 (GeV/c)	24,001 0.059	14,162 0.005	2991 0.003	579 0.004	200 ≤0.01
3-5	6972 0.063	3782 0.015	963 0.01	450 0.010	
5-7	3359 0.102	2102 0.016	435 0.007	215 ≤0.01	
7-9	2064 0.089	1306 0.019	266 0.010		
9-11	1141 0.044	809 0.014	196 ≤0.01		
11-13	765 0.045	618 0.010	143 ≤0.01		
13-15	529 0.050	415 ≤0.01			
15-17	365 0.050	290 ≤0.01			
>17	896 ≤0.01	725 ≤0.01			

(Unless stated $P_{h\to e}$ <0.01) KEY: #Hadrons
$P_{h\to e}$

(>70% of the events) this procedure is perfectly reasonable because we find that in this case the reconstructed thrust axis reproduces the $q\bar{q}$ direction to within a few degrees. For events with hard gluon radiation, the procedure generates a slightly less accurate measure of P_t. However, this definition of P_t does not change the essential features of Table 2.2. The numbers in Table 2.2 correspond to 17,500 produced Z°'s, corresponding to approximately a two month run at an average luminosity of 10^{29}. Electrons arising from gamma conversions are not included in these plots. We have shown at PEP that we are capable of reconstructing $\gtrsim 80\%$ of the photon conversions and they are thus easily eliminated. Electrons arising from Dalitz decays are confined to small P and P_t where, as we will see later, backgrounds from hadron misidentifications dominate. In the region of good signal to misidentification background, the yield of electrons from Dalitz decay is negligibly small. We discuss the physics of Table 2.2 in the absence of background and return to the background question later. The most striking feature of Table 2.2 is that there are large regions of P/P_t in which the top quark has sole occupation. One would readily detect the presence of the top quark even with a few thousand Z°'s! In the absence of the t quark, there are regions where bottom is clearly separated from charm ($P_t > 1$ GeV/c for all P).

In the regions which are populated by both top and bottom, the two species are readily separable based on event shapes. Consider Figure 2.5 which shows the aplanarity (measure of the momentum out of the event plane), versus the jet mass for b and t quark events. Cuts as indicated in Fig. 2.5 show that a clean sample of b's can be obtained even in the presence of t's. This clean separation of b and t using a shape analysis warrants a little more discussion. Here we were concerned about the effects of detector resolutions, solid angle coverage and analysis techniques. To avoid too optimistic a result then, we took the Monte Carlo generated particle vectors and smeared them according to the resolutions

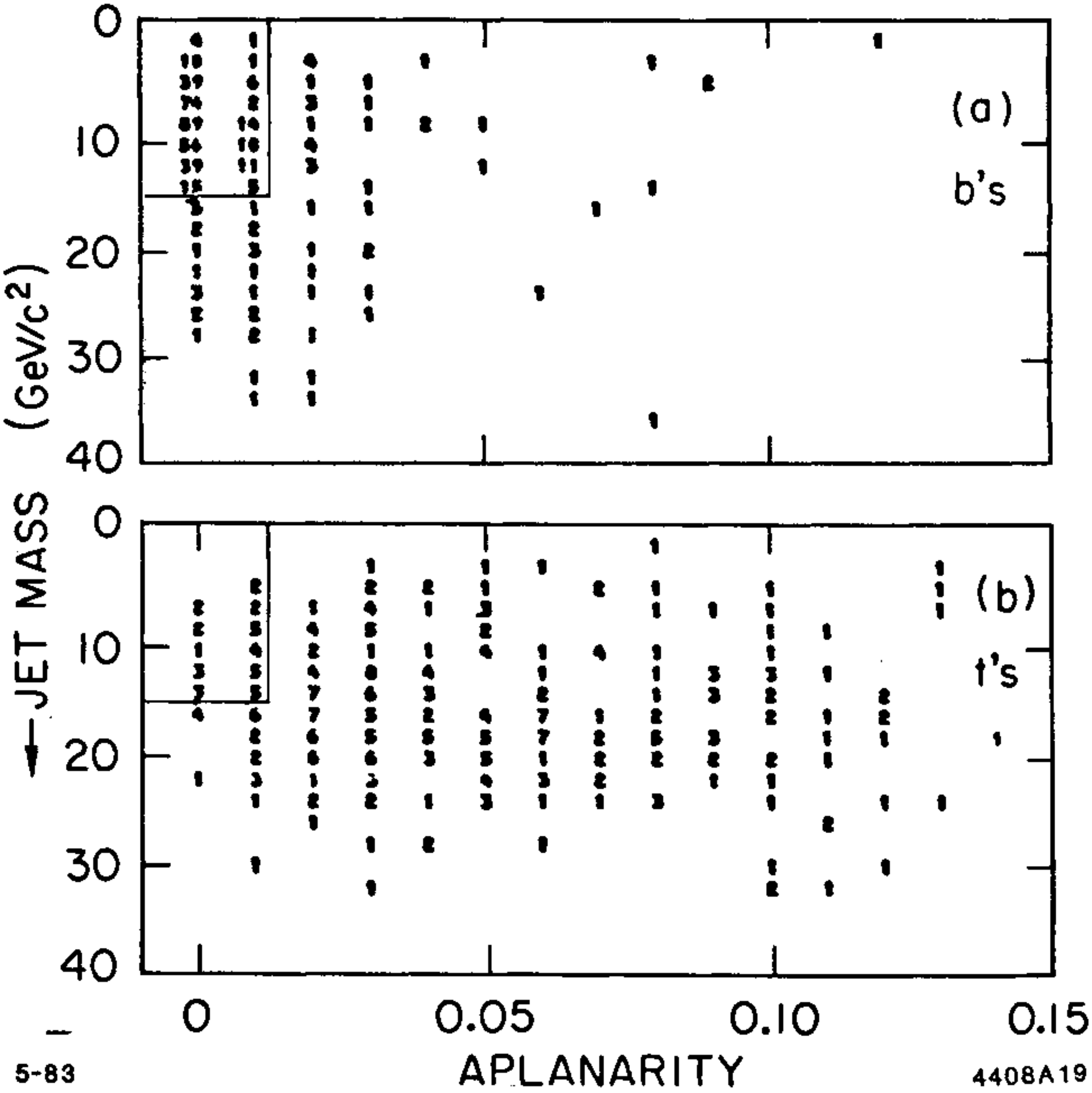

Figure 2.5 Separation of b-quark and t-quark events from shape analysis. The blocked off region has a >10:1 enhancement of b relative to t for a b efficiency of >80%.

given in this proposal. Only tracks in the instrumented solid angle were included. A cluster algorithm [2.3] was applied to the data which partitioned the event into two, three and some four cluster (jet) events. Each cluster's momentum and energy is defined by the set of particles which define the cluster. The jet mass is then calculable from the energy and momentum of the cluster. Entries were made into Fig. 2.5 only for the two-cluster events--events involving hard gluon bremsstrahlung have been removed (i.e., 3-cluster events). Hence, with high efficiency (>70%) b quark events are isolated with a small (<10%) t contamination.

We conclude then that if the background from misidentified hadrons can be handled, a clean sample of b's and t's will be obtainable from the semi-leptonic events.

We now discuss the level of background arising from misidentified hadrons. To study this we have taken the same $Z^\circ \to$ hadrons events used to produce Table 2.2. In Table 2.3 (upper entry) we show the yield of hadrons (from all six quarks) as a function of P and P_t. The yields are normalized to the same number of events as the lepton yields in Table 2.2. We have used the procedure outlined earlier to find the fraction of these hadrons which are misidentified as electrons. These numbers appear as the lower entries in Table 2.3. For comparison, we have included the measured misidentification fractions obtained at PEP in Table 2.4. For Table 2.3, we have filled in only those P/P_t boxes where the backgrounds appear to be larger than, comparable to or measurably less than the signal; for those P/P_t boxes without entries, the signal is essentially background free. Multiplying the two entries in Table 2.3 yields the background arising from misidentified hadrons. These numbers are summarized as the left-hand entries in Table 2.5. These background estimates should be compared directly with the entries in Table 2.2; for convenience we have transcribed the

TABLE 2.4

Hadron Misidentification Probabilities
as Measured at PEP

P / P_T	0-0.5 (GeV/c)	0.5-1	1-1.5	1.5-2
1-2 (GeV/c)	0.022 ± 0.008	0.010 ± 0.005	0.007 ± 0.003	0.007 ± 0.003
2-3	0.015 ± 0.008	0.008 ± 0.005	0.007 ± 0.003	0.007 ± 0.005
3-4	0.010 ± 0.005	0.006 ± 0.003	0.005 ± 0.002	0.005 ± 0.002
4-5	0.007 ± 0.003	0.005 ± 0.003	0.004 ± 0.002	0.004 ± 0.002
5-6	0.007 ± 0.003	0.005 ± 0.003	0.004 ± 0.002	0.004 ± 0.002
6-7	0.006 ± 0.003	0.004 ± 0.003	0.003 ± 0.002	0.004 ± 0.002

TABLE 2.5

Background and Signal Populations

Numbers in brackets give background
after use of dE/dx with $\sigma(dE/dx) = 86\%$

P/P_T	0-0.5 (GeV/c)		0.5-1		1-1.5		1.5-2		>2	
1-3 (GeV/c)		45		1						
	1416	52	71	19	9	4	2		0	
	(<14)	27	(<1)	74	(<1)	63		35		18
3-5		29		8						
	578	21	56	25	9	6	4	2	0	
	(12)	7	(1)	6	(<1)	22		16		56
5-7		19		9						
	340	11	34	13	3	5	2	<2	0	
	(23)	1	(2)	6	(<1)	2		3		56
7-9		14		13						
	184	5	25	6	3	10		4		
	(22)	2	(3)	2	(<1)	1		1		36
9-11		9		12						
	50	6	11	6	3	4		4		1
	(9)	0	(2)	1	(<1)	1		2		22
11-13		9		7						
	34	3	6	5	<2	4		3		1
		1		0		1		2		24
13-15		0		5						
	26		<4	2	<1	6		1		2
				0		0		1		14
15-17		4		5						
	18		<3	5		2		1		1
				1		0		0		17
>17		4		8						
	<9		<7	8		13		5		1
				1		0		0		56

Backgrounds are insignificant if no entry

KEY:		
		c
	Bkgd	b
	(+dE/dx)	t

entries from Table 2.2 onto Table 2.5 (we have not included the hadron rejection capabilities of the dE/dx system). Comparison of the background and the summed signal in Table 2.5 show that there are large regions of P/P_t where the top quark electrons are perfectly clean. In addition, the regions where the bottom signal appears separated from both top and charm are also background free. For $P_t < 1.0$ GeV/c, the misidentification backgrounds dominate or are comparable to the signal. However, below 10 GeV/c in momentum, the dE/dx rejection power becomes significant and should be included (see Table 2.5). Hence, where the liquid argon by itself begins to limit the separation of the signal and background, the dE/dx takes over. Therefore, with good electron efficiency, we estimate that an additional factor of $\gtrsim 10$ reduction in the backgrounds in Table 2.5 will result from the dE/dx measurement of the semi-leptonic decay electrons for all P/P_t ranges. This means the background will be comparable to the total signal in the lowest P_t bin, and considerably less, elsewhere.

We summarize the tagging of top and bottom quark events using semi-leptonic electron decays as follows: the Mark II drift chamber will have the tracking efficiency, momentum and angular resolutions, and solid angle adequate to give a faithful and efficient reconstruction of the semi-leptonic events; using realistic simulations (cross-checked by PEP measurements) of the hadron rejection in the liquid argon, we find that a large fraction of the top semi-leptonic events are cleanly separated from both background and the lighter quarks. A few thousand Z° decays would suffice to establish the presence of a >20 GeV/c^2 top quark. A clean bottom signal is also obtainable using only the liquid argon as a hadron rejector; there is some overlap between the top and bottom quarks but this is easily removed using shape analysis on the events The fractional yield of bottom events is low when the liquid argon only is used to reject background. Use of the dE/dx system, however, allows us to cleanly identify prompt electrons in virtually the entire P/P_t space. At worst, the backgrounds are comparable to the signal and this occurs only for the region $P_t < 0.5$ GeV/c and $P \leq 7$ GeV/c. As an indication of the tagged yields, we have chosen to count bottom and top tagged events for all P/P_t except $P_t < 0.5$ GeV/c and $P < 5$ GeV/c. For an average luminosity of 10^{29} (30 times smaller than design) and a 6 month run, the Mark II would have ~2000 tagged top decays and ~500 tagged bottom decays.

Now, we briefly indicate some of the physics that will be possible given that one has clear t and b tags. The top quark events can be used to establish the top quark fragmentation function through a fit to the P/P_t spectrum. From the fit one would also obtain the top quark mass since the distribution of P_t is a direct measure of mass. The fragmentation function should be well measured with ~2000 events--the b fragmentation function at PEP was similarly obtained with <100 bottom decays. The sensitivity to the top quark mass comes from the endpoint measurement of the P_t spectrum. Fig. 2.6 shows a comparison of dn/dP_t for top quarks with masses 25 GeV/c^2 and 30 GeV/c^2. One notices that the spectra differ at the largest P_t's. The exact value of the endpoint of the P_t spectrum is, as one would expect, sensitive to the top quark mass. This sensitivity should lead to a determination of the top quark mass to a few GeV/c^2. Having established the top quark mass to a few GeV/c^2, and assuming that $t\bar{t}$ had not yet been seen, one could possibly take the SLC down in energy and search for the $t\bar{t}$ threshold given the small scan region defined by the measured t quark mass. (The proposed fall-off of the SLC luminosity as one lowers the beam energy is very small; $L(\text{peak}) \sim 4 \times 10^{30}$ at $E_{cm} = 60$ GeV.) The bottom fragmentation function can likewise be measured from the bottom tagged events.

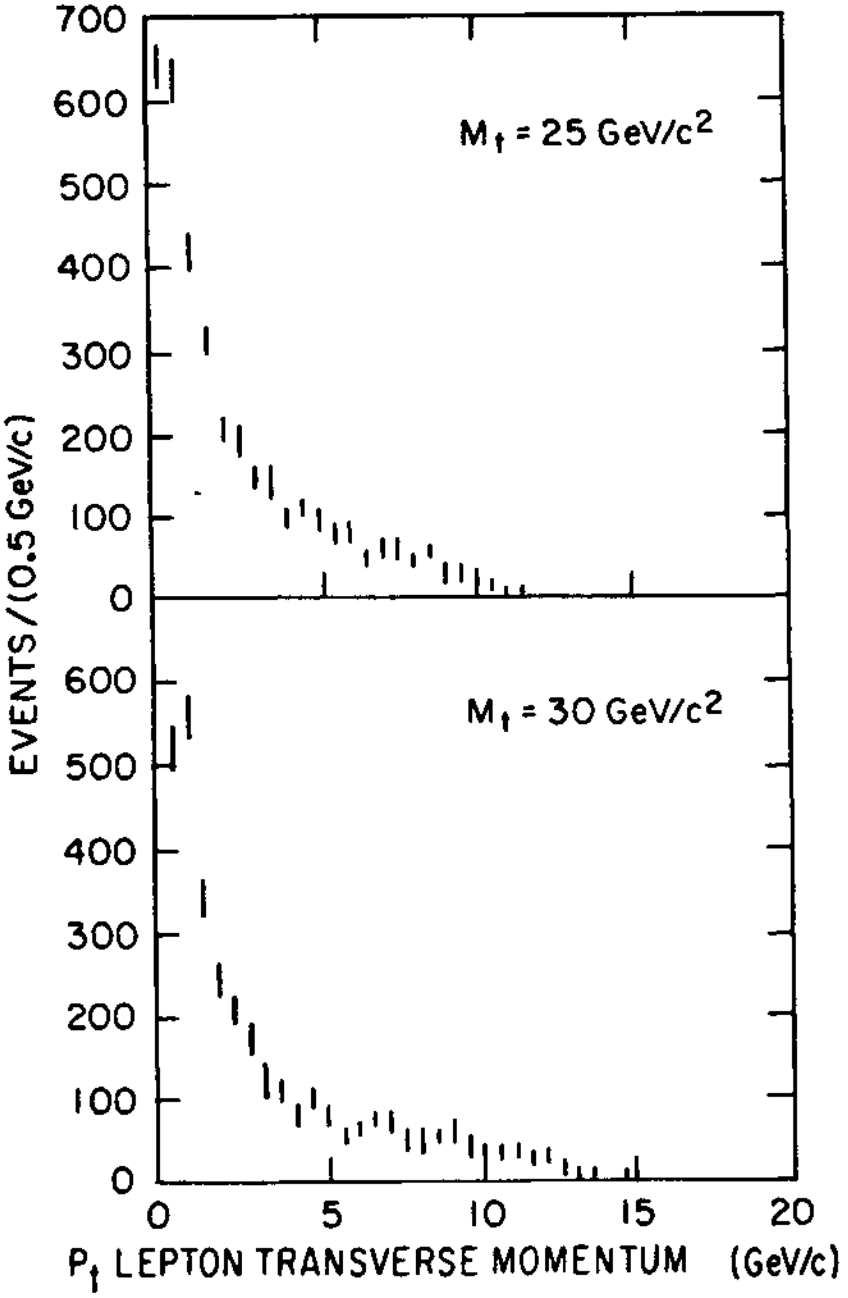

4-83 4408A10

Figure 2.6 Transverse momentum distribution from t-quark decay. End point determines mass of t-quark.

2.7 Search for the Neutral Higgs Boson

The search for the neutral Higgs Boson at the SLC will be done, as outlined [2.5] by Bjorken in the 1976 SLAC Summer Institute, by looking for the decays

$$Z^{\circ} \rightarrow H^{\circ}\, e^{+}e^{-} \tag{1}$$

and $Z^{\circ} \rightarrow H^{\circ}\, \mu^{+}\mu^{-}$ (2)

These decays are described by the bremsstrahlung diagram shown in Fig. 2.7. The propagator of the virtual $Z^{\circ *}$ is such that the momentum distribution of the Higgs is peaked sharply at low values and the leptons are produced mostly back-to-back and with large energies. Our method of analysis for (1) and (2) is to search for events with two high momentum particles that are within the fiducial region of the detector. Several cuts are made, as described below, to remove backgrounds that arise from semi-leptonic decays of top quarks and from the inelastic radiative Bhabha and annihilation diagrams shown in Fig. 2.8. We first discuss the properties of the detected signal events.

We have written a fairly detailed Monte Carlo simulation of the decays (1) and (2). The matrix element was taken from Refs. 2.6 and 2.7, and the generated distributions have been checked against published results. We note that the distribution of lepton pair masses given in the SLC Workshop Proceedings appears to differ from that predicted by our calculation. Our result agrees with other published results [2.6]. The beam energy spread (0.5%) has been included in the calculation, and initial-state radiation has also been done by assuming that the SLC is operated with the nominal center of mass energy equal to the Z° mass. In reality it will operate somewhat above the Z° mass in order to optimize the Z° production rate. The effects of these beam properties on the recoil mass resolution are not completely negligible. The detector response has been simulated by using the tight-vertex-constrained resolution for the drift chamber, and

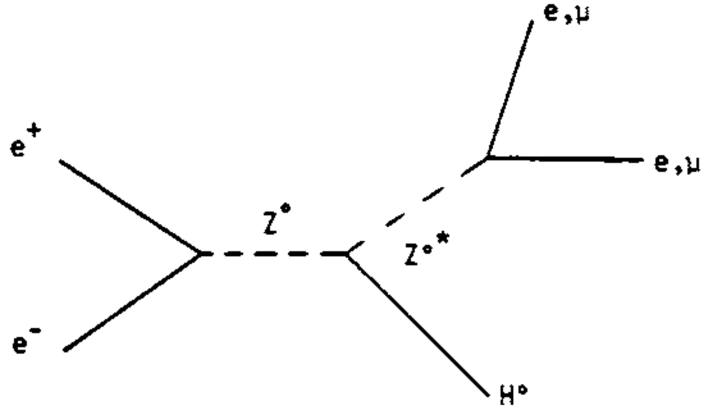

FIGURE 2.7

the calorimeter resolutions have been conservatively taken to be $15\%/\sqrt{E}$ for the liquid argon (the electron energies are typically $\gtrsim$ 25 GeV) and $18\%/\sqrt{E}$ for the endcap. As we normally do in our analyses of PEP data, we have removed from the fiducial region of the calorimeters ±2° in azimuth at the cracks between the liquid argon modules. The region $0.68 \leq |\cos\vartheta| \leq 0.72$ has also been removed since we expect the calorimeters to be too thin in that region to provide good energy resolution for high energy electrons. The angular resolutions of the detector have also been included. For purposes of this exercise we have assumed that the material around the beam pipe totals 3% of a radiation length and the electrons have been allowed to radiate in this material. The momentum measured by the drift chamber is affected by this loss of energy, but a photon radiated by a high energy electron strikes the calorimeter at essentially the same spot as the electron itself (typically within 1 cm), and so the radiated energy will properly be assigned to the electron.

The yields of the detected events predicted by this simulation are shown in Figs. 2.9 and 2.10 for Higgs masses of 10 GeV/c^2, 25 GeV/c^2, and 35 GeV/c^2. The backgrounds shown in these figures are discussed below. The momentum resolution for electrons that are within the fiducial region of the electromagnetic calorimeters has been optimized by using, as the best estimate, a weighted average of the momentum measured by the drift chamber and the energy measured by the calorimeters. Good calorimetry in the endcap region is important here since the distribution of the final state electrons is approximately given by $1 + \cos^2\vartheta$ and the resolution of any solenoidal spectrometer becomes degraded as $\cos\vartheta$ increases beyond ≈ 0.7. The muon momenta are, of course, measured only by the drift chamber. As can be seen in the figures, the distributions are slightly asymmetric. This is due to initial state radiation and also reflects the fact that $d\sigma/dm$ is plotted rather than $d\sigma/dm^2$. The resolution in the e^+e^-,

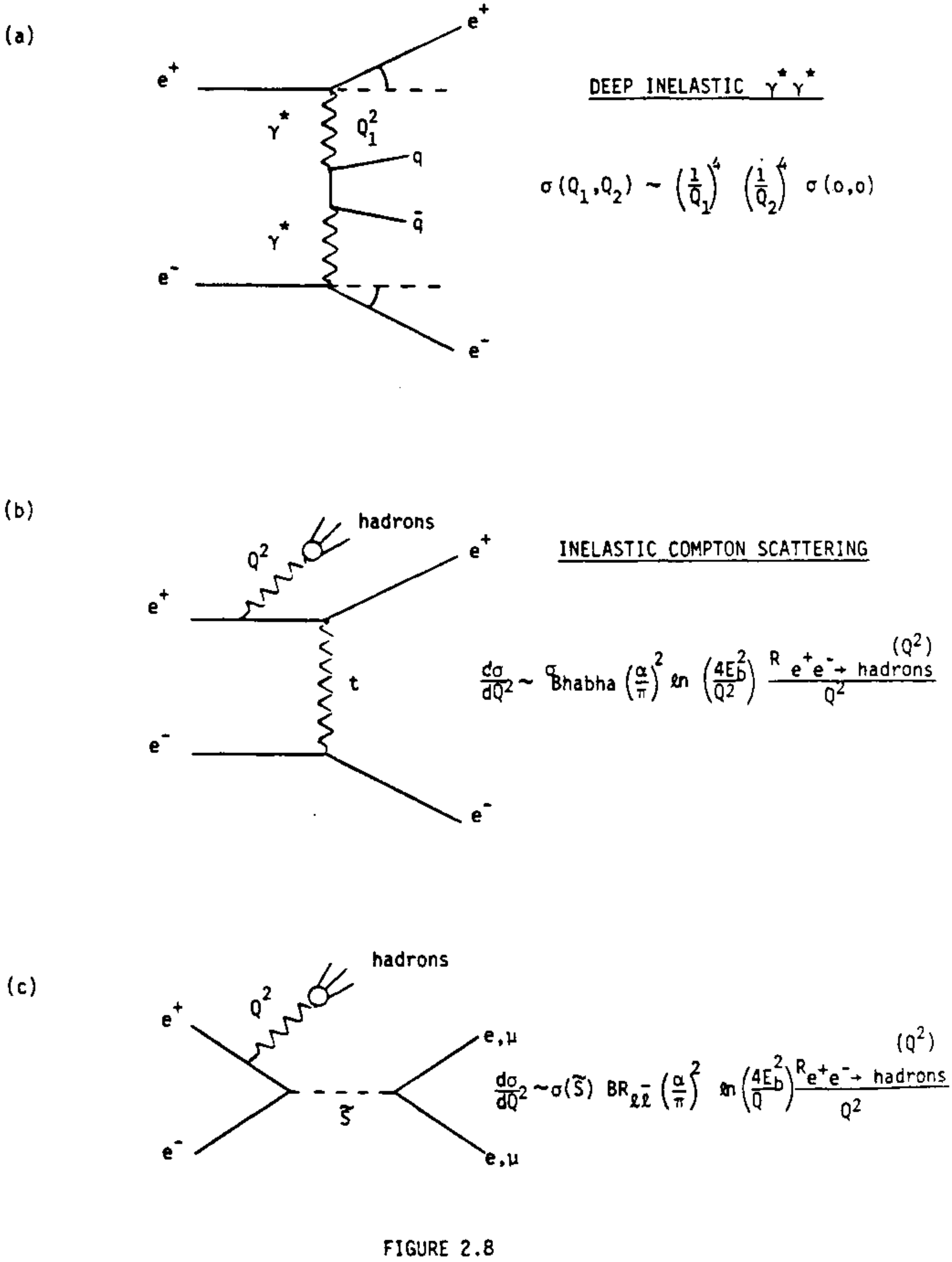

DEEP INELASTIC $\gamma^*\gamma^*$

$$\sigma(Q_1,Q_2) \sim \left(\frac{1}{Q_1}\right)^4 \left(\frac{1}{Q_2}\right)^4 \sigma(0,0)$$

INELASTIC COMPTON SCATTERING

$$\frac{d\sigma}{dQ^2} \sim \sigma_{Bhabha} \left(\frac{\alpha}{\pi}\right)^2 \ln\left(\frac{4E_b^2}{Q^2}\right) \frac{R_{e^+e^-\to\text{ hadrons}}(Q^2)}{Q^2}$$

$$\frac{d\sigma}{dQ^2} \sim \sigma(\tilde{S})\ BR_{\ell\bar{\ell}} \left(\frac{\alpha}{\pi}\right)^2 \ln\left(\frac{4E_b^2}{Q}\right) \frac{R_{e^+e^-\to\text{ hadrons}}(Q^2)}{Q^2}$$

FIGURE 2.8

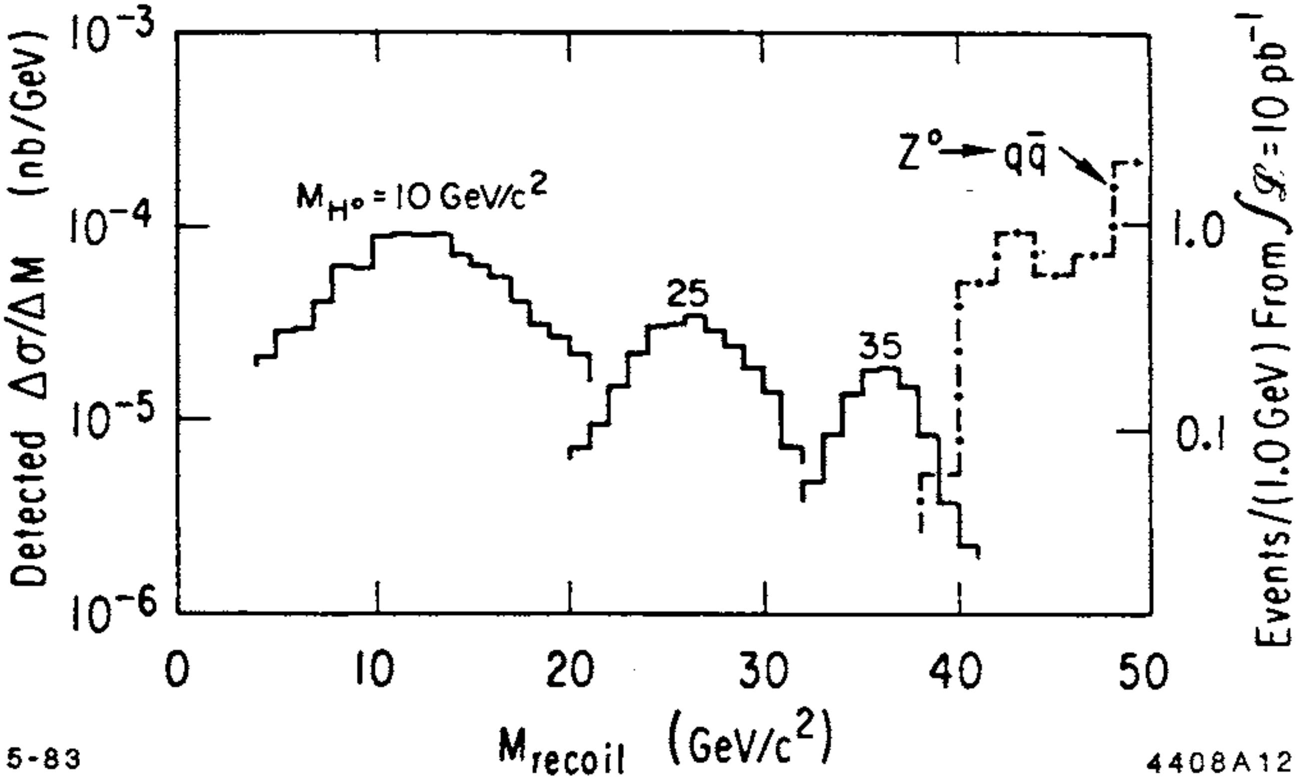

Figure 2.9 The Higgs signal from $Z^\circ \rightarrow H^\circ e^+e^-$. The expected backgrounds are also shown.

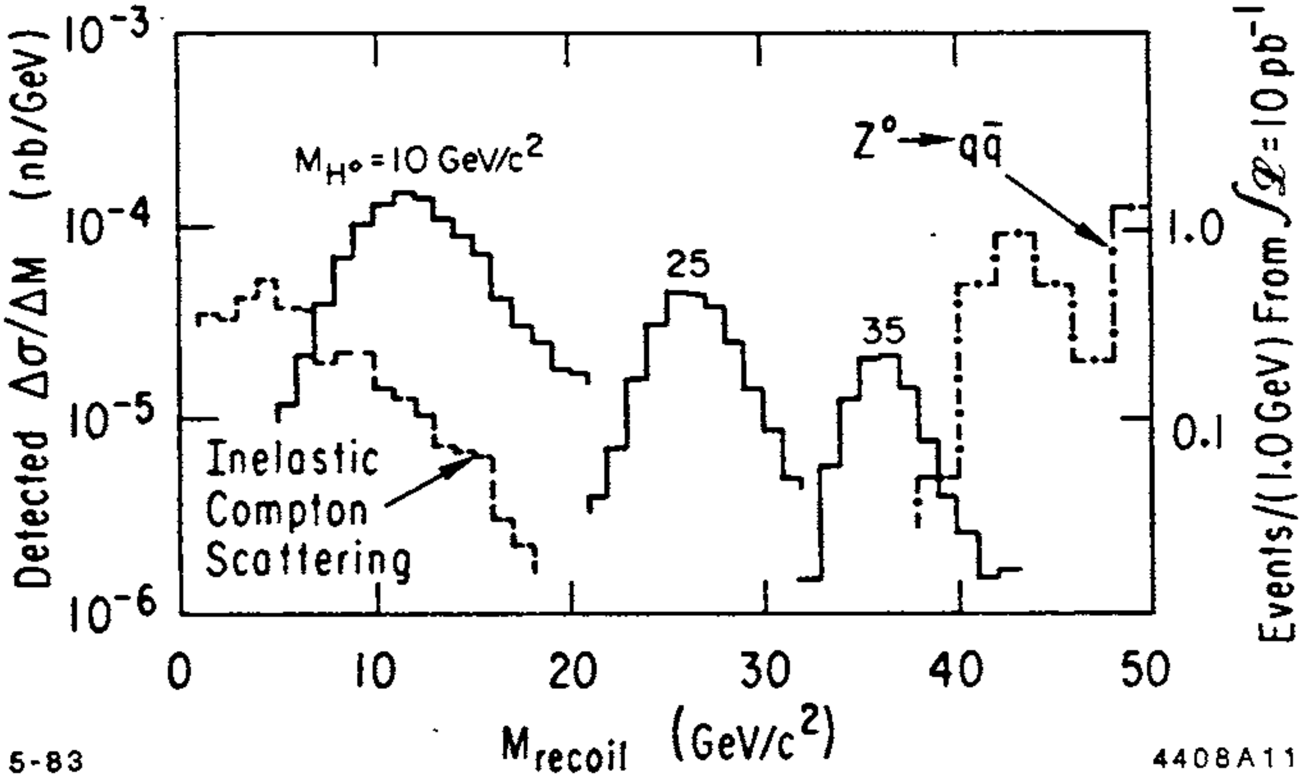

Figure 2.10 The Higgs signal from $Z^\circ \rightarrow H^\circ \mu^+\mu^-$. The expected backgrounds are also shown.

recoil mass is found to be $\sigma = 2.7$ GeV/c^2 at a Higgs mass of 10 GeV/c^2, and $\sigma = 1.5$ GeV/c^2 at 35 GeV/c^2. The corresponding values for the $\mu^+\mu^-$ channel and for electrons that do not have useful information from the calorimeters are 4.6 GeV/c^2 and 2.0 GeV/c^2, respectively. The overall geometrical acceptance of the detector is ≈ 70% and is independent of the Higgs mass. This value includes what we believe are realistic fiducial and background cuts. Before discussing the feasibility of seeing these signals we must examine the known backgrounds to reactions (1) and (2).

As previously mentioned, the backgrounds to decays (1) and (2) that we have identified consist of semi-leptonic decays of heavy quarks and of the radiative processes shown in Fig. 2.8. We have made an estimate of the contamination due to decays of various quark types using the Monte Carlo generated events described in Section 2.6 above. With appropriate cuts we find that only $t\bar{t}$ events produce a significant background in the recoil mass region of interest. The background in the e^+e^- signal (1) has been estimated by selecting events that produce two electrons each with momentum greater than 7.5 GeV/c. The invariant mass of the e^+e^- pair is then required to be greater than 10 GeV/c^2. These two cuts have been included in our calculation of the yields of Higgs events shown in Figs. 2.9 and 2.10; they remove only a few per cent of the signal events. We also make a cut, as described in the SLC Workshop Proceedings, on the angle between the detected electrons and the thrust axis reconstructed from the remaining particles. We make this cut at 15°. We have not included the effect of this cut on the signal events, but since the Higgs is produced mostly at rest, there will be little correlation between the direction of the leptons and the decay products of the Higgs. This cut will remove <10% of the signal events. The analysis of the $\mu^+\mu^-$ events proceeds in exactly the same manner, only in this case we do not require that the muons be identified, only that candidate particles be clearly not electrons. This means that the background from $q\bar{q}$ decays will be somewhat higher since a few pions will be energetic enough to produce recoil masses in the region of interest. Our estimates of the $q\bar{q}$ backgrounds are shown in Figs 2.9 and 2.10 as dashed-dotted histograms. As can be seen, these events populate the recoil mass region above 40 GeV/c^2, but are such that detection of a 35 GeV/c^2 Higgs by this method appears difficult. More severe cuts will be required to reduce the background. With extremely large data samples a cleaner signal would be visible from the $Z^\circ \to H^\circ + \gamma$ decay. The energy of the 40 GeV photon that recoil against a 35 GeV/c^2 Higgs will be measured in our detector with a resolution $\sigma = 1.0$ GeV, and an integrated luminosity of 100 pb^{-1} would result in 3 to 4 detected events in a narrow energy range.

Shown in Fig 2.8 are processes that produce lepton pairs with low recoil masses in coincidence with hadrons. The peripheral two-photon process (Fig. 2.8a) is heavily suppressed since the internal photons have masses Q^2 that are typically in the range 300-400 GeV^2 (i.e., $Q^2 \sim E_b^2\,\vartheta^2$). We have computed the rate for this process using the computer program written [2.7] by J. Smith and J. Vermaseren and find that it is quite small. We differ on this point with the analysis given in the SLC Workshop Proceedings. The estimate given there is based on the assumption that the two-photon cross section is independent of Q^2. The inelastic Compton process shown in Fig. 2.8b is more of interest. This process, however, can also be computed with the Smith-Vermaseren program, and we have used this program to compute the dashed curve shown on Fig 2.9 for the background due to both diagrams 2.8a and 2.8b. We assumed a constant value of $R_{ee\to hadrons} = 4$ and have folded in our detector resolution. No cuts were made on the hadronic system. As a check on these estimates we have searched for events of this type in our PEP data. Events were selected if two high energy electrons were detected in the fiducial region of the liquid argon accompanied by three or more additional charged particles. No cut was made on the invariant mass of the hadronic system. We have found three such events in a data sample that corresponds to an integrated luminosity of 35 pb^{-1}. Although we would use the endcap region in our search for the Higgs at the SLC, the relevant values of momentum transfer produced at PEP are still lower than those at the SLC and, hence, the detected wide-angle-Bhabha rate is larger at PEP than it will be at the SLC.

The diagram shown in Fig. 2.8c has not, to our knowledge, been treated in the literature as a background to the Higgs search. We have not done an exact evaluation of this process, but an order of magnitude estimate can be made by replacing the Bhabha cross section in diagram 2.8b with the annihilation cross section $\sigma(\hat{s})\, BR(Z^\circ \rightarrow l\bar{l})$. Notice that for internal bremsstrahlung of a photon, the contamination of the $\mu^+\mu^-$ final state is probably not much less than that of the e^+e^- final state. The detected wide-angle-Bhabha cross section is $\approx$ 0.4 nb and if we evaluate $\sigma(\hat{s})$ at its peak, then $(m_{Z^\circ})\, BR(Z^\circ \rightarrow l\bar{l}) \approx 0.9$ nb. If no cuts are made on the hadronic system, then the rate is dominated by events at low Q^2, and finite resolution on the recoil mass will then smear these events exactly as shown in Fig. 2.9 for the inelastic Compton process. Note also that there will be a contribution from Z° exchange in the t channel that, at 90°, will be approximately half as large as the Bhabha rate. As can be seen in the figure, if the background curve is multiplied by a factor of three or four, then it would become a problem in searches for a low mass Higgs in either the e^+e^- or $\mu^+\mu^-$ channel. We believe, however, that all of the backgrounds shown in Fig. 2.8 can be substantially reduced by making reasonable cuts on the hadronic system accompanying the lepton pair. The simplest cut will be to require that the hadronic system consist of at least two charged particles with an invariant mass greater than 1-2 GeV/c^2. Even if the Higgs decays 50% of the time to $\tau^+\tau^-$, this cut would reduce the acceptance of the analysis for signal events by less than ≈10%, but would eliminate most of the background.

Summarized in Table 2.6 are the properties of the signals and backgrounds for luminosities that yield 10 events in the combined e^+e^- and $\mu^+\mu^-$ channels in a mass region that is consistent with the resolution of the detector. The size of this region for each of the three considered Higgs masses is shown in the table The luminosity required to produce a signal has been estimated from the calculations given in Figs. 2.9 and 2.10. These numbers include corrections for losses due to all analysis cuts, and in particular, the loss of 10 GeV Higgs events due to cuts on the hadronic system was assumed to be 10% as discussed above. The uncertainty in the mass determination has been estimated from the e^+e^- channel as the resolution of the parent distribution (see Fig. 2.9) divided by the square root of the number of expected events. From our consideration of the backgrounds and event rates we feel that detection of the Higgs will be achieved if its mass is in the range 10-30 GeV/c^2. Declining production rates and increasing backgrounds at masses above 30 GeV/c^2 will make detection of the Higgs more difficult and success will depend upon the exact level of the background and machine luminosity.

TABLE 2.6

Summary of $Z^\circ \to H^\circ l\bar{l}$ Analysis

Higgs Mass	$\int L$	Signal Region	Expected Yields e^+e^-	 $\mu^+\mu^-$	Mass Uncertainty in e^+e^-	Backgrounds
10 GeV/c^2	7 pb^{-1}	±5 GeV/c^2	5.8	4.2	1.1 GeV/c^2	little, with appropriate cut on hadronic mass
25 GeV/c^2	20 pb^{-1}	±4 GeV/c^2	5.5	4.5	0.90 GeV/c^2	none expected
35 GeV/c^2	46 pb^{-1}	±3 GeV/c^2	5.2	4.8	0.65 GeV/c^2	possibly comparable with the signal

2.8 Determination of the Number of Light Neutrinos

The idea of neutrino counting in e^+e^- annihilations has been discussed previously by a number of authors [2.8-2.11]. The Feynman diagrams for $e^+e^- \to \gamma\nu\bar{\nu}$ are shown in Fig. 2.11 and the cross section is given by [2.9]:

$$\frac{d\sigma}{dxdy} = \frac{G^2\alpha}{6\pi^2}\left\{\frac{M^2\{N(g_v^2 + g_A^2) + 2(q_v + g_A)[1 - S(1-x)/M^2]}{[S(1-x) - M^2]^2 + M^2\Gamma^2} + 2\right\} \tag{3}$$

$$\cdot \frac{S}{x(1-y^2)}[(1-x)(1-\tfrac{1}{2}x)^2 + \tfrac{1}{4}x^2(1-x)y^2]$$

where, within the context of the standard model:

G = Fermi constant

α = fine structure constant

M = Z° mass

Γ = Z° width

N = number of neutrino species

$g_v = -\tfrac{1}{2} + 2\sin^2\vartheta_w$ (ϑ_w = weak mixing angle)

$g_A = -\tfrac{1}{2}$

x = E_γ / E (E_γ = photon energy, E = beam energy)

y = $\cos\vartheta_\gamma$ (ϑ_γ = angle between photon and beam)

s = $4E^2$, where E is the beam energy.

The general shape for the photon energy spectrum given by Eq. (3) is shown in Fig. 2.12 where the peak is a reflection of the Z° resonance.

Equation (3) can be simplified since in the kinematical region of interest:

$$(1 - \tfrac{1}{2}x)^2 \gg \frac{x^2y^2}{4}$$

and $$\frac{M^4\{N(g_v^2 + g_A^2) + 2(g_v + g_A)[1 - S(1-x)/M^2]}{[S(1-x) - M^2]^2 + M^2\Gamma^2} \gg 2$$

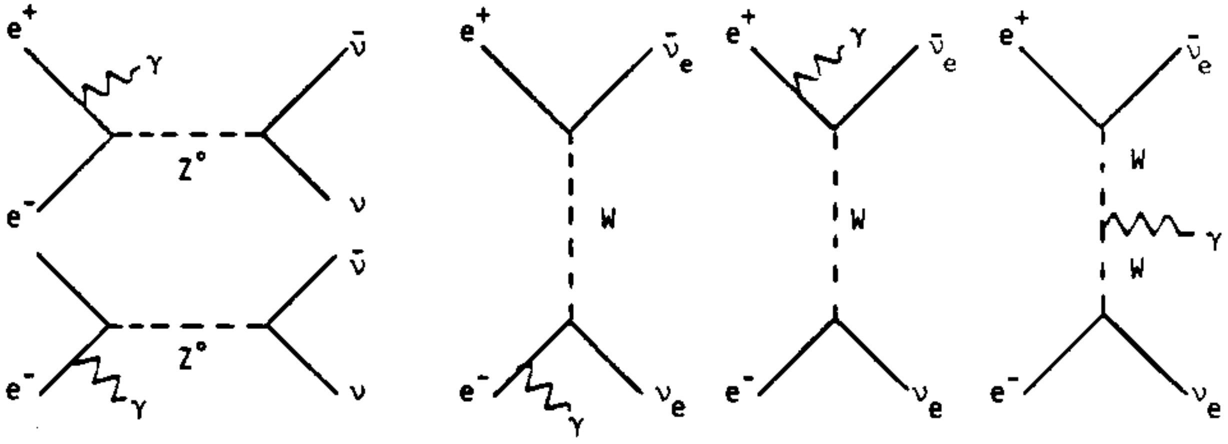

Figure 2.11 Lowest-order Feynman diagrams for $e^+e^- \to \gamma\nu\bar{\nu}$

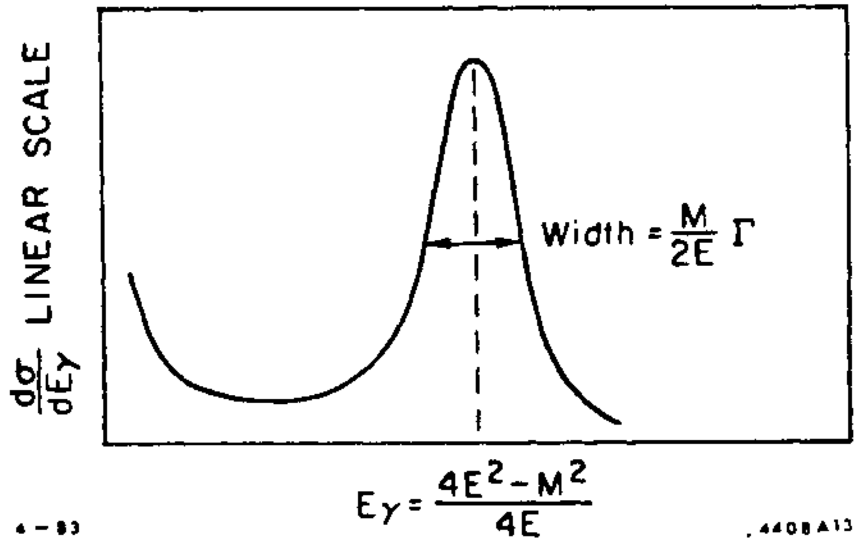

Figure 2.12 Photon energy spectrum in $e^+e^- \to \gamma\nu\bar{\nu}$ where E = beam energy, M = Z° mass, and Γ = Z° width.

We obtain:

$$\frac{d\sigma}{dx\,dy} \approx \frac{G^2 \alpha S}{6\pi^2} \frac{1}{1-y^2} \frac{(1-x)(1-\frac{x}{2})^2}{x} \left[\frac{0.25N - 1.08(1-S(1-x)/M^2)}{[1-S(1-x)/M^2]^2 + \Gamma^2/M^2} \right] \qquad (4)$$

Integrating $-y_{\max} < y < y_{\max}$

$$\frac{d\sigma}{dx} \approx \frac{G^2 \alpha S}{6\pi^2} \ln \frac{1+y_{\max}}{1-y_{\max}} \frac{(1-x)(1-\frac{x}{2})^2}{x} \left[\frac{0.25N - 1.08(1-S(1-x)/M^2)}{[1-S(1-x)/M^2]^2 + \Gamma^2/M^2} \right] \qquad (5)$$

On resonance $1-S(1-x_R)/M^2 = 0$, and for $y_{\max} = 0.94$ ($20° < \vartheta_\gamma < 160°$)

$$\left.\frac{d\sigma}{dx}\right|_{\max} \approx 13.9 \times 10^{-10} \frac{M^4 N}{\Gamma^2} \frac{(1 + M^2/S)^2}{(1 - M^2/S)} \qquad (6)$$

with $d\sigma/dx$ in nanobarns and all energies in GeV. We obtain the total cross sections in the peak by integrating in the range $\pm\Gamma$ around the $Z°$ peak:

$$\sigma(e^+e^- \to \gamma\nu\bar{\nu}) = \int_{x_R-\Delta x}^{x_R+\Delta x} \frac{d\sigma}{dx} dx \approx \left.\frac{d\sigma}{dx}\right|_{\max} \frac{2M\Gamma}{S} \tan^{-1} 2 \qquad (7)$$

where $\Delta x = \frac{2M\Gamma}{S}$ and $x_R = 1 - \frac{M^2}{S}$.

We have calculated cross sections for several values of N at two beam energies, assuming $M = 93$ GeV and $\Gamma = 2.8$ GeV $+ 0.18$ (N-3):

$\sigma(e^+e^- \to \gamma\nu\bar{\nu})$

N	$2E$ = 103 GeV	$2E$ = 108 GeV
3	0.0390 nb	0.0230 nb
4	0.0490	0.0288
5	0.0576	0.0340
6	0.0654	0.0386
7	0.0724	0.0427

If the experiment is carried out at 103 GeV then a 4σ statistical separation between $N = 3$ and $N = 4$ requires approximately 250 events for the $N = 3$ case. This in turn requires an integrated luminosity $\int \mathcal{L} dt \approx 6400\ \mathrm{nb}^{-1}$.

At 103 GeV the photon spectrum peaks at 9.5 GeV and for $N = 3$ has a width of 2.5 GeV. At 108 GeV these numbers are 14.0 and 2.4 GeV, respectively.

A. Backgrounds

Physical processes that produce energetic photons in low-multiplicity events include beam-beam and beam-gas bremsstrahlung, two-gamma interactions, and annihilations into two or three photons. In these processes, additional detectable particles accompany the photon and the experimental problem is to extend coverage of the apparatus so as to register these particles. In background events, the transverse momentum $p_\perp$ of the detected photon determines a minimum angle at which one of the other particles must appear (Fig. 2.13). This angle $\vartheta_{\min}$ is approximately equal to $p_\perp / 2E$ where E is, as defined above, the beam energy. If we wish to detect radiated photons down to 20° then, for $2E$ = 103 GeV, $\vartheta_{\min} \sim 24$ mr = 1.4°. If $2E$ = 108 GeV, $\vartheta_{\min}$ = 37 mr = 2.1°. The authors of reference 2.11 point out that the backgrounds are acceptable (<10% of signal) if detector coverage stops at somewhat larger angles ($\sim 2\vartheta_{\min}$). It should

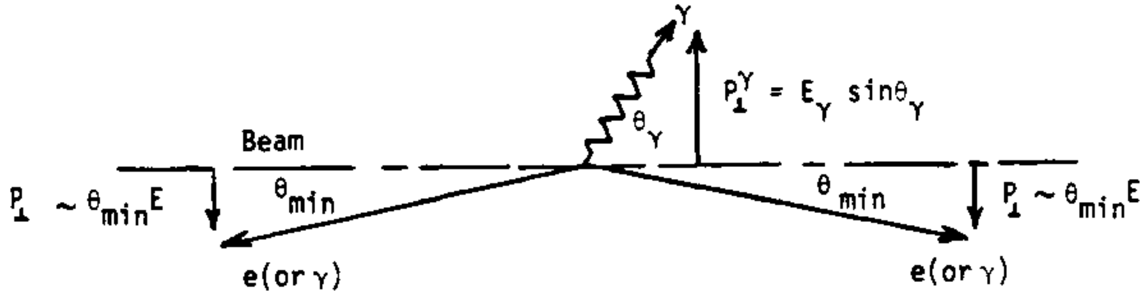

Figure 2.13 Kinematical picture of two potential background processes, $e^+e^- \to e^+e^-\gamma$ and $e^+e^- \to \gamma\gamma\gamma$. The detector must cover angles down to $\vartheta_{min} \sim p_\perp^\gamma / 2E$ to reject these events.

be noted that the luminosity monitor for this experiment is a Bhabha detector which covers angles down to $\lesssim$30 mr. Such a luminosity monitor will therefore reject the small-angle electrons and photons from the backgrounds enumerated above.

Potentially the most serious background problems for this experiment are associated with machine radiation (i.e., backscattered synchrotron photons, neutrons) at small angles. These backgrounds are difficult to estimate without a definite design for the final-focusing and masking systems. Proceedings from the SLC workshop indicate that one might obtain several hundred background photons per beam crossing in the angular region 20-200 mr. However, these studies did not include the case of interest here: a detector with $\vartheta > 30$ mr and quadrupole magnets beginning at ±50 cm from the crossing point. Large background radiation rates at small angles would present two possible major problems: high occupancy rates in the tracking system and radiation damage of the shower counters. The first of these dictates a tracking system at small angles with many layers and small dimensions per tracking element. The use of PWC's for the small-angle calorimetry addresses the second of these potential problems.

B. Estimate of Errors

The cross section measurement for $e^+e^- \to \gamma\nu\bar{\nu}$ depends directly on the number of photons observed and inversely on the total width of the Z° and the number of luminosity monitor counts. We expect a 6% statistical error in the photon count. Knowledge of the Z° width and the integrated luminosity will be limited by systematic errors each of which is estimated to be around 5%. The total error will then be at the 10% level allowing a 2.5σ separation between three and four families of neutrinos.

3. Detector Components

3.1 Solenoidal Magnet

There are three areas in which the Mark II solenoid is being upgraded:

1) A new coil is in fabrication to replace the present coil which developed a short in March 1982. The location of the coil and the number of ampere-turns is unchanged so that the field distribution will remain the same. New features are that it consumes less power (1.8 MW compared to 2.5 MW) and all water connections are on the ends of the coil and accessible. It is expected that winding will be complete in May 1983.

2) Presently the drift chamber, TOF system and coil are captured within the assembled iron. When the magnet is disassembled in 1984 to affect the detector exchange, a new cut-out in the end steel will be made so that it would be a much simpler operation to withdraw the chamber or coil in the event of a future need. The new incisions will not alter the distribution of the iron and will thus not affect the field.

3) The present system of using the overhead crane to remove and restore both end doors to gain access to the drift chamber takes about five hours of rigging time. In fact, the present method will no longer be possible when the new end cap detectors are installed because they are captured by the beam line vacuum chamber. Thus we are designing a new motor driven door extraction system which will be appended to each end of the magnet structure in 1984 and which will reduce the access operation from five hours to less than an hour.

3.2 Drift Chamber

The existing Mark II drift chamber has provided excellent tracking capability at both SPEAR and PEP. However, its precision for high energy tracks is limited by the relatively small number of layers and its pattern recognition capability is limited by inability to record more than one hit per cell. Therefore, we propose to replace the existing Mark II drift chamber with a new one with highly improved capability well matched to the requirements of Z^0 physics. The main elements which have been considered in the development of our new design are the following: (1) good momentum resolution with our 5kG magnet, (2) good solid angle coverage, (3) ease of pattern recognition and high tracking efficiency and (4) dE/dx measurement capability at a level to provide a useful, independent aid to calorimetry in electron-hadron separation up to a momentum of about 10 GeV/c.

A considerable design effort has been made, and we consider the chamber described here to be our final design. In this section of the Proposal, we give a summary of the chamber design and predicted performance and leave technical details to a more extensive discussion given in Appendix I.

The design of the new drift chamber is based on a multi-sense-wire cell shown in Fig. 3.1. This cell contains six sense wires staggered ± 380 μm on either side of the cell midplane to provide local left-right ambiguity resolution. There are two guard wires on either end of the cell for field shaping, and potential wires are placed between sense wires to reduce electrostatic deflections and to reduce signal coupling between adjacent sense wires. Potential wires, guard wires and sense wires are all tensioned to have the same gravitational sag. The fields on the surfaces of all field wires

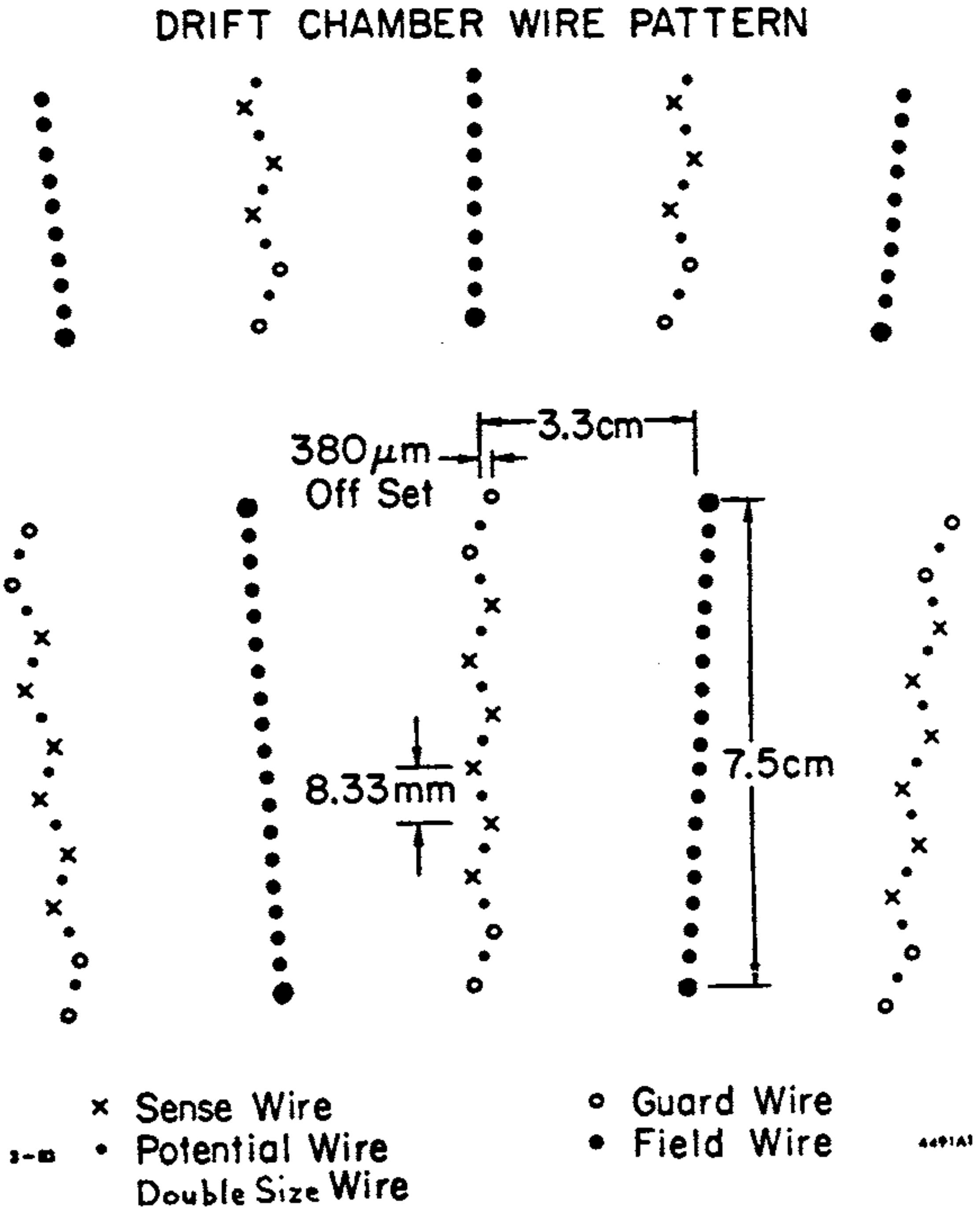

Figure 3.1 Cell structure of the proposed drift chamber.

are kept below 17.5 kV/cm to prevent whisker growth. The distance between field and sense wires in the middle of a six-sense-wire cell is 3.3 cm.

The drift chamber consists of twelve concentric layers of cells. Alternate layers have their wires parallel to the axis or at ~ ± 3.5° to the axis to provide stereo information. There are a total of 5832 sense wires and 72 samples for dE/dx measurement. The active length is 2.3 m. The overall layout is shown in Fig. 3.2, and the detailed parameters are given in Table 3.1.

The gas used will be a mixture of 89% Argon, 10% CO_2 and 1% Methane at atmospheric pressure. The experience at HRS and Mark III indicates that such a mixture may be less prone to whisker growth than the Argon-Ethane mixture used in the present Mark II drift chamber.

Table 3.1

Drift Chamber Parameters

Layer	Radius at Center (cm)	Stereo Angle (degrees)		Number of Cells	Accumulated Material including 2 mm Be inner cylinder and gas	
		Wire 1	Wire 6		(mg/cm^2)	Fraction of rad. length $\times 10^{-3}$
1	27.05	0	0	26	399	7.4
2	38.25	3.65	4.07	36	428	9.2
3	48.45	0	0	46	456	10.8
4	59.25	-3.73	-4.00	56	484	12.6
5	69.45	0	0	66	512	14.2
6	80.15	3.76	3.96	76	541	15.9
7	90.35	0	0	86	568	17.6
8	100.95	-3.77	-3.93	96	597	19.3
9	111.15	0	0	106	625	21.0
10	121.65	3.77	3.91	116	653	22.7
11	131.85	0	0	126	681	24.4
12	142.35	-3.78	-3.89	136	709	26.1

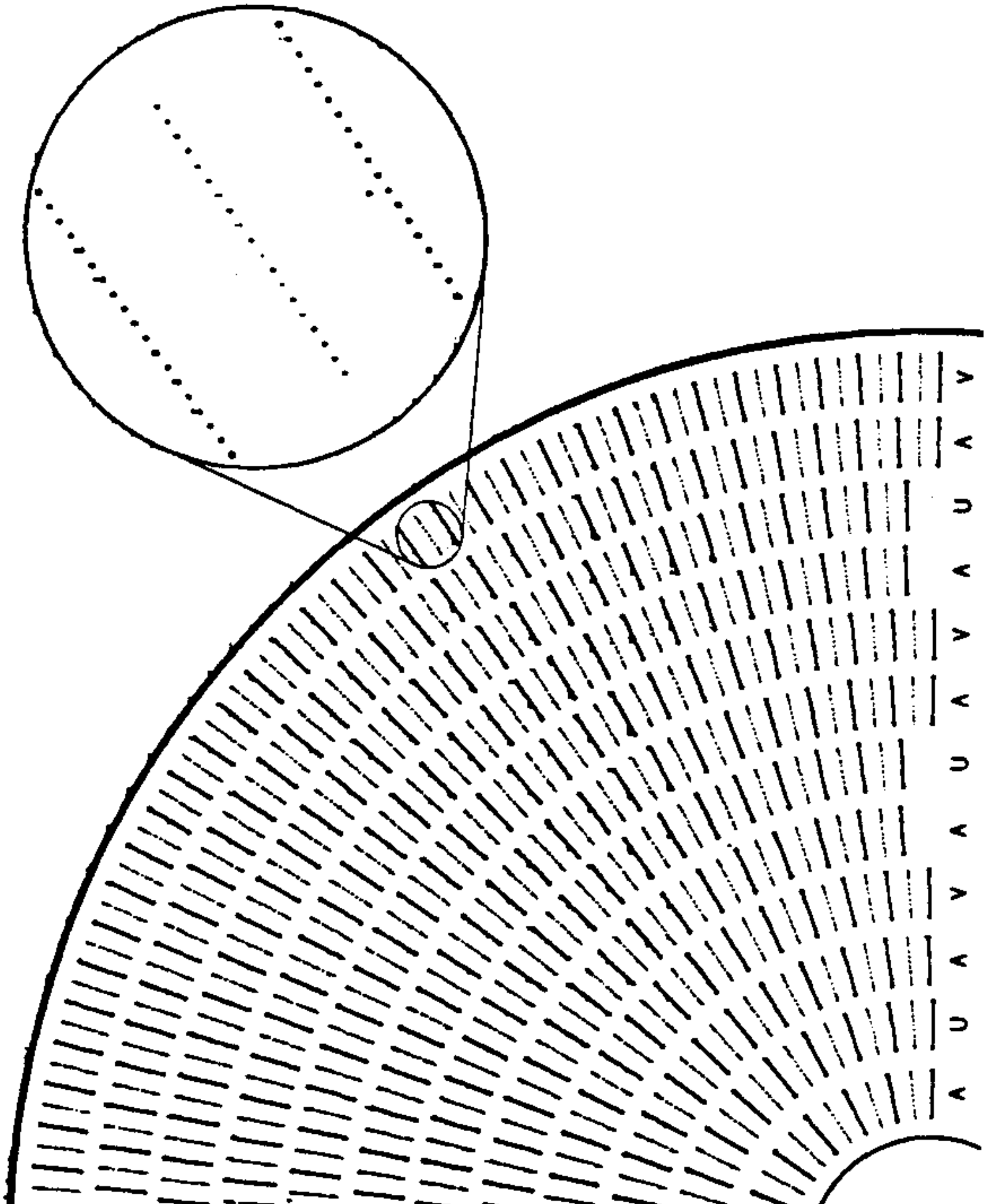

Figure 3.2 Overall layout of the drift chamber.

The expected electric field uniformity will result in a linear time-distance relationship which will aid the pattern recognition, and will provide good accuracy in the determination of both the track location and the dE/dx. The electronics is being designed to record multiple hits on each sense wire, and we expect a double track resolution of 4.2 mm or half the sense wire spacing.

It is worth emphasizing that our cell provides several advantages for pattern recognition. By staggering sense wires in the cell we can solve the left-right ambiguity prior to track finding and the nearly linear space-time relation allows very good spatial precision at the pattern recognition stage to facilitate track finding. Furthermore the comparison of the times from the several wires in a cell allows the use of the very good resolution of the chamber for the rejection of spurious hits (multi-pulsing, single bremsstrahlung hits, poorly measured points due to δ-rays, confused points due to crossing tracks in the cell) before pattern recognition begins. This could be particularly useful in an environment containing many soft photons or neutrons which might give a fair number of single hits but very few compatible hits over a number of adjacent wires. Finally, the randomization of the wire pattern from layer to layer improves our ability to separate nearby tracks and guarantees that a track cannot everywhere be near sense or field wires where the measurement accuracy tends to be worst.

The expected performance of the proposed drift chamber is summarized in Figs. 3.3 and 3.4. Momentum and angular precisions as functions of the cosine of the polar angle shown are based on an expected position accuracy of 200 μm. Multiple scattering is not included, and is expected to contribute an additional σ_p/p of 1.4% to the momentum error. The impact parameter error for track extrapolation to the beam line is 150 μm for

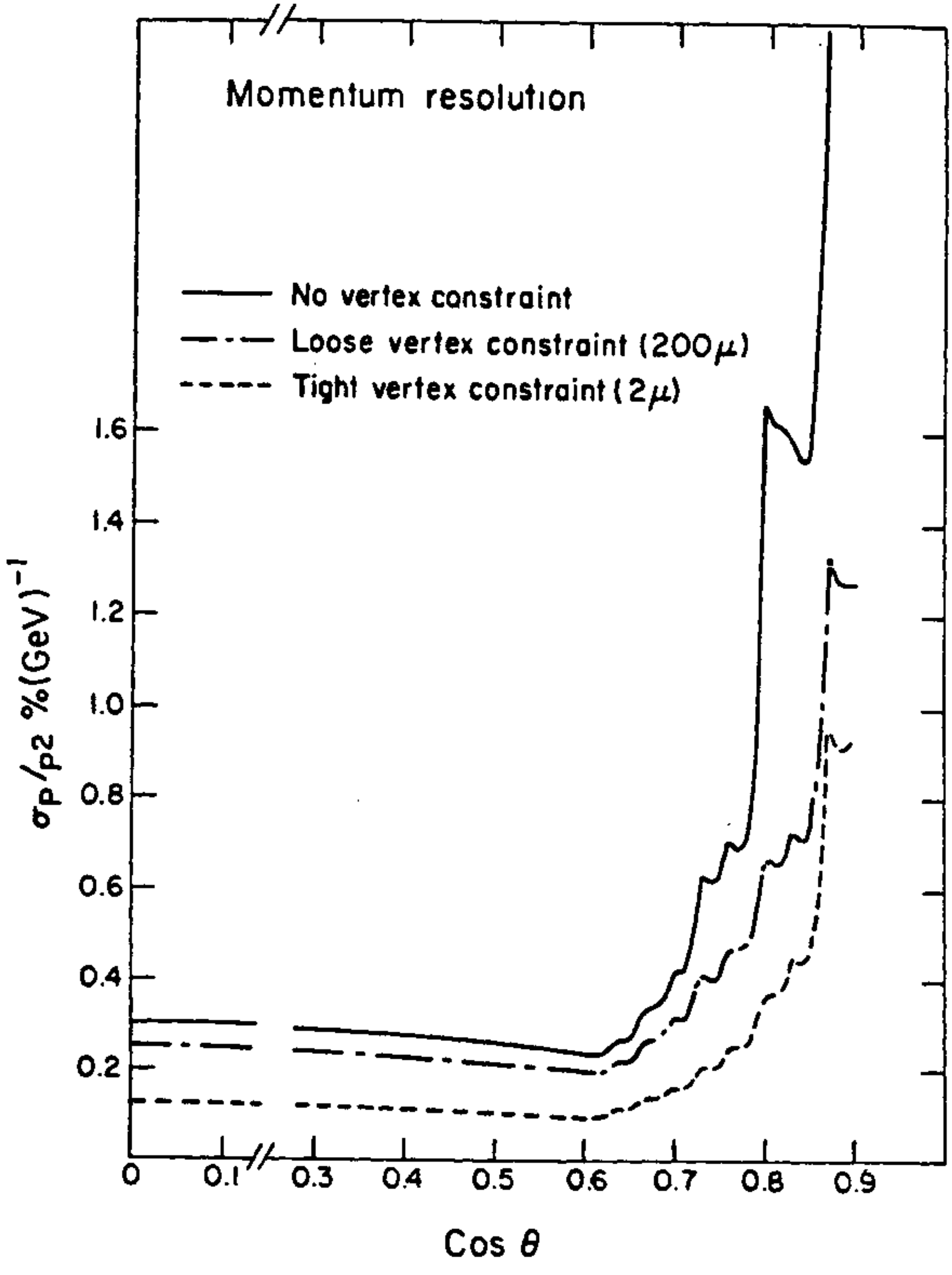

XBL 833-117

Figure 3.3a σ_p / p^2 in % GeV^{-1} as a function of cosϑ

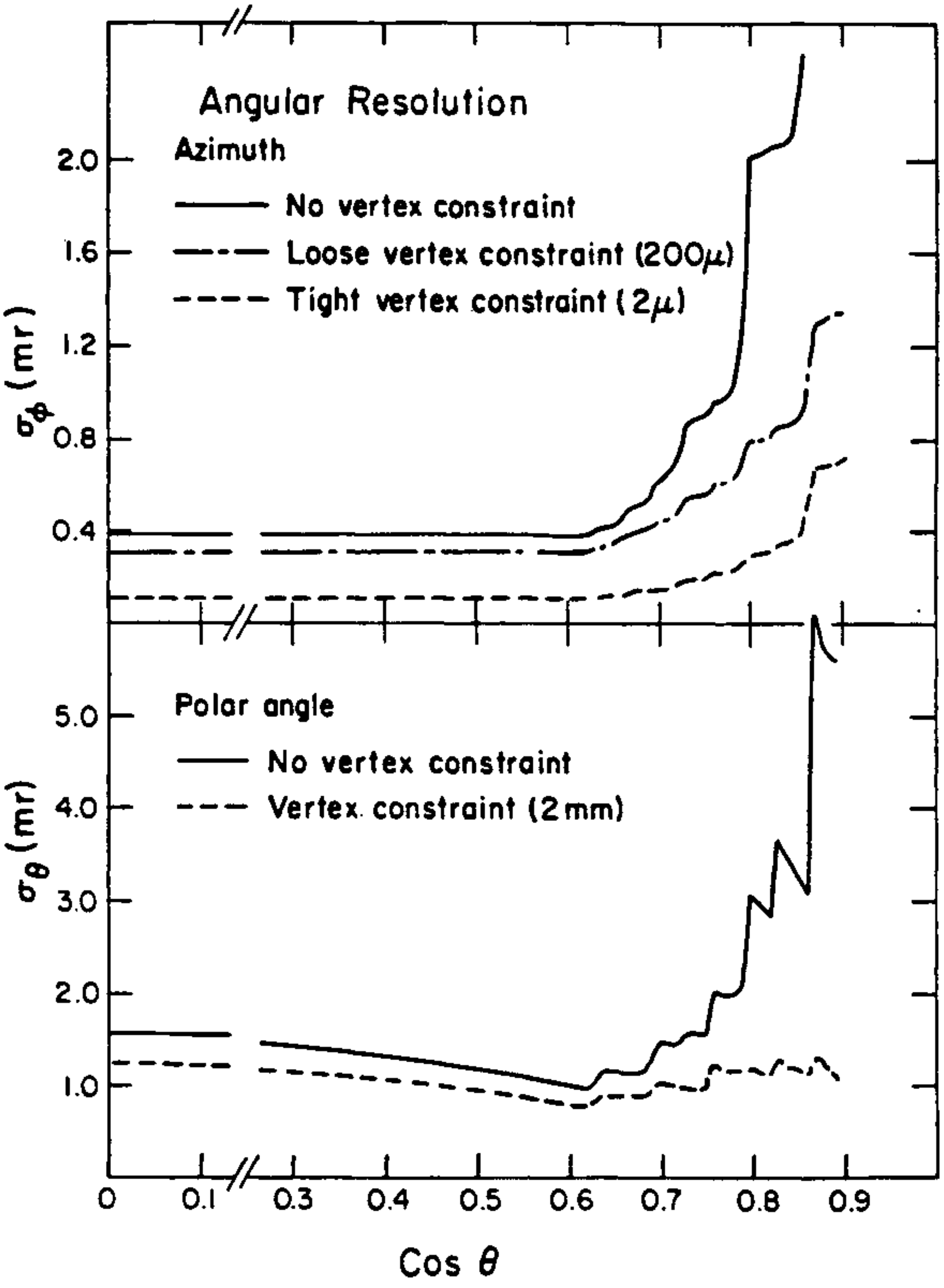

XBL 833-118

Figure 3.3b σ_θ, σ_φ as functions of cosϑ. The wiggles in these plots reflect the layer structure of the chamber.

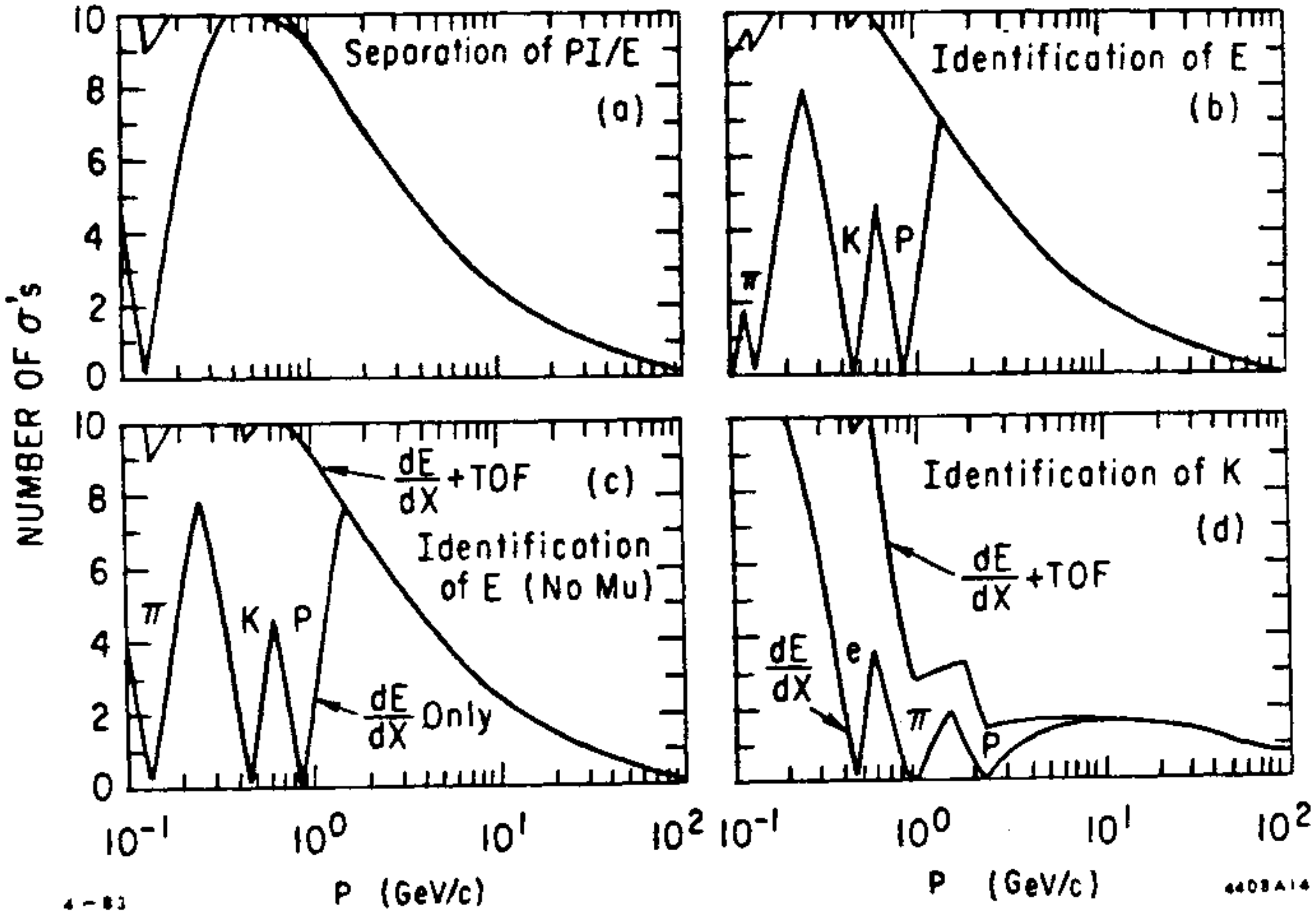

Figure 3.4a) $\Delta E/\sigma$ for π/electron as a function of momentum.

b) $\Delta E/\sigma$ as a function of momentum for electrons relative to the closest particle.

c) Same as b) with the improvement due to TOF with 200 psec resolution.

d) $\Delta E/\sigma$ for kaon relative to the closest particle. The improvement due to TOF with 200 psec resolution is also shown.

particles which traverse most of the chamber. In Fig. 3.3 we have indicated the effects of two types of vertex constraint, a tight one for tracks known to originate at the beam interaction point and a looser one applicable to tracks which could be secondaries of charm, tau or bottom decays. A precision σ_p/p^2 of 0.12% GeV^{-1} is achieved with vertex constraint over 65% of 4π solid angle. This increases to 0.45% GeV^{-1} at $\cos\vartheta = 0.85$. In our mechanical and electronic designs, we are setting specifications to ensure that systematic effects are small in comparison with these precisions.

Pulse height measurement of the sense wire signals will provide dE/dx measurement. Our calculated resolution is 6.9%. We have used the calculations of J. Va'Vra [3.1] to estimate how well we should be able to separate and identify particles by means of a dE/dx system with 72 samples of 8.33 mm size. The figure of merit is the quantity $\Delta E/\sigma$, which gives the number of standard deviations separation between pairs of particles, where ΔE is the difference in dE/dx between the particles and σ is the resolution in the dE/dx measurement. Figure 3.4a shows this separation as a function of particle momentum for the $\pi - e$ case. We find that from 200 MeV/c to 9 GeV/c the separation is better than 3 standard deviations. This means that for an 80% e tagging efficiency a 10 to 1 π rejection can be expected for momenta up to 12 GeV/c. Even for 50% worse dE/dx resolution, a very pessimistic assumption, we would have 10 to 1 π rejection up to 7 GeV/c. Unambiguous identification of a particle is more difficult, however, since all combinations of stable charged particles must be considered and the smallest separations of any pair must be used instead. Figure 3.4b shows this identification power for electrons. Although there are regions of poor identification around 140, 450, and 850 MeV/c, there is still good identification above 1.2 GeV/c. The poor regions can be eliminated when time-of-flight information is used. Figure 3.4c shows electron identification when dE/dx and time-of-flight (with resolution of 200 ps) are both used. The identification then extends from 100 MeV/c to 5 GeV/c to better than 4σ, and up to 8 GeV/c to better than 3σ. This mode of electron separation is completely independent of that provided by the liquid argon calorimeter which yields $e-\pi$ separation at about the per cent level above 1 GeV/c. Indeed the principal calorimeter limitation, namely photon-charged-hadron overlap, plays no role in limiting the dE/dx measurement. The combination of dE/dx and time-of-flight also provides some K identification as shown in Fig. 3.4d. K separation to better than 3σ is possible for momenta up to 1 GeV/c, and to 1.5σ for momenta up to about 30 GeV/c.

Active prototyping efforts to study accuracy of locations and tensioning of wires, electrostatic properties, pulse shapes, position resolution and high voltage connections are being carried out at SLAC and U.C. Santa Cruz. Design efforts for the various electronic components are being actively pursued at SLAC, U.C. Santa Cruz and LBL. The overall schedule calls for wire stringing in the fall of 1983 and installation in the Mark II detector at PEP in the summer of 1984. The chamber will be extensively tested and used for data taking at PEP prior to installation at the SLC.

The budget for the drift chamber is discussed in Section 8. The overall cost is $970K mechanical and $3,100K electronics.

3.3 Calorimetry

3.3.1 Barrel Region Calorimeter

Electromagnetic calorimetry for the solid angle $\cos\vartheta < 0.7$ is provided by the eight liquid argon modules now in the Mark II detector (Figs. 1.1, 3.5). We have used these calorimeters extensively, and their associated electronics and analysis programs are well understood and highly developed. The strengths of this shower counter system are the high degree of stability of the pulse height scale, the good energy resolution and the fine longitudinal and transverse segmentation. Each module is 14 rl thick and longitudinal shower development is measured by seven groups of layers ganged in depth (Fig. 3.6). The position of showers is reconstructed in these seven layers using ϑ, Φ, and U (at 45°) strips each typically 4 cm wide. The first layer of the system is at a radial distance of 1.8 meters. Further details of the modules are given in Appendix II.

The energy resolution (at normal incidence) for the modules has been measured as $\sigma/E = 12\%/\sqrt{E}$ for electron energies below 15 GeV. (See Fig. 3.7 and Appendix II.) For higher electron energies EGS simulations indicate that the resolution will increase to $\sigma/E = 15\%/\sqrt{E}$ at 50 GeV. These numbers are justified in Appendix II. For any calorimeter system the intrinsic resolution of the device for high energy electrons is quickly degraded by leakage out the back of the calorimeters and by small variations in the energy scale. For 50 GeV electrons the energy resolution for the liquid argon calorimeters is $\sim 25\%/\sqrt{E}$ without corrections for leakage (Fig. 3.8a). Because of the fine depth segmentation of the liquid argon calorimeters, a simple algorithm corrects for the leakage and reduces the resolution to $< 15\%/\sqrt{E}$. (See Fig. 3.8b and Appendix II). Likewise an uncertainty

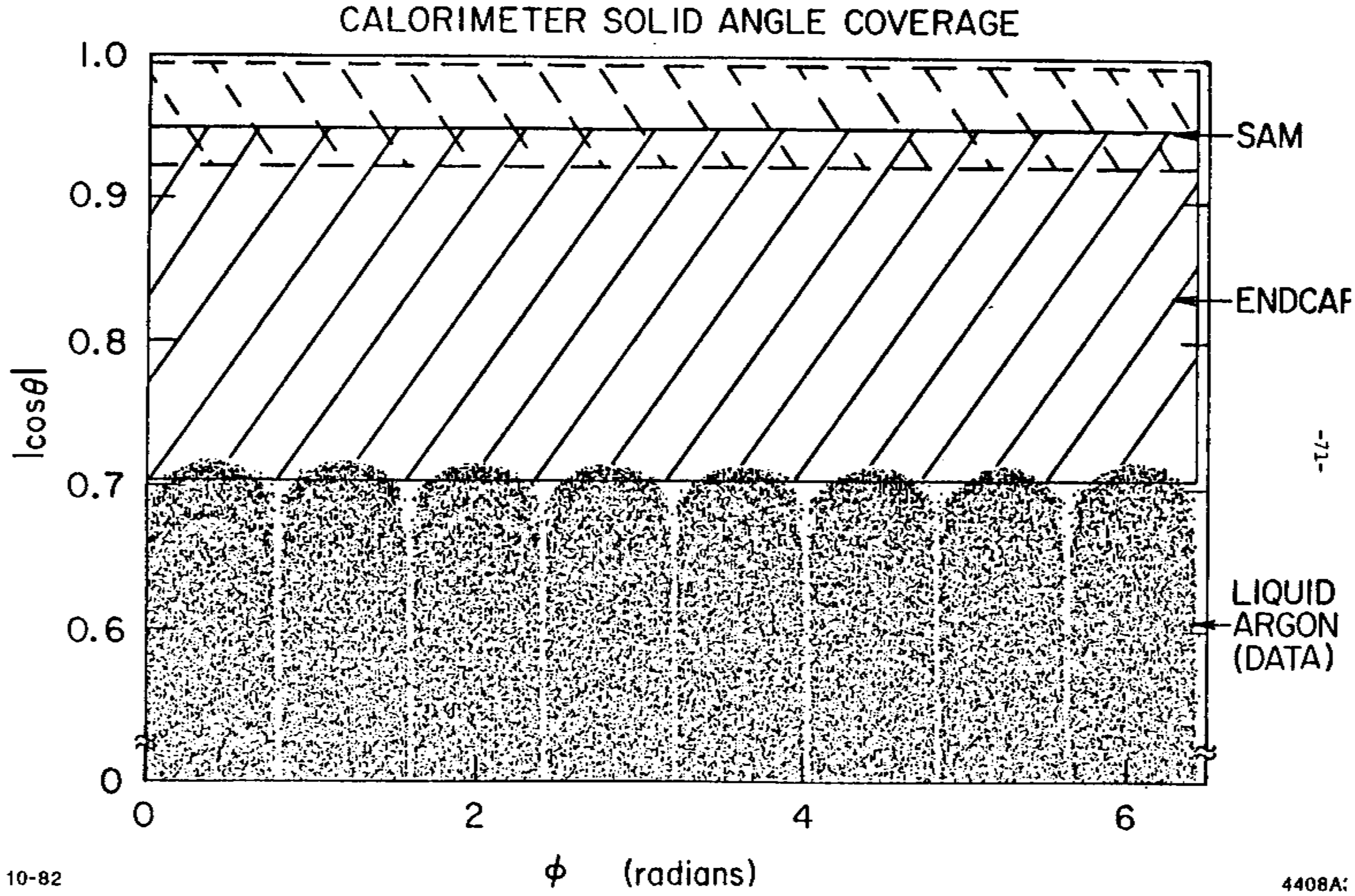

Figure 3.5 Solid angle coverage of the liquid argon calorimetry.

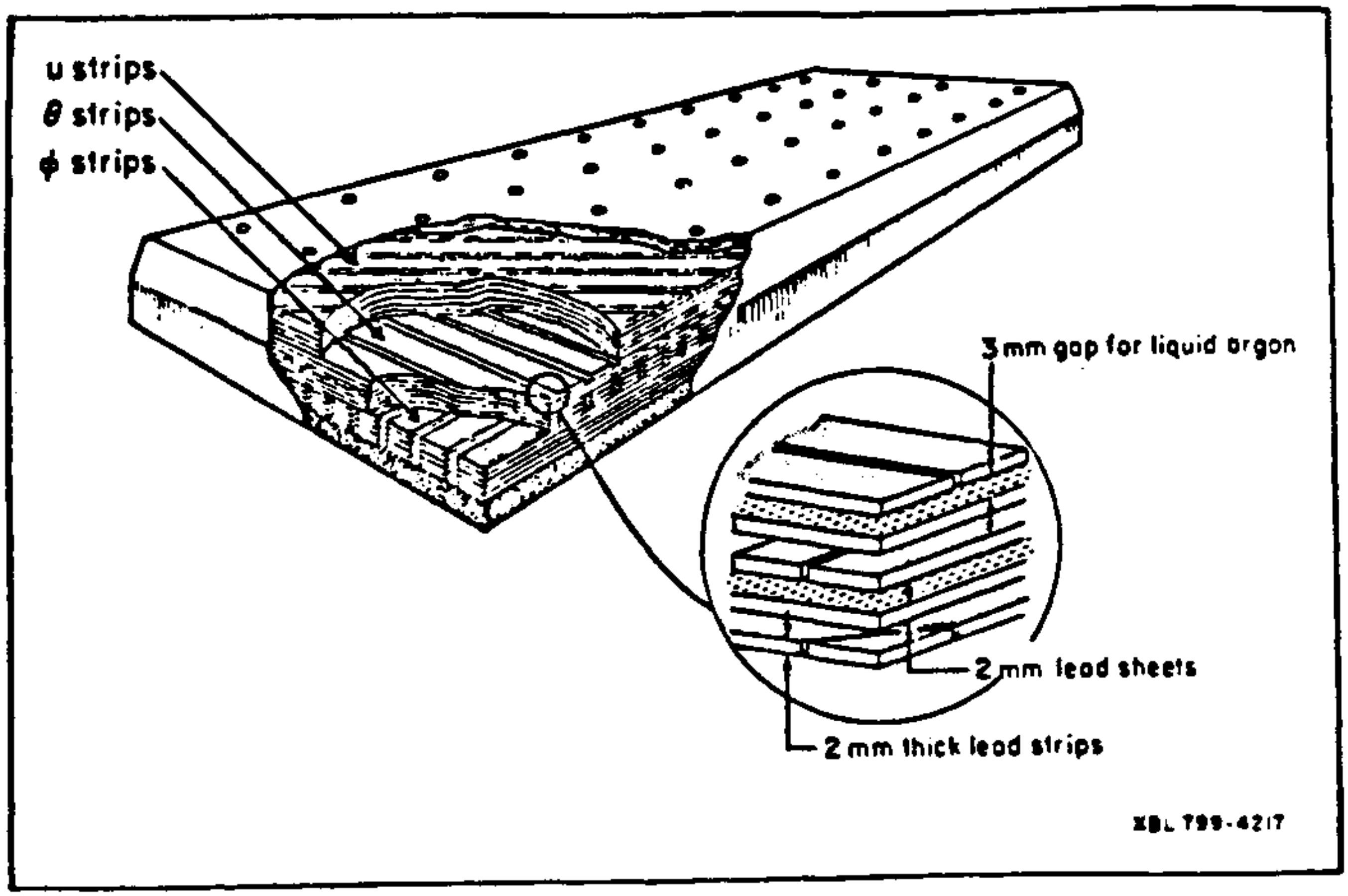

Figure 3.6a A schematic representation of a liquid argon counter showing layers of strips lying along the three coordinate directions.

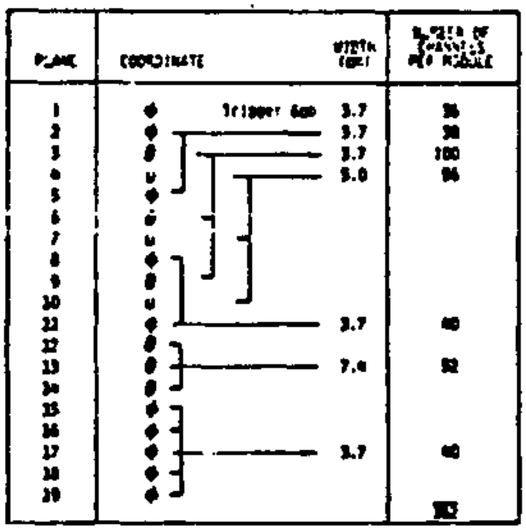

PLANE	COORDINATE		WIDTH (CM)	NUMBER OF CHANNELS PER MODULE
1	φ	Trigger Gap	3.7	36
2	φ		3.7	38
3	θ		3.7	100
4	u		5.0	96
5	φ			
6	θ			
7	u			
8	φ			
9	θ			
10	u			
11	φ		3.7	40
12	θ			
13	θ		7.4	52
14	θ			
15	φ			
16	φ			
17	φ		3.7	40
18	φ			
19	φ			
				[illegible]

Figure 3.6b Arrangement of strips in depth and the ganging scheme.

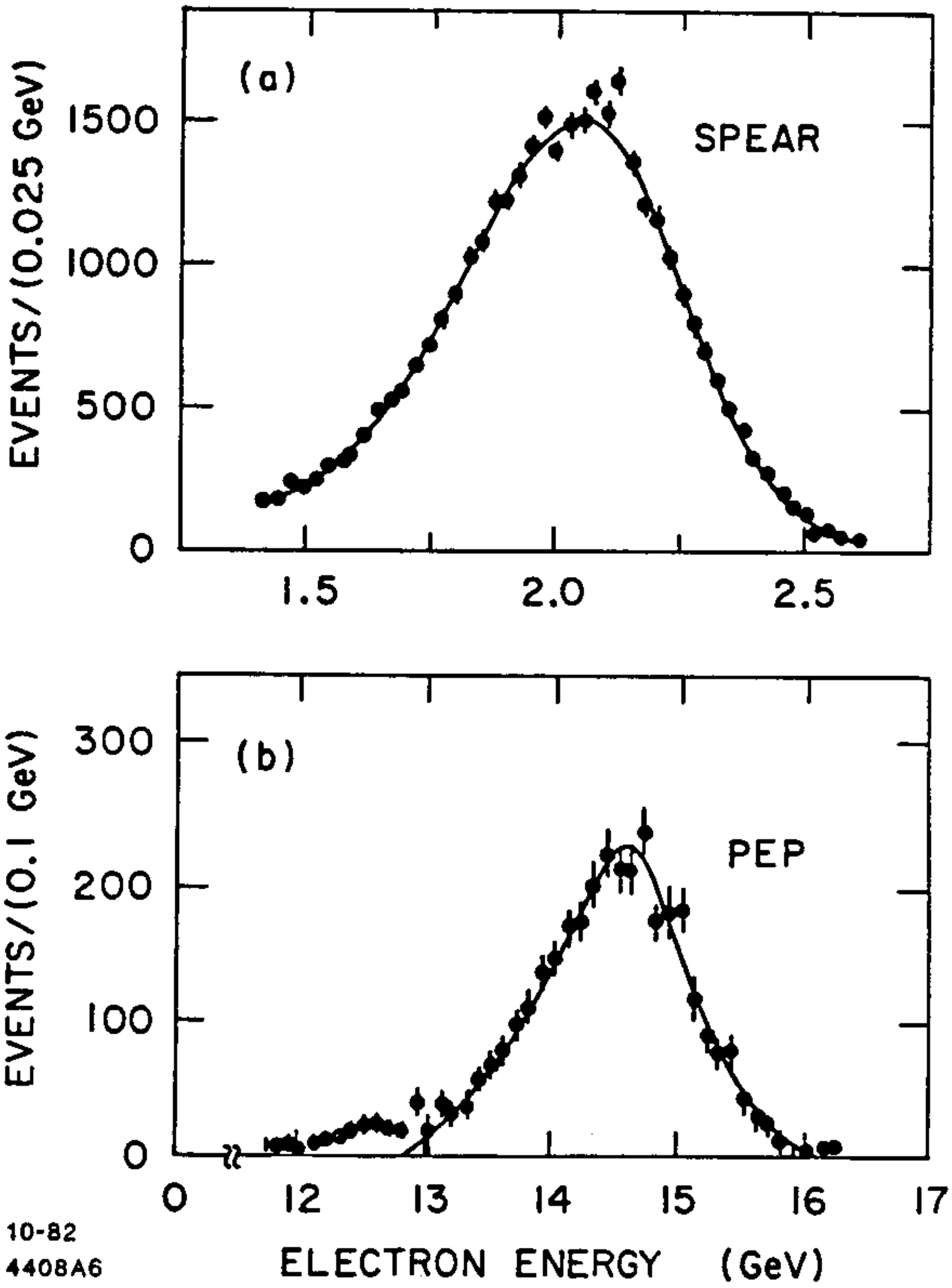

Figure 3.7 Energy resolution at normal incidence for the liquid argon calorimeter a) at SPEAR, b) at PEP.

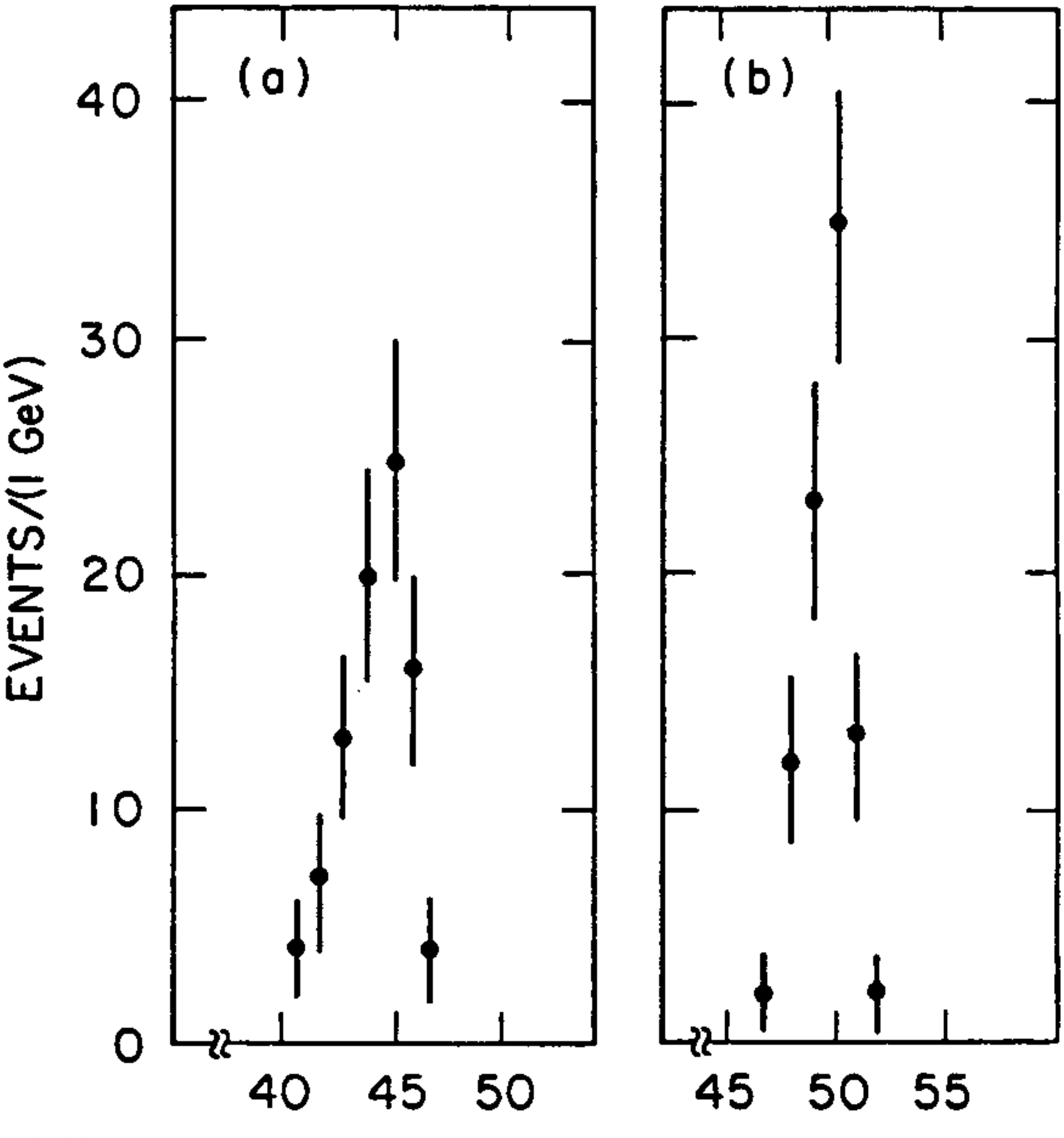

10-82
4408A1

Figure 3.8 Energy resolution of the liquid argon calorimeter for the 50 GeV electrons a) without correction for leakage, b) with the correction for leakage.

of 3% due to variations in the pulse height scale would correspond to a resolution of $21\%/\sqrt{E}$. We have measured the pulse height stability to be $<\frac{1}{2}\%$ over periods of many months.

Other properties of the shower counter system have been measured at SPEAR and PEP. For Bhabhas the angular resolution is $\sigma_\theta = \sigma_\phi = 3.5$ mrads. The all important hadron rejection has been extensively studied. For electrons in isolation (i.e., not buried in the heart of a quark jet) we measure the probability that a pion of momentum > 1 GeV will fake an electron is 0.4%. This is for a corresponding electron classification efficiency of ≥ 80%. Hence for isolated electrons we have rejection power of > 200:1 for momenta above 1 GeV/c. Using PEP hadronic events we find that in the center of the jets, the rejection rate is 50:1 Extrapolating this to the higher density SLC jets we expect rejection power of ~ 20:1 in the center of a jet. This by itself may not be sufficient to do some of the physics. However, when combined with the dE/dx and TOF measurement (2σ separation for momenta below 15 GeV/c), a rejection in the core of a jet of >500:1 will be achieved.

For the study of $Z^\circ \rightarrow$ hadrons (jet physics) the shower counters are best operated as calorimeters rather than individual photon finders. Using $Z^\circ \rightarrow$ hadron simulations run through current analysis code (i.e., no optimization for Z° energies) we find that the addition of the liquid argon energy to that of the charged particles improves the agreement between the found sphericity axis and the produced $q\bar{q}$ direction. The study of multi-jet events requires reconstruction of the jet directions and energies. The liquid argon barrel modules will improve the resolution of both these measurements and will not skew the determination of the jet axis.

3.3.2 Endcap Calorimeter

In this section we present a description of the endcap electromagnetic calorimeters (EEC) that we propose to build as part of the Mark II SLC upgrade.

I. Design Sketch and Performance Evaluation

After evaluation of several options we have settled on a design that is essentially the one given in our Letter of Intent. We plan to construct endcaps that are a good match in performance to the liquid argon (LA) barrel calorimeters. To that end we have chosen to use a strip geometry composed of individually extruded (or drawn) aluminum proportional tubes sandwiched between lead sheets as shown in Fig. 3.9. The tubes will be 0.9 cm × 1.5 cm in cross section and will be arranged to lie along four different coordinate axes: x, y, u, and v. Each endcap consists of 36 layers of Pb/proportional-tube, and each layer corresponds to half of a radiation length of Pb (0.28 cm thickness). This results in a total of 18 radiation lengths sampled by approximately 9000 proportional cells per endcap. The total number of electronic channels is ≈2500 per endcap. We are still evaluating various electronics options for the signal readout, but intend to place some emphasis on attempting to make the endcap digitizing electronics the same as that of the LA calorimeter. This will minimize the difficulties associated with operating and maintaining two different systems, and will facilitate the integration of the new endcaps into the Mark II data acquisition stream.

The design sketched above is a conservative one intended to minimize risk of delays and cost overruns associated with development of new techniques. Many of the mechanical features are based on the successful Mark

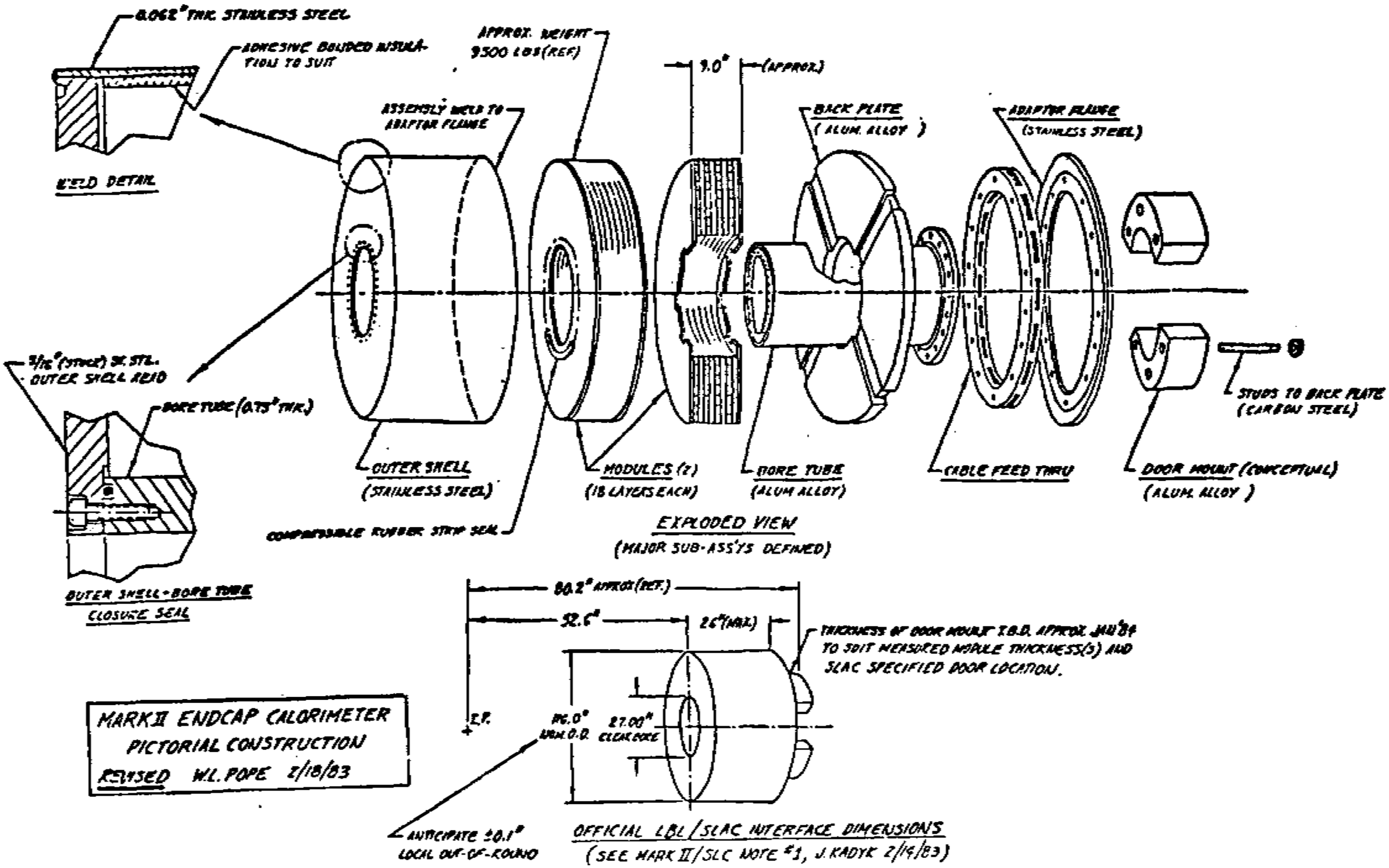

Figure 3.9 Details of calorimeter module assembly. (a) Expanded view of major components and reference dimensions. (b) Detail of submodule assembly showing layers, tubes and cabling. (c) Gas flow routing and electrical feed-through.

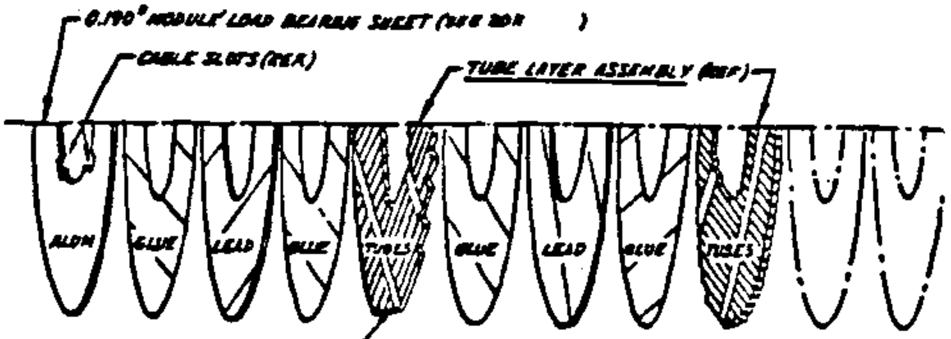

MODULE CONSTRUCTION

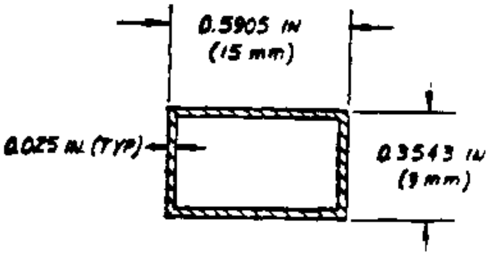

ALUMINUM TUBE DETAIL

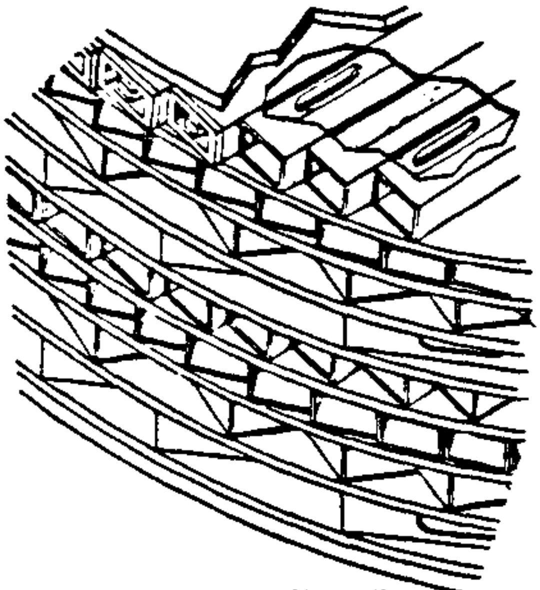

PICTORIAL OF A MODULE

OUTER CABLING PICTORIAL

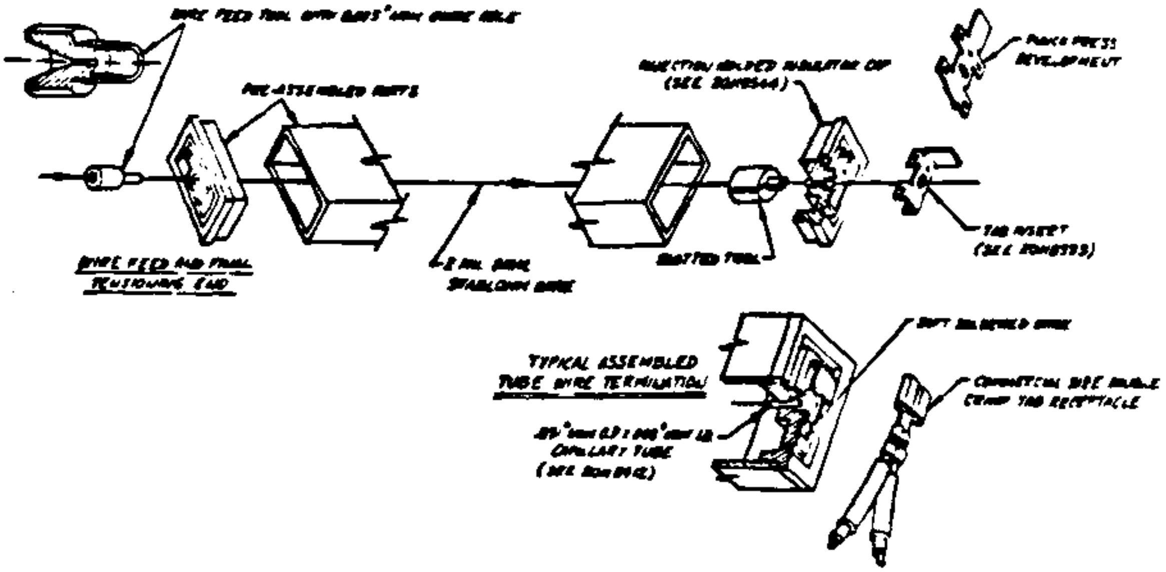

FIGURE 3.9b

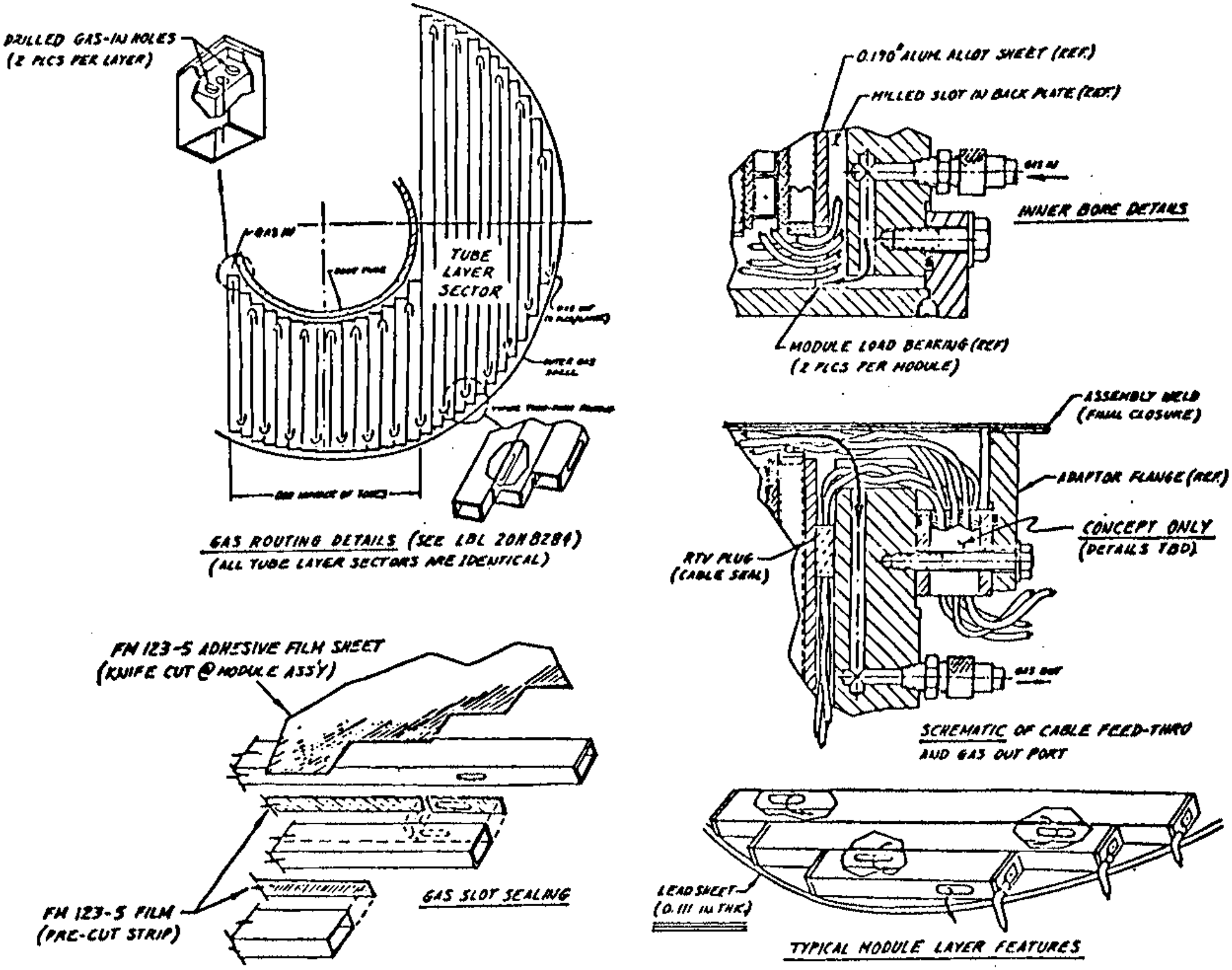
DRILLED GAS-IN HOLES
(2 PLCS PER LAYER)
GAS IN
TUBE
LAYER
SECTOR
OUTER GAS SHELL
GAS ROUTING DETAILS (SEE LBL 20N8284)
(ALL TUBE LAYER SECTORS ARE IDENTICAL)
FM 123-5 ADHESIVE FILM SHEET
(KNIFE CUT @ MODULE ASSY)
FM 123-5 FILM
(PRE-CUT STRIP)
GAS SLOT SEALING
0.190" ALUM. ALLOY SHEET (REF.)
MILLED SLOT IN BACK PLATE (REF.)
GAS IN
INNER BORE DETAILS
MODULE LOAD BEARING (REF)
(2 PLCS PER MODULE)
ASSEMBLY WELD
(FINAL CLOSURE)
ADAPTOR FLANGE (REF)
CONCEPT ONLY
(DETAILS TBD)
RTV PLUG
(CABLE SEAL)
GAS OUT
SCHEMATIC OF CABLE FEED-THRU
AND GAS OUT PORT
LEAD SHEET
(0.111 IN THK)
TYPICAL MODULE LAYER FEATURES

FIGURE 3.9c

III endcap calorimeters, while the similarity of the sampling geometry and segmentation to those of the liquid argon calorimeter should allow a fairly straightforward modification of existing software to be used for endcap tracking. We have also handled the details of the design in a way that will allow future upgrading of the endcaps by the addition of charge division on some or all of the wires. The total project is estimated to cost $1.5M (FY84 dollars), and we expect to have both endcaps installed and operational at PEP by the end of the calendar year 1984.

The important performance characteristics of these calorimeters are 1) energy resolution, 2) spatial (or angular) resolution, 3) electron identification, and 4) solid angle coverage. While, at low energy, the energy resolution of an electromagnetic calorimeter is determined by the sampling thickness, at high energy it is also essential to minimize the cell-to-cell variations in the response to the energy deposited by the showering particles. We have chosen to use individual tubes for each cell because it is easier for a vendor to maintain the required tolerance in the cross sectional dimensions of a single tube than in a multitube extrusion. As discussed in more detail below, the cell gain is most sensitive to variations in the smaller cross sectional dimension of the cell--this effectively determines the capacitance of the tube. Based on the experience of the Mark III, and the response from prospective vendors, we see no difficulty in obtaining extruded or drawn tubing with the required dimensional tolerances of ± .004". With due care in the fabrication of the endcaps and with proper calibration and monitoring, we expect to obtain an energy resolution for incident photons and electrons of $\sigma/E \approx 17-18\%/\sqrt{E}$ for 1 GeV $\lesssim E \leq 50$ GeV [3.2, 3.3].

The ability of the endcaps to separate electrons from pions is determined by the longitudinal sampling scheme employed and by the lateral size of the cells that are used. This latter parameter is most important since it determines the probability that a single cell will be hit by more than one incident particle. This is also an important factor in determining the effective energy resolution of the calorimeters in a multiparticle environment. The cell size in the endcap is somewhat smaller than that in the LA (1.5 cm instead of 3.8 cm), and we expect the e/π separation in the endcap to be as good as or better than that in the LA. Table 3.2 shows the result of a Monte Carlo analysis of the endcap performance for a tube width slightly larger than we have finally chosen (18 vs. 15 mm). This table gives the probability that a pion is misidentified as an electron as a function of the pion's total momentum and also its momentum transverse to the axis of the jet of which it is a member. Such a plot of P_T vs. P has been used successfully to study b and c quark production and fragmentation at PEP [3.4]. The tracking algorithm used to generate Table 3.2 was a relatively simple extension of the technique used in the LA. It can be seen that, except for the region of small P and P_T, the pion misidentification due to pile-up is $\lesssim 0.5\%$. The design choice of 15 mm for the tube width improves the π/e discrimination near the jet axis ($P_T < 0.5$ GeV/c, $3 \leq p \leq 11$ GeV/c) relative to that shown in Table 3.2 for an 18 mm width. Other quantities in the table are not changed appreciably. The electron detection efficiency remains nearly 100%. This will allow a clean separation of top and bottom quark jets from those produced by the lighter quarks. We have done this analysis for a wide variety of endcap configurations, including some using a projective geometry and some with charge division on the wires, and we conclude that the parameter that has the largest effect on these results is the width of the individual cells. Our endcap design attempts to provide the smallest cell size, consistent with a reasonable cost.

One of the desired features of the detector at SLC, is that it provides electromagnetic calorimetry matched to the charged particle tracking. This means that it is important to cover the region $|\cos\vartheta| \lesssim 0.90$ as completely as possible. In particular, we intend to minimize the "crack" at $\vartheta \sim 45°$ between the LA and the endcaps. Shown in Figure 3.10 is a plot of the number of samples and thickness (in radiation lengths) due to sampling layers in either the endcap or liquid argon calorimeter vs. polar angle. Each ECC layer corresponds to 1/2 of a radiation length at normal incidence, and so at polar angles near 45°, each sample corresponds to ≈0.7 radiation lengths. The solid angle coverage of the ECC and LA calorimeters overlap and for most applications the full power of the calorimetry should be available everywhere except for a small region near $\vartheta = 45°$ Even in this region the coverage will be adequate to provide a veto for detection of photons as needed, for example, in the neutrino-

TABLE 3.2

Probability of Pion Misidentification as Electron for the Endcap Calorimeter, for 18 mm Tube Width

		P_T(GeV/c)		
		0-0.5	0.5-1.0	>1.0
P(GeV/c)	1-3	4.6%	0.5%	—
	3-11	2.6%	0.0%	0.2%
	>11	0.0%	0.0%	—

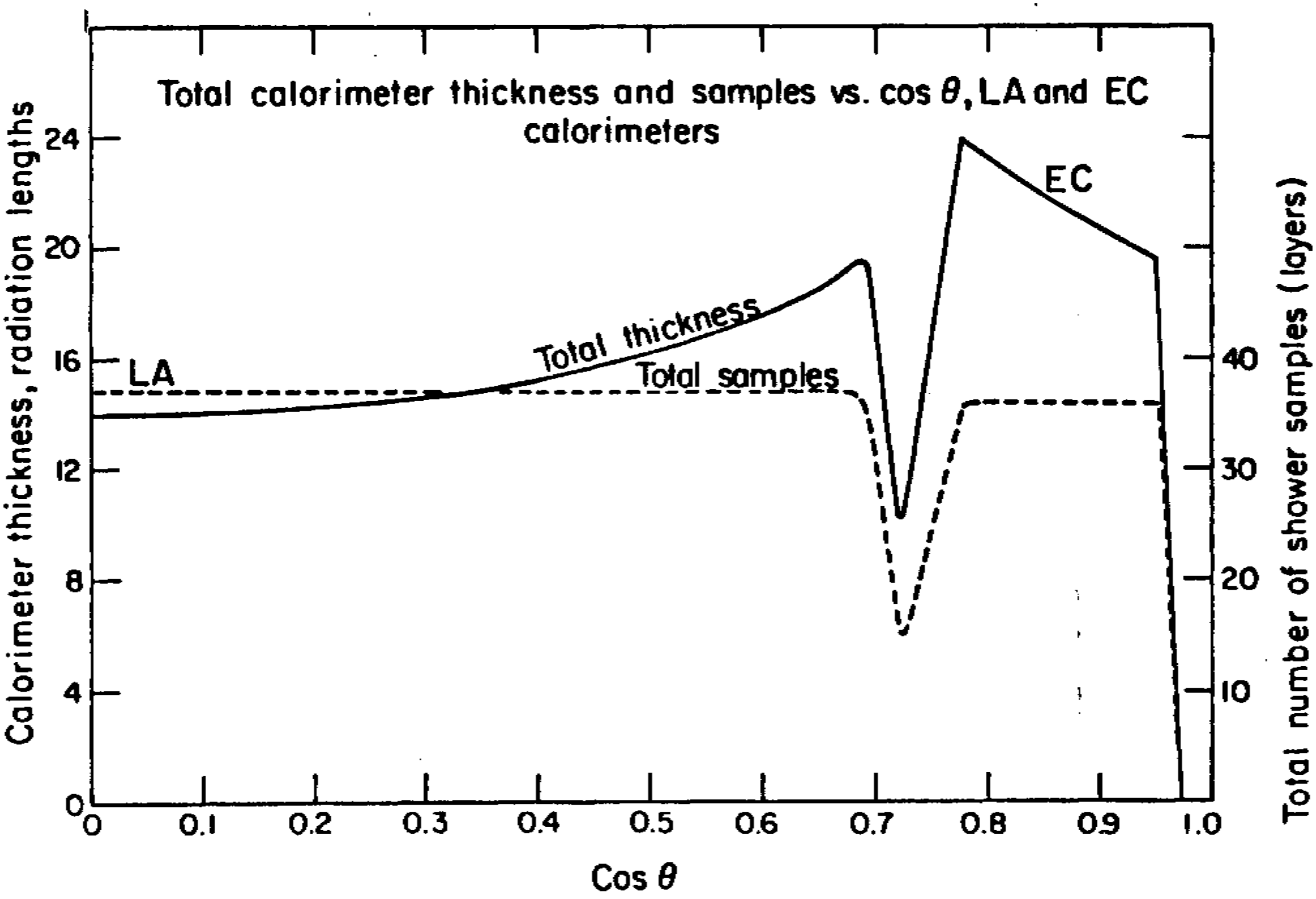

Figure 3.10 Liquid Argon and Endcap calorimeter thickness, in radiation lengths and number of sampling layers vs. cosθ for a ray originating from the interaction point (geometry only). This plot includes only the calorimeter absorber thickness and not, for example, the material in the coil or drift chamber endplates.

XBL 833-122

counting measurement.

II. Design Details and Specifications

A. Mechanical Design

A mechanical design of the endcap calorimeter has been completed by engineers W. Pope (chief design engineer), K. Mirk and G. Miner at LBL. Some pictorial representations of the calorimeter assembly and some of the subcomponents are illustrated in Fig. 3.9. In this section we present a detailed description of the endcap calorimeter design and comment on some of the considerations which helped to determine the design.

As illustrated in Fig. 3.9b, the calorimeter is constructed of layers of aluminum tubes sandwiched between layers of lead sheet. The tubes are glued to each other and to the lead sheet with strips of thermo-curing adhesive (American Cyanamide FM 123-5). This adhesive has been used successfully for similar applications on the Mark III calorimeters. Two submodules of 18 tube layers each are next formed by bonding this many layers of tubes and lead sheet between two face plates that transmit the weight loading to a central bore tube. An additional layer of tubes is bonded to the front face of the innermost submodule to detect γ conversions in the drift chamber endplate.

The face plates extend to a somewhat smaller radius than the tubes so that there is space available along the bore tube to bring out the electrical leads from the inner radius terminations of the tubes. These inner leads would be used only if charge division were utilized at a later stage, and for the present operation we plan to install a single connection to each tube at the outer radius. Both the high voltage and signal are carried on the same shielded lead, and each lead corresponds to one electronic channel, which is the sum of signals from several tubes ganged together. The ganging scheme will be studied using the Monte Carlo simulation program discussed earlier. Although the particular ganging will be chosen to optimize electron identification, it would be relatively simple to alter the scheme subsequently to emphasize different capabilities, or to upgrade the performance sometime in the future by bringing out more channels.

Gas is allowed to flow through the tubes as indicated in Fig. 3.9c. Each tube has a slotted hole near each end for the purpose of conducting the gas flow to the adjacent tubes. In this manner, gas is made to flow nearly the full length of each tube, and through many tubes in series before exiting. There are two such gas flow paths in parallel for each layer. The adhesive acts as a gasket around each slotted hole to seal the gas connection between tubes, as successfully demonstrated by our recent tests. However, this seal need not be "perfect", in that an overall gas seal is provided by the outer shell over the entire calorimeter. The choice of gas has not been made, but there are several gasses known to work well in calorimeters, e.g., 50% argon plus 50% ethane. There is also the possibility of using the same non-flammable gas which the drift chamber will use, viz. $A(89\%)+CO_2(10\%)+CH_4(1\%)$. Tests are in progress to guide us in making an optimal choice.

The sense wire is chosen to satisfy the need for reliability against breaking, and to be sufficiently large in diameter that the streamer mode could be used if desired. However, the voltage required increases with the wire diameter, other parameters being held constant, so that this sets an upper bound. A reasonable size satisfying these requirements is about $50\mu m$ diameter. Experience of the Mark III group has shown that Stableohm (trademark) wire (75% Ni + 20% Cr + Cu + Ag) is very reliable against breaking and works well in the charge division mode. We plan to use this wire to allow this technique as a future option, if desired.

The feed-through insulators at each tube end are designed to hold the wires by soldering, a method used successfully in numerous similar applications, and known to provide a reliable electrical connection; mechanical integrity is provided by gluing the wire ends with epoxy. The tension will be established in the wire at one tube end before soldering. The Valox (trademark) plastic insulation material has also been used successfully in the Mark III design. The feed-throughs will have a metal piece molded onto or clipped onto the plastic for mechanical rigidity, and this piece provides the wire end support as well as a clip-on terminal for attaching the signal/high voltage lead. The wire position is determined by the capillary tube of small inside diameter, molded in a precision hole in the plastic itself.

The mechanical tolerances necessary to avoid degradation of the intrinsic resolution of the calorimeter have been determined by calculation, and from previous experience [3.3,3.5]. The gas gain is very sensitive to the electric field in the region of the avalanche at the wire surface. Previous measurements, as well as our own (described later), indicate that $\frac{d(\text{Gain})}{\text{Gain}} = \alpha \frac{d(\text{Voltage})}{\text{Voltage}}$, with $\alpha \approx 10-15$. The surface charge on the wire, which determines the field at the wire, is determined by the <u>capacitance</u> between the wire and the tube. This in turn is affected by: 1) the wire position inside the tube, 2) the tube diameter or cross-sectional size, and 3) the wire diameter, in order of increasing sensitivity. We have set the tolerances by requiring that each of these individual variations contribute no more than 1% to the overall calorimeter resolution. This amount is chosen to be small but comparable to the best achievable fractional resolution; $\frac{\sigma(E)}{E} \simeq 2.4\%$ at $E = 50$ GeV. It is assumed that the tube-to-tube gain variations in successive layers that sample the shower will tend to average out errors. This leads to about a ±5% tolerance on the gain of any given tube. These tolerances translate into requirements of ~.02" in wire placement (along the smaller of the tube dimensions), ~.004" in tube size (again in the smaller dimension), and ~1% in the wire diameter. Although the wire diameter tolerance seems severe on an absolute scale of size, it is compatible with presently achievable fabrication techniques. The wire placement tolerance is not very demanding, and perhaps the tube size (gap height) tolerance will be the most difficult to achieve. There is indirect evidence from several sources that these mechanical tolerances are the most important elements in determining the calorimeter energy resolution and that it is very important to achieve them. Means of monitoring these mechanical tolerances during procurement and fabrication are being developed.

The signal and high voltage are conducted on the same coax lead from each set of sense wire gangings, and each such channel lead is brought to an electronic box on the endcap where the HV is isolated by a blocking capacitor. The metal connector on the tube feed-through insulator provides two friction-tight push-on connections, one for this channel lead and the other to "daisy-chain" the other sense wires in the ganging. These cables (e.g. RG174) are each about 0.10" diameter, and are available as flat woven cable braids. The ensemble of braids is brought parallel to the beam axis along the outer radius to the back plate where the leads exit the main enclosure via feed-through insulators that form a gas seal. The gas pressure will be only slightly above atmospheric within the calorimeter outer shell, so that gas leakage problems should be negligible. The channel leads finally pass out of the detector through a set of fourteen 5" diameter holes spaced uniformly around the endcap, and enter electronics boxes mounted on the endcap door, where HV blocking capacitors separate the dc and ac components.

Examination of Fig. 3.9a will show that the major weight load of the calorimeter, about 10 tons, is carried via the face plates to the 27" diameter (aluminum) bore tube, which is bolted to the back plate. The back plate is bolted to the endcap steel leaving space for the cables from both inner and outer radii to reach the gas shell feed-through insulators. The ECC module is mounted on the end door as shown, and the entire combination, weighing about 30 tons, is moved axially outward by about 2.3 m when access to the inner part of the Mark II detector is desired. Two supports hold the endcap door on a linear gear and motor driven ratchet mechanism for retracting the endcap. Such design has been used successfully in the TASSO detector.

The endcaps completely encircle the beamline, and in particular do not have fixed "keyways" to support the beam pipe. The problem of supporting the beam pipe must be solved for operation at PEP as well as the SLC. In the former case, the support of the beam pipe is not very critical, since the positions of the insertion quadrupoles are not disturbed by the motion of the endcap. On the other hand, there is a considerable weight of tungsten and lead shielding on the beam pipe between Z = 2.6 and 4.8 m, which must be supported. In the case of the SLC beam pipe, the insertion quadrupoles will most probably be located within the range of the motion of the endcaps. The 21" diameter hole in the endcap is large enough to clear these quadrupoles during the endcap retraction, but the tolerances on the positions of these magnets are quite stringent. The shielding has not yet been designed in the SLC case. A solution appears to be possible that works for both cases. Two supports are needed on each end of the detector, a permanent one located beyond the endcap motion, at about 5 m, and a removable support located just outside the endcap, at about 2.6 m. The latter support might attach to the endcap, or to a permanent base (the Mark II mainframe or the ground), but would be easily and quickly removable, and doweled into a fixed position. During the retraction these supports are removed allowing the beam pipe to sag slightly. However, the pipe can be made strong enough to be self-supporting between $Z \simeq +5$ m and $Z = \simeq -5$ m. After the door is returned to its normal position, the removable supports are replaced and the appropriate dowel pins are used to reposition the quadrupoles to ≈ 50 μm accuracy. This is sufficient to allow a raster scan of the SLC beams to bring the beams back into collision. This design is predicated on the assumption that for the SLC case, a precise repositioning procedure will be needed to bring the beams back into collision after a shutdown no matter what mounting scheme is used.

B. Electronics and Signal Readout

The requirements on the electronics are partly determined by technical considerations such as dynamic range, noise, etc., and partly by cost. As stated earlier, it is desirable to use digitizing modules which are the same, or as similar as possible to those used for the liquid argon barrel calorimeters, in order to avoid unnecessary duplication of effort in design, maintenance and understanding of their operation.

The range of measured energy will be larger at the SLC than at PEP and the electronics used on the electromagnetic calorimeters must be able to handle the correspondingly larger range of signals. The lower end of the range is determined by the need to detect minimum ionizing tracks while the upper end is set by the need to avoid saturation of individual channels at incident energies near 50 GeV. We are still evaluating this problem for various ganging schemes in the endcap, but we believe that it will be desirable to obtain a range in the electronics that is equivalent to 14-15 bits. We are investigating the possibility of using non-linear amplifiers, as well as configurations of linear amplifiers with 15-bit ADC units. A number of amplifier designs can be used to provide a non-linear response, but we have not yet completed an evaluation of this option. Extended ADC units are now coming on to the commercial market, and, in particular, we are studying the suitability of the LeCroy series 1800 FASTBUS ADC's for our needs. (The new drift chamber electronics will use TDC modules in the same series.) We are also considering the possibility of upgrading the present 12-bit BADC/SHAM system that is used on the liquid argon system.

Noise considerations are more benign in the ECC relative to the liquid argon calorimeters. This is because the gain obtained in the avalanche process (10^4–10^5) raises the signal far above the ambient noise background from electronic pickup and circuit noise. Although care must be given to insure proper shielding against electrical noise, there is not nearly the vulnerability that exists in the barrel calorimeters, which operate as ionization chambers with unit gain. It is even possible that no amplifiers will be needed at all for the ECC if they are operated in the saturated avalanche mode. This would further decrease cost and the potential maintenance problems associated with close-in amplifiers. We are still evaluating this option.

The leads carrying both the HV and signals from the ECC will be coaxial cables. They have been used successfully in similar applications at the CLEO and Mark III detectors. These cables carry the ganged signal, the ganging of layers having been made at the outside radius of the calorimeter module, and they terminate at dc blocking capacitors inside of the electronics boxes, which are on the outside of the endcap door. The average length of these HV/signal cables will be about 3 m. Inside the electronic boxes are amplifiers (if they are necessary), HV connections to each channel through a very high resistance (to provide isolation in case of a short), and the calibration system (see below). The non-linear response network may also be located here (in lieu of a BADC modification). The transmission of the ~ 5000 signals from the electronics boxes to the digitizing modules in the LEACH will probably be done with shielded cables each consisting of many twisted pair leads.

C. Calibration

The calibration scheme involves two distinct parts: 1) electronics calibration, accomplished by injecting standard test pulses into the input of the electronics system inside the electronics box, and 2) a system for monitoring and correcting the gas gain, which is a sensitive function of HV, pressure, temperature, and gas composition. This method of electronics calibration is now used successfully for the calibration of the liquid argon calorimeters, as well as for the Mark III calorimeter calibration. However, the calibration of gas gain is new to the Mark II, and we plan to adopt the method used by the Mark III group. In their scheme, the gas gain is monitored using a small wire test cell having the same cross-sectional geometry as the calorimeter sampling tubes, but much shorter in length. This cell, external to the calorimeter, is operated with the same gas (in the same series gas circuit) as the detector calorimeters, and its gain is continuously monitored by the position of the pulse height spectrum from an Fe^{55} source inside the cell. This cell (or cells: one at entrance and one at exit of the gas path) monitors the effect of the gas composition, pressure and temperature, and is successfully used in the Mark III experiment to correct the overall gain variations to the ≈1% level [3.3]. This level of gas gain calibration is necessary in our case ($\frac{17\%}{\sqrt{E}} \simeq 2.4\%$ at $E = 50$ GeV).In the Mark III experience, it has been sufficient to monitor only the pressure (due to atmospheric pressure changes) to establish the 1% level of calibration, other variations (HV, temperature and gas composition) being controlled to a high level of reliability. Nevertheless, the gas gain monitors are an important check on the performance. Geometric sources of gas gain variations, such as tube and wire size, and wire location have been discussed earlier and must be carefully controlled during fabrication.

After one (or perhaps each) of the ECC modules is completed, it will be tested thoroughly in a beam to determine its performance. This will include response to electrons, pions and muons over as wide an energy range as available. Tests will be made at different angles of incidence, and different positions, particularly to map out response at the "edges" (inner and outer radii). It should not be difficult at this time to confirm the expected gain variations due to pressure and gas composition, if desired, although this should be no different than measured in the current lab tests. The main objective of these beam tests on a full module is to have an accurate knowledge of the ECC performance, so that this may be used for the physics analysis. In addition, it serves as an important monitor to detect any indications of malfunction during the experiment, by sensing deviations from the expected performance.

D. Laboratory Tests

In order to fully understand the operation of the individual sampling tubes in the ECC, a set of measurements are in progress using a single 2 m long tube of the type used by the Mark III experiment. A 50 μm diameter tungsten wire was strung in this tube under 100 g tension, and signals measured under a variety of conditions. A highly collimated Ru^{106} beta source (2mC in strength) was used as the probe of the tube response. The source holder collimates the beta rays to about 30 mr (rms), and they are required to trigger two scintillation counters, with ≈ 1/8" diameter sensitive regions, one placed above and one below the tube under test. A substantial fraction of the beta ray spectrum (3.55 MeV endpoint energy) has sufficient energy to allow the necessary penetration of the bottom scintillator, the two tube walls (.025" of Al each), and to enter the top scintillator. A typical counting rate is about 8 counts/sec., with essentially no background. Certain of these measurements which could have impact on the mechanical design were done first, and have led to useful and encouraging results. For example, the aspect ratio of the tube under test is 2:1 (width:height), and it is found, by a transverse scan of the tube, that there is negligible positional dependence in charge collection from the ion trails left by the beta track provided that a gate length of at least 300 ns is used. Our actual design specifies a tube of smaller linear dimensions (9 × 15 mm) than the tube being tested (13 × 28 mm). We have found that a decrease in charge collection occurs within about 1/2" of the end of the tube (which should be about 3/8" in the actual design), but that useful sensitivity extends to within 1/8" from the end of the sense wire. Another test has determined the sensitivity of gain to wire voltage for the gas mixture 50%A + 50% C_2H_6:

$$\text{Gain} = (\text{const.})\, V^{\alpha},$$

where $\alpha \cong 10-15$, depending on the operating voltage (see Figs. 3.11-3.13).

In addition to the geometric tests, some investigations of other gas compositions will be made. In particular, a study will be made of the

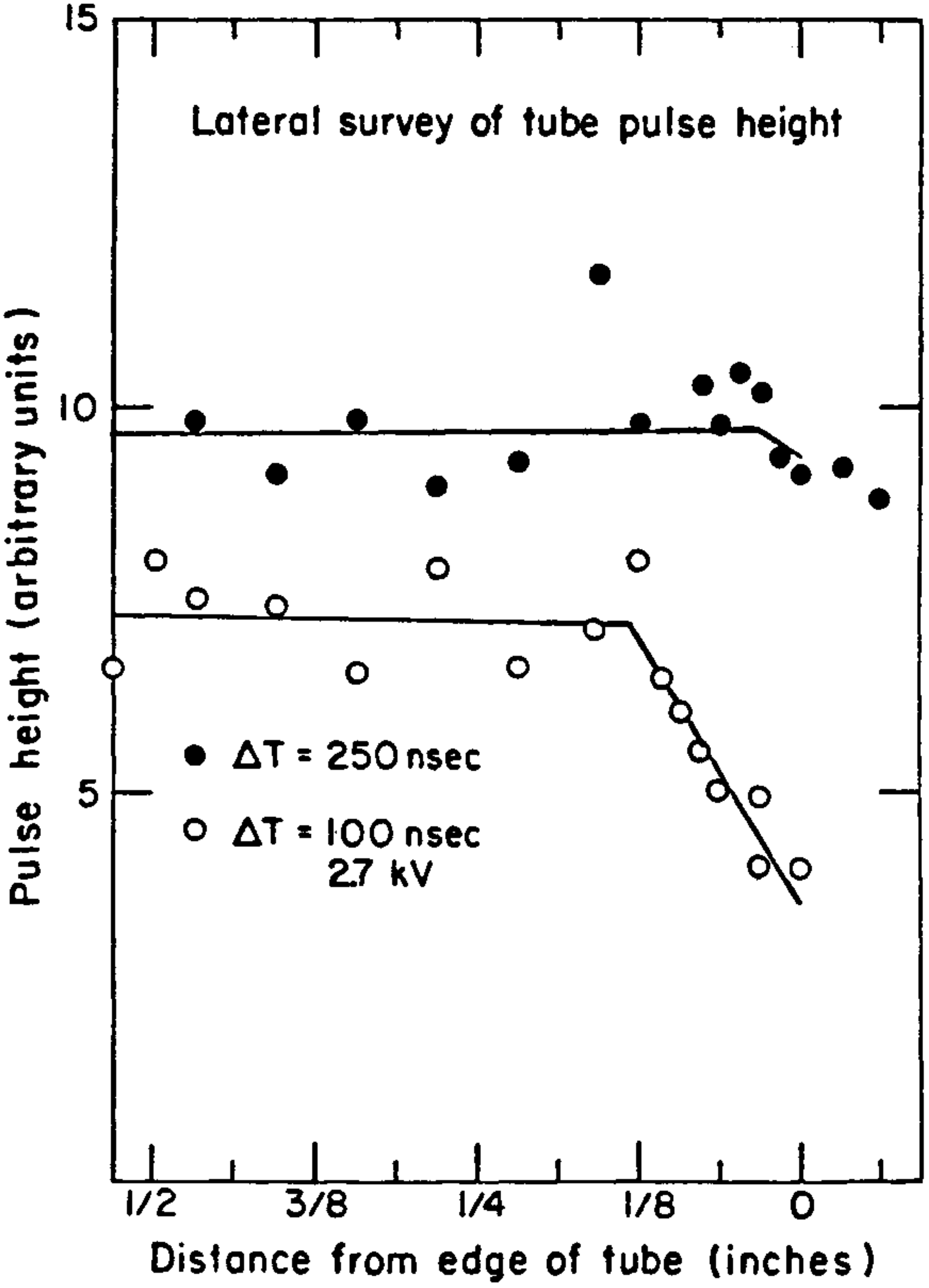

Figure 3.11 Response of a test sampling tubé (13 × 28 mm in cross section) to beta ray source vs. lateral position of source. Gas: A (50%) + C_2H_6 (50%). Wire: 50 μm diameter tungsten. HV: 2700 v. Source well-collimated Ru^{106} and two-fold counter coincidence.

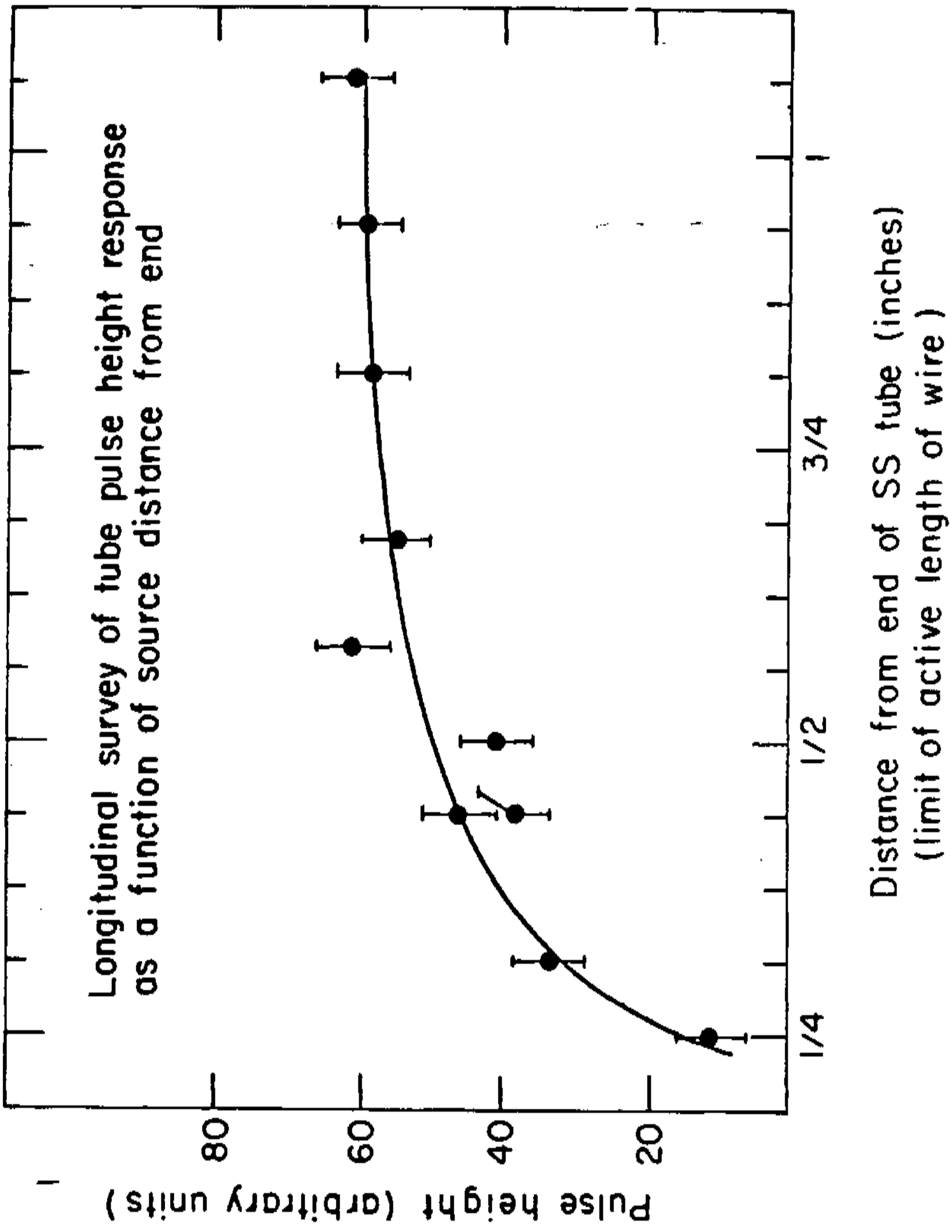

XBL 833-120

Figure 3.12 Response of a test sampling tube vs longitudinal position of source. Other conditions as in Figure 3.11 above.

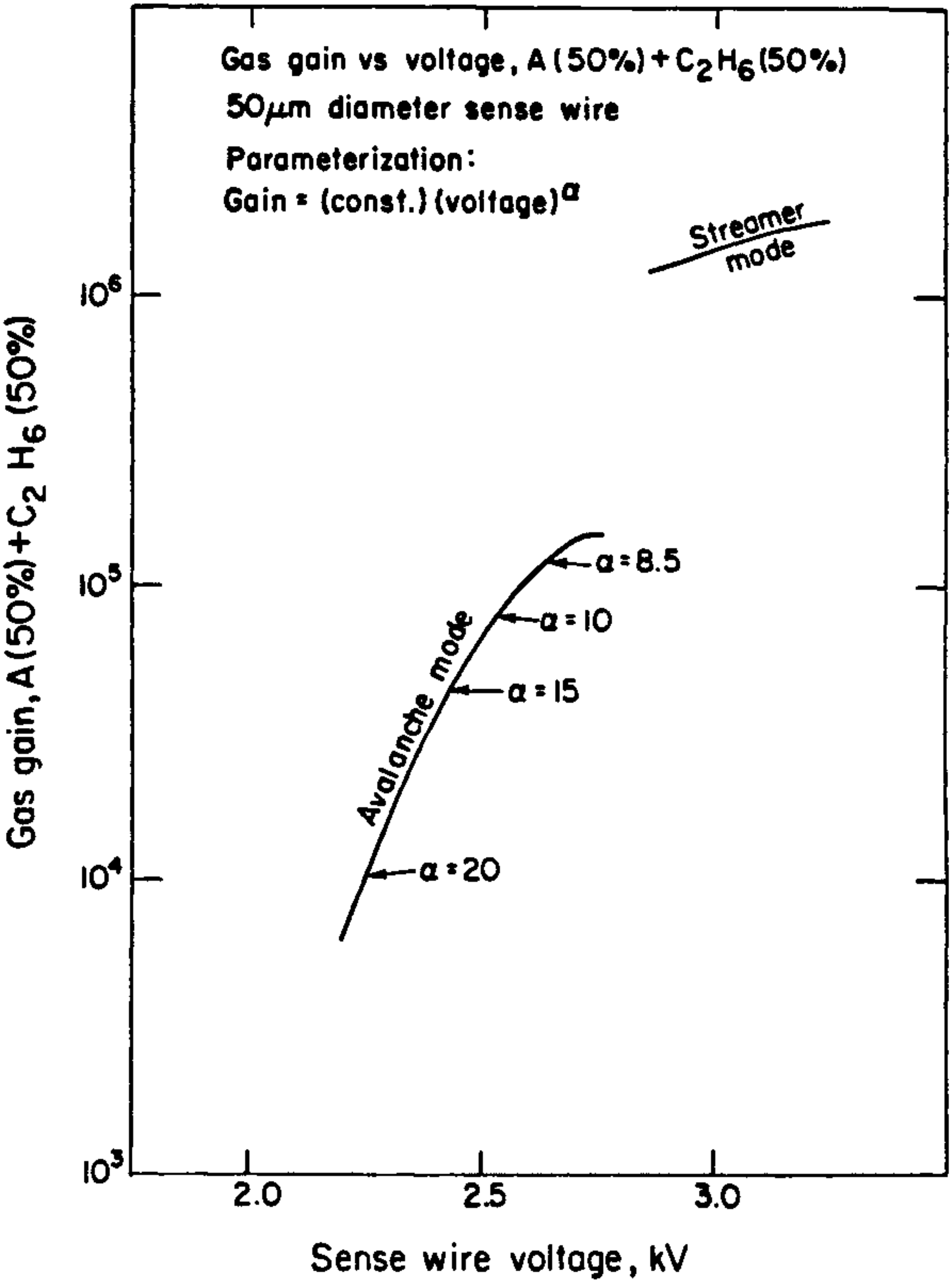

Figure 3.13 Gas gain of sampling tube vs. HV. Other conditions as in Figure 3.11 above. (Measurement of other candidate gases is in progress.)

usefulness of ethanol as a constituent in small amounts to quench photons that would otherwise cause secondary discharges originating at the tube walls. Such a phenomenon has been observed to occur at the high voltage of about 2700V without alcohol present in the mixture. Running at higher gain may eliminate the need for amplifiers, and may improve energy resolution as well by suppression of the contribution of delta-rays [3.2]. The choice of gas composition has little impact on the design of the tube and lead assembly, although it could affect the electronic design and is currently under investigation.

III. Budget and Schedule

The design of the endcap given in the previous section is the result of a detailed study of cost vs. performance as functions of various parameters. A computer program was developed which used as input information the best available cost estimates for labor and materials, and the per unit estimates of effort required in the various stages of assembly. It was then possible to make cost comparisons between designs by varying the physical parameters of the calorimeter, such as lead thickness, tube width, etc., and to make a choice based on the predicted cost for a given performance. As an example, a set of curves giving the cost per endcap is given in Fig. 3.14. In this case, the total lead thickness in the calorimeter stack was fixed at 4 inches, corresponding to the ≈ 18 radiation lengths necessary to contain electron showers at SLC energies, and the tube aspect ratio was fixed as width/height = 1.8. There is little advantage in using a larger ratio since (a) the maximum tube width is dictated by the particle pileup, and (b) there is ample space for the total depth required (along Z) in the calorimeter when this ratio is equal to about 2. Moreover, the required mechanical tolerances

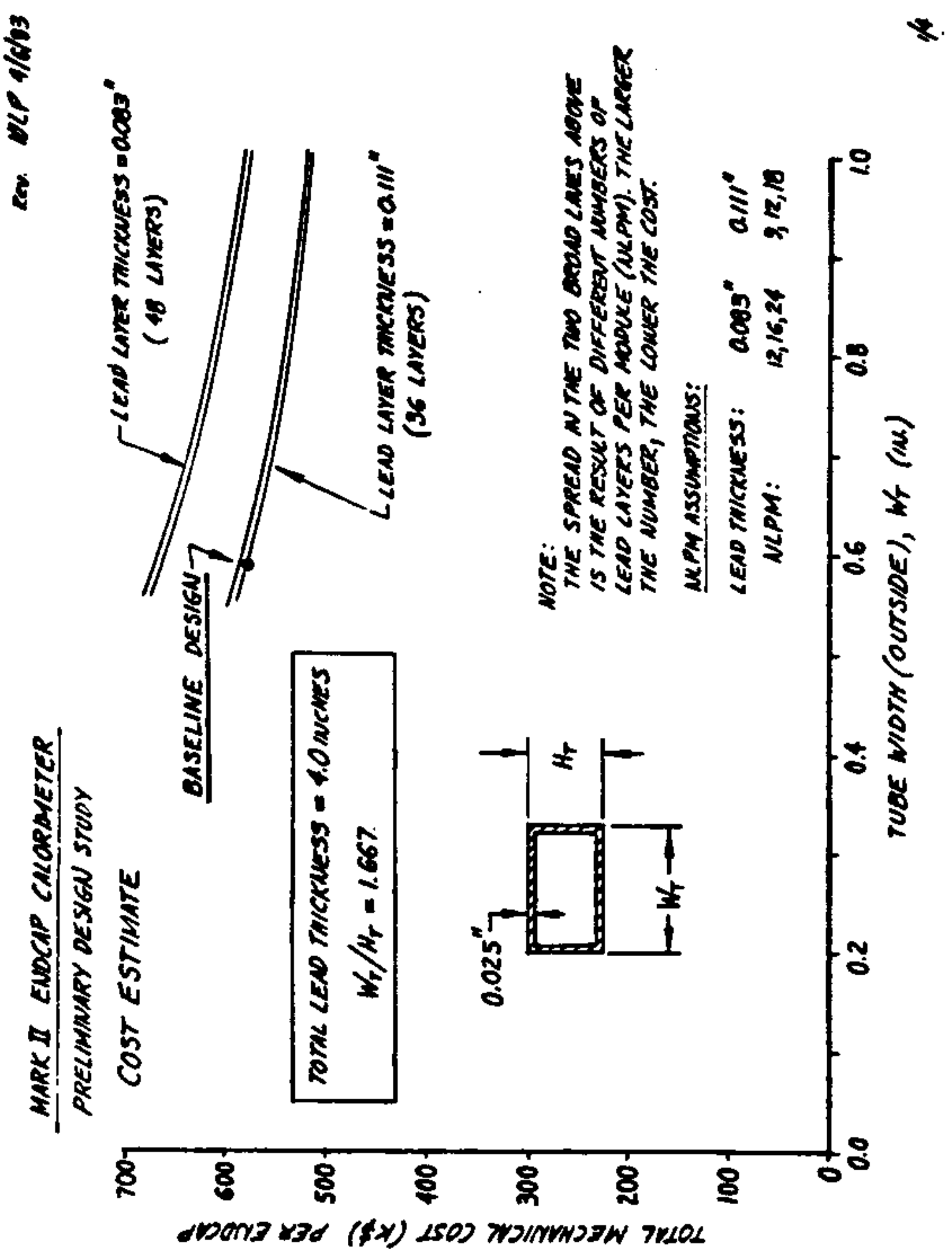

Figure 3.14 Total mechanical cost vs. tube width, for fixed tube cross section aspect ratio and fixed total lead thickness.

due to gain variations are less for smaller ratios. The curves in Fig. 3.14 give the cost per endcap in FY84 dollars, assuming 7% inflation per year (plus 20% contingency), vs. the tube width for assumed lead thicknesses of $0.38X_0$ and $0.50X_0$. The selection of a width of 15 mm is based upon the Monte Carlo study of pileup discussed in Section 2, and the choice of the lead thickness is based on the energy resolution desired ($\approx 17\%/\sqrt{E}$).Electronics costs are estimated as $60/channel and assume $10/channel for cables and connectors, plus the HV and calibration systems. The preamplifiers are estimated to cost $10/channel.

The schedules of cost and effort are given in Figures 3.15 and 3.16. In Fig. 3.15 the spending profile is shown for the nominal installation schedule called the "baseline" schedule, which corresponds to installation of both endcap calorimeter modules during the summer 1984 shutdown at SLAC. A more stretched-out installation schedule is represented by the profile in Fig. 3.16, where one module is installed in summer '84, and the other during the Christmas '84 shutdown. In this latter case, 20% of the total cost falls into the 1985 fiscal year, while in the baseline schedule all costs are incurred in FY83 and FY84. Both of these profiles are idealized in that purchases have been concentrated at certain convenient times, such as fiscal year boundaries, when in fact they will probably be distributed more uniformly. There are additional uncertainties simply because of the difficulties in making precise cost and delivery estimates. However, the total mechanical design and fabrication cost is known much more precisely. The electronics cost has a greater uncertainty since it is based primarily on costs from other experiments, and the details of the electronics system have not yet been clearly specified.

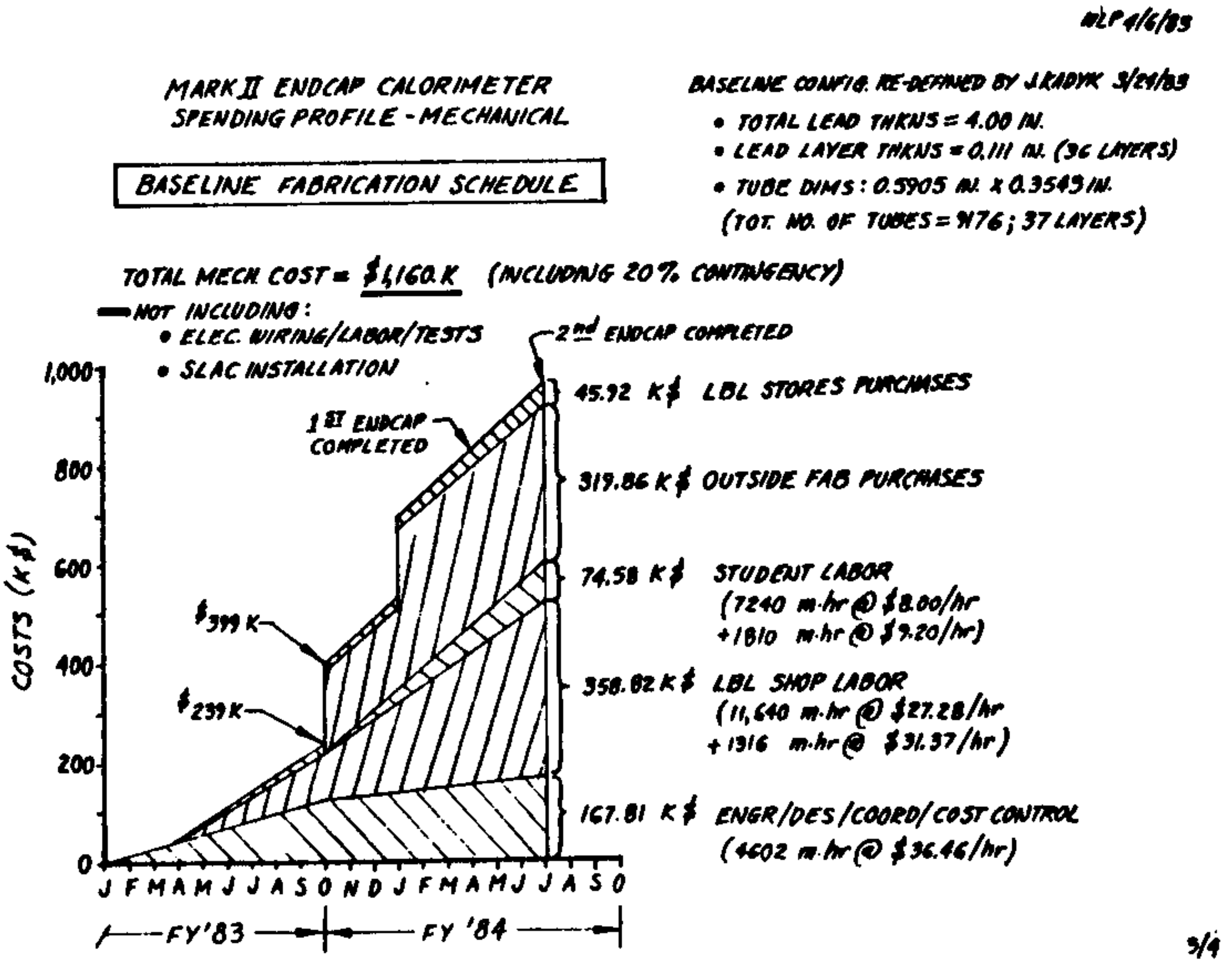

Figure 3.15 Spending profile of mechanical fabrication for installation of both endcap calorimeter modules in summer 1984.

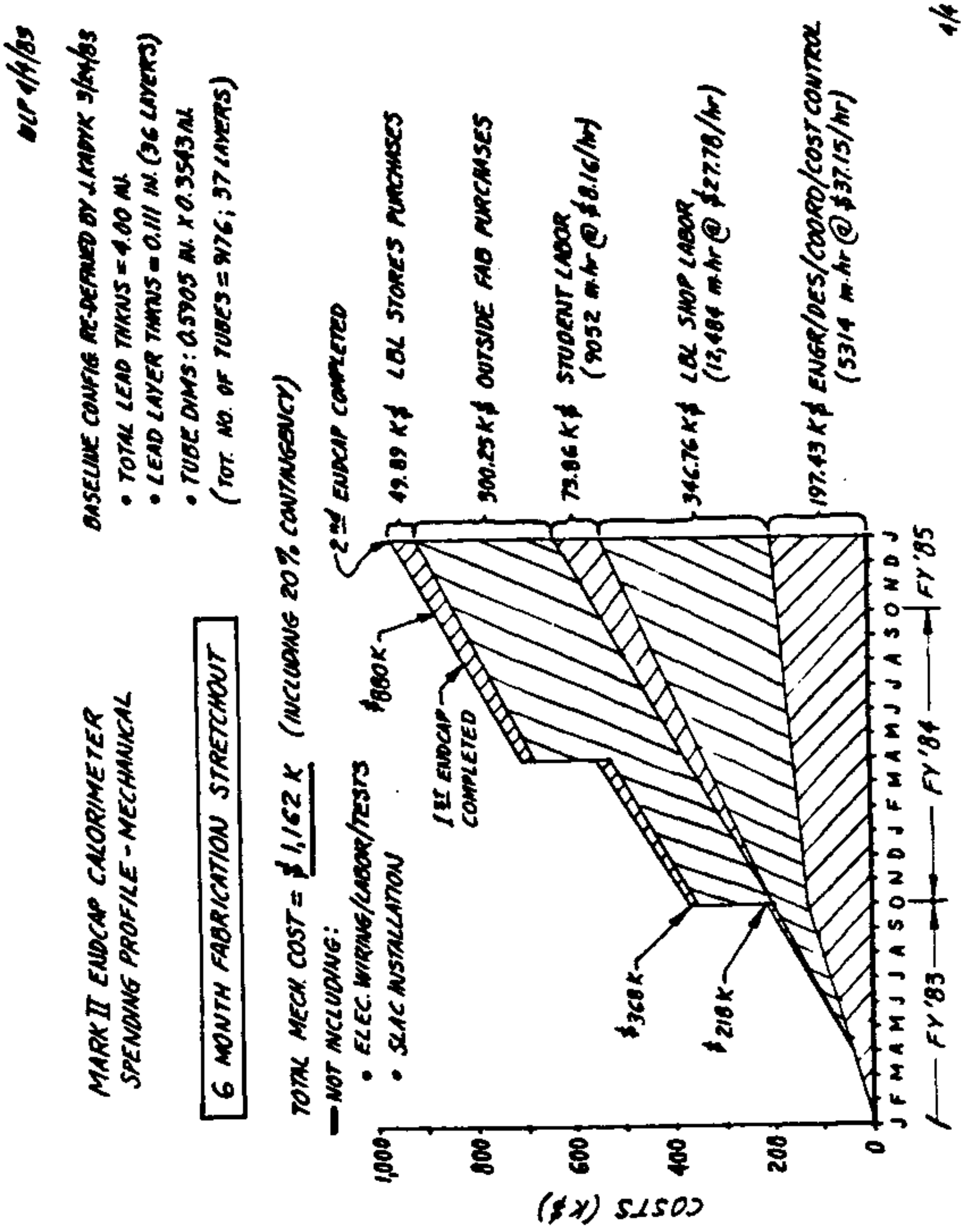

Figure 3.16 Spending profile of mechanical fabrication for installation of one endcap module in summer 1984 and the other in winter 1984-85.

These cost estimates apply to the construction of the ECC and the associated electronics modules, but do <u>not</u> include certain other costs which are related to the ECC construction and operation. Such items that have been identified whose costs must be added to the above estimates are: 1) the endcap door retraction system, 2) the door modification (keyway fill-in), and 3) temperature and pressure regulation and monitoring system.

3.4 Time of Flight Counter System

The Time of Flight counter system serves several purposes. It provides identification of the low momentum particles and is complementary to the dE/dx system for both e/π and π/K separation. It enables us to search for new, heavy stable particles which may be produced at SLC. It is used as a component of the fast trigger and finally it is useful in the rejection of the cosmic ray events.

At present, the Mark II TOF system consists of 48 counters of 1" thick scintillator placed at the radius of 152 cm (see Fig. 1.1). Each counter has acrylic light guides and photomultipliers at both ends. This system has achieved 270 picosecond timing resolution at SPEAR and 350 psec at PEP allowing for the π/K separation of up to ~ 900 MeV/c at the 2σ level.

The major drawback of the present system lies in its crude segmentation. In the multihadron events at PEP about 30% of the struck TOF counters are hit by two or more charged particles. A simple recovery algorithm assigns the nearest phototube to the track. This procedure results in correct assignment for about 50% of the double hits at PEP. Monte Carlo simulation of the multihit and recovery rates agree with the measured data. Such simulation for the c.m. energy of 89 GeV at the SLC indicates [1.1] that over 50% of struck counters with the present geometry will have multiple hits. The recovery rate will also decrease because of the increased average momentum of tracks.

Therefore, we propose to modify the existing TOF system by increasing its segmentation by a factor of two. The upgraded system is being engineered and built at Caltech. The modification will require no change in the end steel of the magnet as the light guides can be brought through the existing holes in the steel (see Fig. 3.17). The Monte Carlo simulation

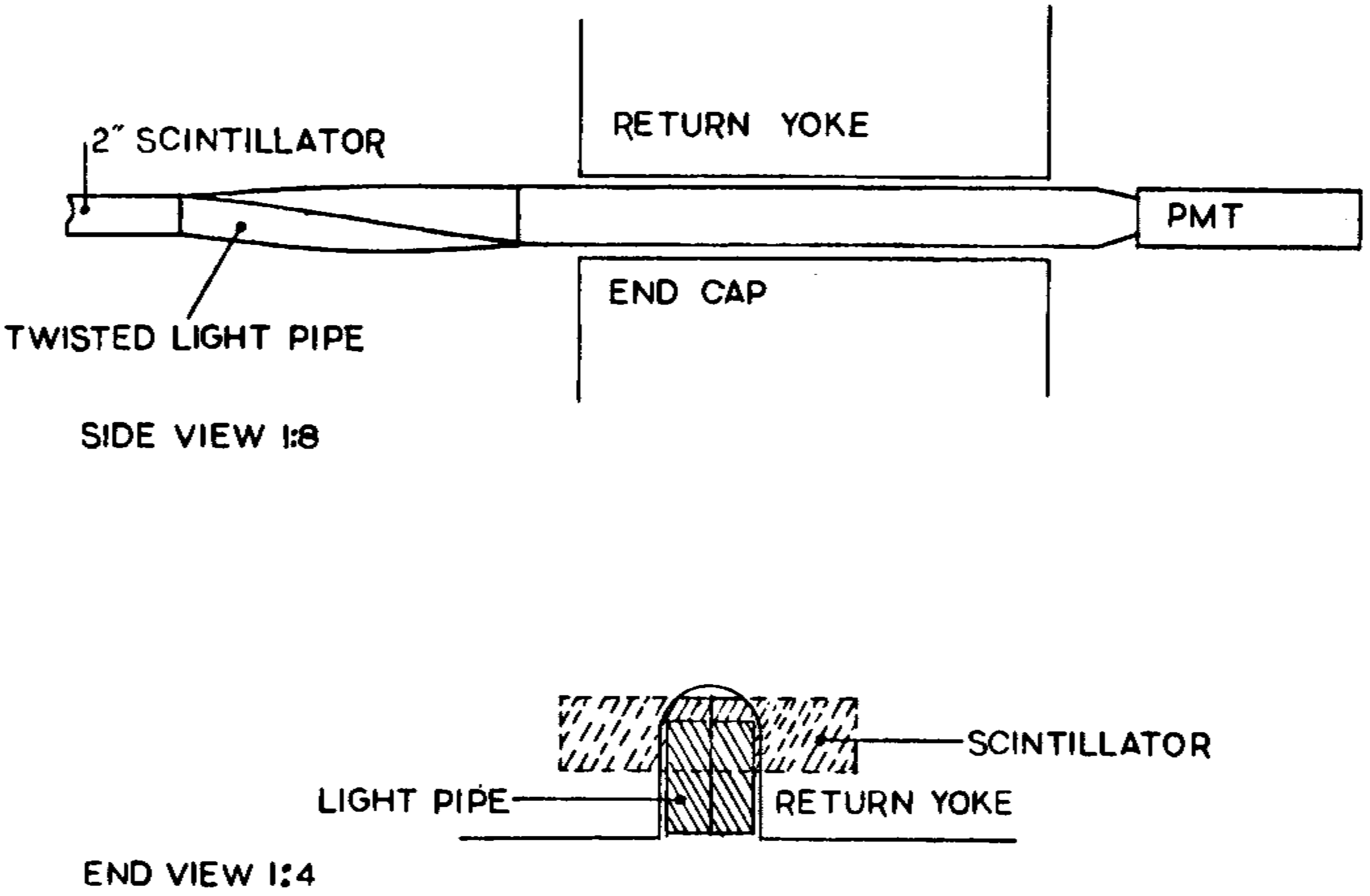

Figure 3.17 Time of flight layout.

described in [1.1] shows that with 96 counters at the radius of 152 cm, the fraction of unrecovered multiple hits will be at the 10-15% level at SLC, i.e., similar to present one at PEP. Most of these unrecovered hits are due to the high momentum particles at the core of the jet for which the time of flight measurement is not applicable.

Fig. 3.16 shows the detection and identification efficiency of the kaon spectrum as a function of momentum for various segmentation and time resolutions of the counter system.

At the same time we propose to improve the timing resolution of the counters. This will be done by increasing the thickness of the scintillator from 1" to 2", redesigning the light guides to maximize the amount of prompt light that is transmitted to the photomultiplier tubes and, if necessary, replace the phototubes with a type which has better timing resolution. The goal of a 150 picoseconds timing resolution may be difficult to achieve due to constraints made by the end steel on the light guides. The slightly worse resolution of 200 picoseconds will increase the range of the π/K separation to about 1.1 GeV/c. At this time it is not known whether changing the phototubes from the present Amperex XP2230 to the faster XP2020 models will be necessary and tests are underway to resolve this question.

The combined dE/dx and TOF particle separation is shown in Fig. 3.4.

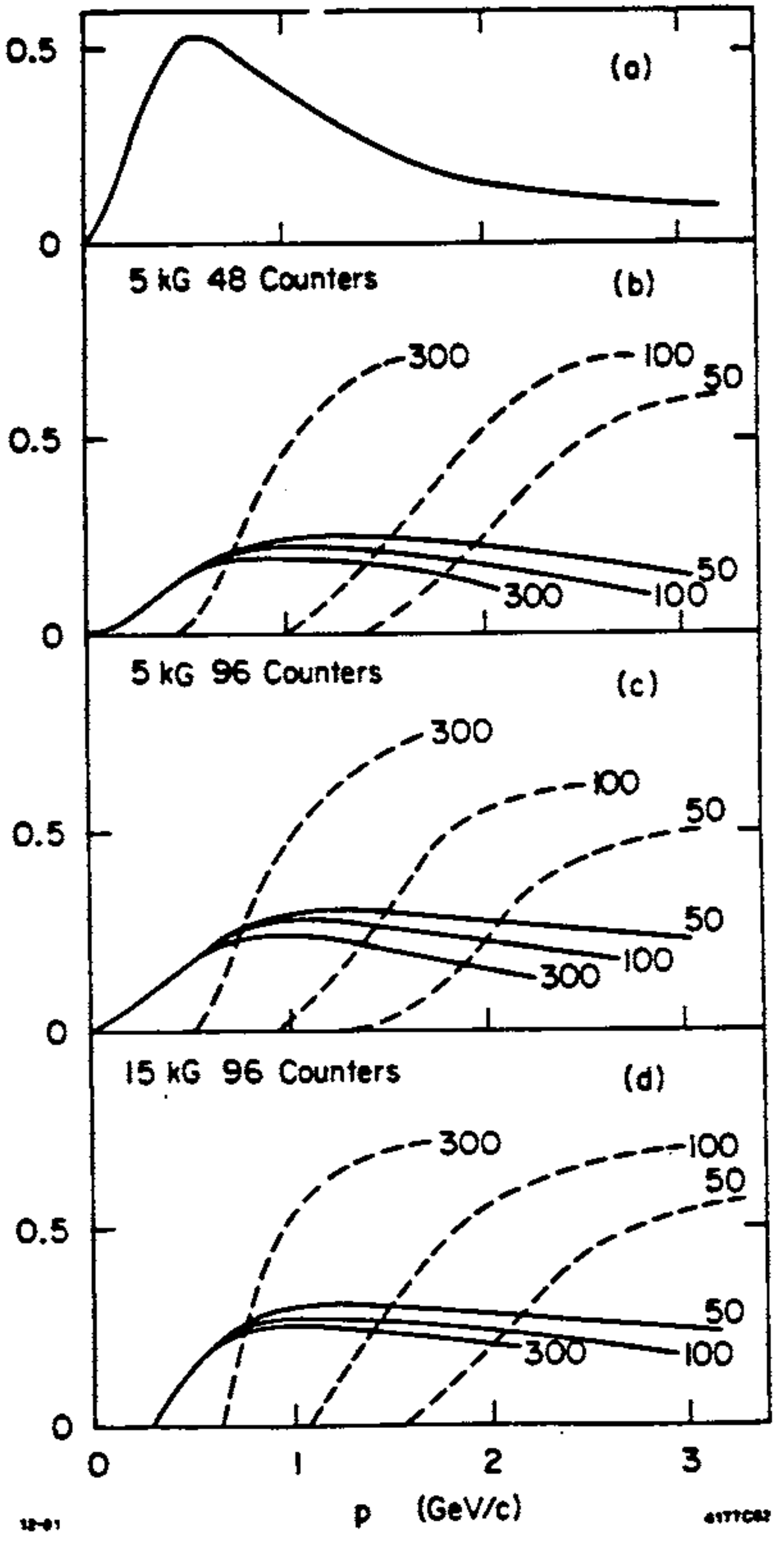

Figure 3.18 a) Produced kaon momentum spectrum. Single-hit efficiency (solid curves) and contamination (dashed curves for b) 48 counters, 5 kG; c) 96 counters, 5 kG; 96 counters, 15 kG. Numbers adjacent to curves give σ_t in picoseconds.

Cost Estimate

The cost estimate is based on 96 scintillators; 5 cm thick, 10 cm wide, and 300 cm long. The material is ND170 from National Diagnostics (PILOT F equivalent). The light pipes will be made from uvt acrylic.

Estimate 1. With XP2230 Phototubes

1.	Scintillator (ND170)	$ 103.0K
2.	Acrylic for light pipes and other components	29.5K
3.	Electronics (110 chs)	82 5K
4.	Engineering and labor	91.0K
5.	Light flasher system	30.0K
	TOTAL	$336 0K

Estimate 2. With XP2020 Phototubes

Item 3 in Estimate 1 was based on a figure of $750 per channel for the electronics. This per channel cost assumes the tubes will be $200 each, which is the cost of the XP2230s. The XP2020 is $700 each so that the per channel cost becomes $1250. This, coupled with the necessity to upgrade all of the channels brings the electronics total to:

$$(\$1250) \times (220ch) = \$275.0K$$

and the system total becomes $490.5K

At this time we are procuring samples to determine what scintillator-light pipe-phototube system will produce the timing precision that is desired. We are using the Monte Carlo program to narrow down our choices, Full scale prototypes of the most likely options will be tested to determine the final design. Due to long delivery times, the design must be finished by

June 1983. We want to place the orders for the major components as soon as the decisions are made. During this same period we will begin our tooling up procedure so that the assembly line will be ready when the materials arrive.

It is our intention to begin mass production in summer of 1983, as the necessary manpower can be made available at that time.

3.5 Muon System

The present Mark II muon system (see Fig. 1.1) is a good match to the SLC physics requirements and there are no plans to upgrade it for the initial running at SLC. It covers 55% of the solid angle and comprises four position measurements with proportional tubes. Each measurement follows 9-12" of steel. The threshold momenta for the four layers (at normal incidence) are 0.7, 0.95, 1.4 and 1.8 GeV/c, respectively. The muon system is confined to the central (barrel) region of the detector but is uniform in its coverage and thickness over that region. There are position measurements in both ϑ and φ coordinates.The wire spacing in the proportional tubes is matched to the multiple scattering and is 2.5 cm. The proportional tubes are triangular in cross-section which has the advantage that a track crossing the proportional tubes has a ~ 65% probability of firing two wires. In this case the left-right ambiguity is resolved, thereby improving the spatial resolution which is important for isolating muons buried in hadron jets. The misidentification probabilities, punch-through plus decay, for hadrons are shown in Fig. 3.19 These curves result from simulations which we have checked using data from the J/ψ for momenta up to 1.5 GeV/c. From 1-50 GeV/c (from extrapolation of Fig. 3.19) the total hadron misidentification rate is always $\leq 2\%$.

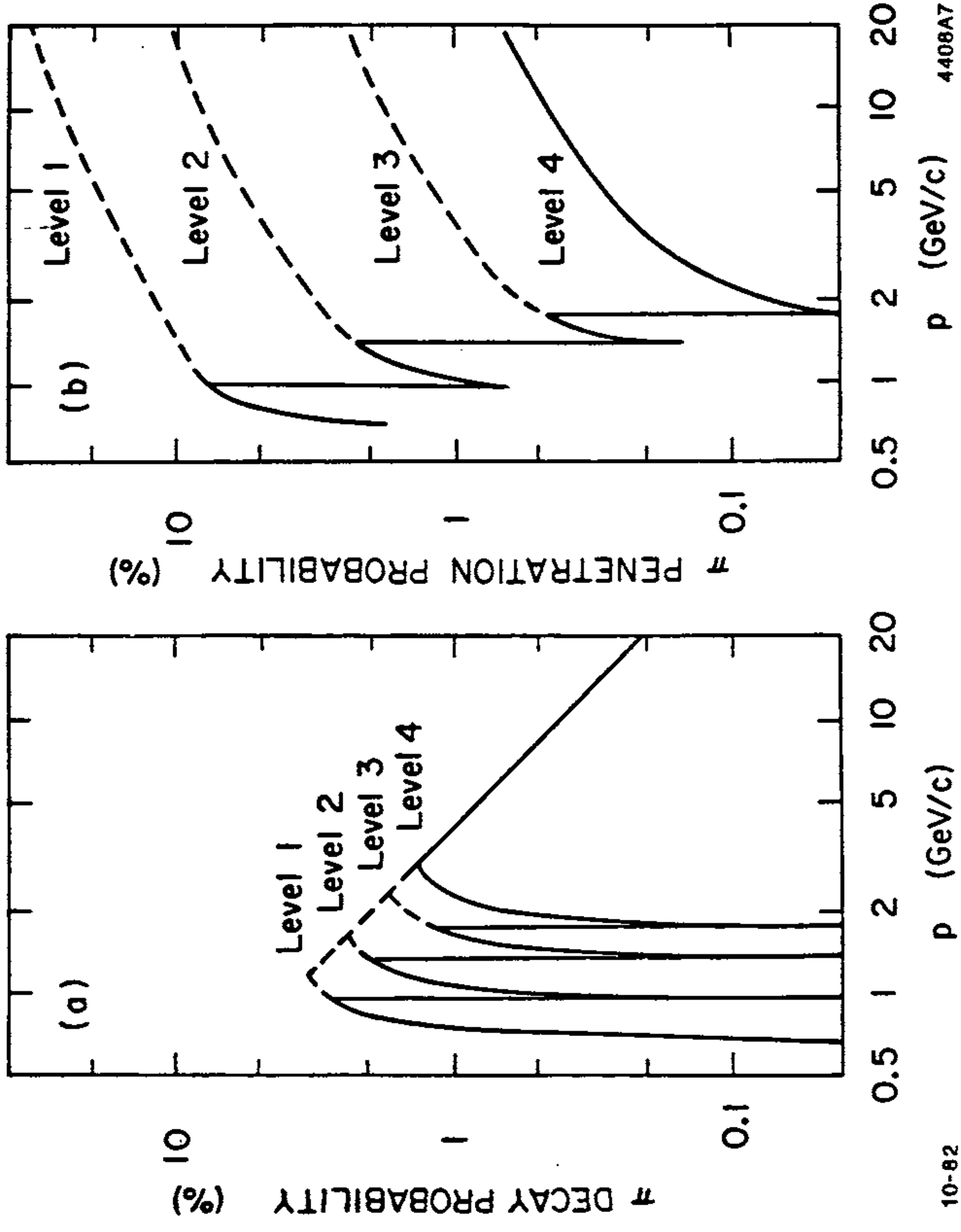

Figure 3.19 Misidentification probability of the muon system as function of momentum a) due to π decays; b) due to pion punch-through.

3.6 Precision Vertex Detection

The unique characteristics of the SLC provide unusual and exciting opportunities for flavor tagging by identification of secondary weak decay vertices of bottom and charmed hadrons and for highly improved precision in lifetime measurements of these particles and of the tau leptons This capability arises from the small e^+e^- interaction volume, the short stay-clear radius near the interaction point, and the pulsed duty cycle of the collider. We propose that a vertex detector should be available at SLC turn-on and be able to take data once running conditions permit

The required performance can be roughly summarized by the following numbers [1.1]:

1) Impact parameter error in track extrapolation to the interaction point of less than about $c\tau/4$ (the factor 4 is to provide an adequate number of standard deviations of separation from the bulk of tracks originating at the e^+e^- vertex).

2) Track overlap resolution of 100 μm for a two-dimensional device (CCD), and 50 μm for a one-dimensional device (silicon strip detector or drift chamber) per centimeter of radial distance from the beam-beam interaction point.

Both pressurized drift chambers and solid state devices could meet these ends, and we are studying all possibilities. Since this device will be installed in the Mark II in late 1986, we have time to decide between various options.

I. Pressurized Drift Chamber for Secondary Vertex Detection

We have initiated development work on a pressurized drift chamber vertex detector suitable for first-round experimentation at the SLC. Such a chamber could be built with existing technology and would survive very high backgrounds. Drift chamber technology is advancing rapidly and existing chambers have achieved spatial and track-pair resolutions approaching those required of an SLC vertex detector. Drift chambers can be operated in very hot environments and, if properly designed, can survive even catastrophic beam loss. In addition, the very low mass and low Z of the detecting medium insures that the device is transparent to most synchrotron radiation.

A vertex detector employing a precision drift chamber was installed in the Mark II at PEP a year ago. We have gained valuable experience with both the technique and the rigors of operation close to the e^+e^- beam line. This program has already borne fruits in the form of lifetime measurements of the τ and the D°.

We presently visualize a pressurized mini-jet chamber with inner and outer radii of 5 and 15 cm, respectively and total length 50 cm. With 20 layers and 30 μm resolution per layer, an impact parameter precision of 20 μm would be achieved.

II. Solid State Devices for Secondary Vertex Detection

Several members of our collaboration are developing solid state devices as vertex detectors. Although these techniques are not tried-and-tested as yet, their potential spatial and track-pair resolution make them attractive. There is time to develop and test these ideas before funds must be committed to a particular design.

A. Silicon Microstrip Detector

Silicon microstrip detectors with position precision of 5 μm, double track resolution of 30-50 μm and impact parameter error of about 15 μm are under development for SLC application. A preliminary design has about 30,000 20 μm strips arranged in three concentric layers at radii between 1.5 and 4 cms. Readout will be done with integrated circuit amplifiers wire-bonded to each end of the detector, and multiplexed (128 strips per line) to a balanced output. The amplifier-multiplexer chip is being designed at the Integrated Circuits Laboratory on the Stanford Campus and will use standard 5 μm NMOS technology. Silicon detectors will survive levels up to about 10^{13} neutrons or minimum ionizing particles per cm^2 and should therefore survive any reasonable background expectations.

B. CCD Arrays

Typical pixel sizes of solid state charge-coupled optical imagers are of order of 15 μm. Readout noise levels of 20 electrons at liquid nitrogen temperatures and 150 electrons at room temperature have been achieved. These are to be compared with a minimum ionizing signal of several thousand electrons. Groups at Rutherford and LBL have already demonstrated the feasibility of detecting minimum ionizing charged particles. We are now evaluating CCD chips from several manufacturers and expect to develop a preliminary detector design by fall 1983.

A three-layer detector will require about 300 one cm^2 chips. As the cost of the CCDs drops we expect that the major expense of the system will be dominated by the readout electronics. Under these circumstances, it will be desirable to install at least a two-layer detector as soon as possible consistent with the access requirements of the SLC machine diagnostics. The unique capability of CCDs to determine three-dimensional space points to very high precision is not easily exploited at any other high energy facility.

It is difficult to estimate the actual cost of the vertex detector until a decision of the type has been made. This decision will be made by 1985 and we presently estimate the cost at $500K.

3.7 Small-Angle Detector

Two important measurements require detector coverage at angles smaller than 20°. One is the determination of the Bhabha cross section. The other is a measurement of $e^+e^- \to \gamma\nu\bar{\nu}$ for which QED backgrounds are large without coverage of the small-angle region.

We give a brief description of the preliminary design of the detector for two different geometries. One assumes a free space available for instrumentation along the beams of ± 50 cm and the other ± 225 cm. The first design allows a minimum detector angle of 50 mr while the second gives 10 mr.

At 93 GeV and with a luminosity of 10^{30} cm^{-2} sec^{-1} the Bhabha rate is 1.2 Hz in the angular interval 10 mr - 20° and 0.047 Hz for 50 mr - 20°. Both rates are more than adequate for measuring integrated luminosities. The rate in the 10 mr detector may also be sufficiently high to be useful for beam tuning.

As shown in Figure 3.20, both detector designs include a relatively simple lead-proportional wire sampling calorimeter for measurements of electromagnetic shower energies. With a total depth of 16 radiation length in 10 sampling layers, the energy resolution at 50 GeV is expected to be ± 5 GeV. The calorimeter is preceded by a drift chamber tracking system consisting of eight layers oriented along $xx'uu'yy'vv'$, where u and v are at ± 45° and the prime indicates a half-cell shift for resolving left-right ambiguities. Precision tracking is essential for accurate measurements of the Bhabha cross section because of the steep decrease in rate with increasing angle.

The total number of drift cells is 1200 for the 50 mr geometry and 1600 for the 10 mr design. The number of ADC channels for the calorimeters is approximately 1000. The total cost for the detectors is estimated to be

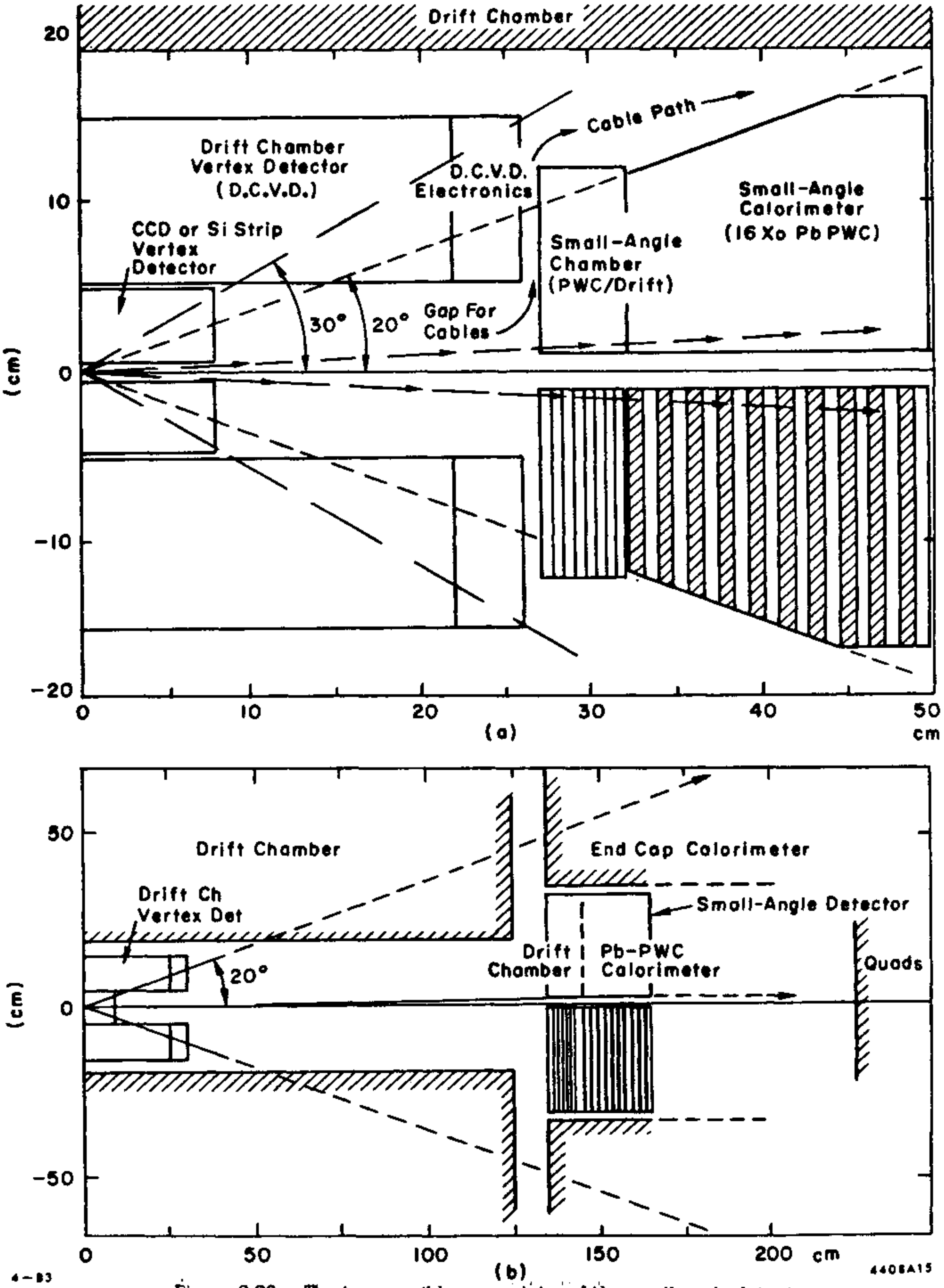

Figure 3.20 The two possible geometries of the small angle detector.

about $200K. The cost could be reduced substantially if presently existing electronics becomes available for this project at SLC. Prototype and tests for the small-angle detector will be completed by the summer of 1984. The choice of the geometry and the final design depends on the design of the final focus and is also expected to be finalized by summer of 1984. Construction of the detector will require an additional 6-12 months.

3.8 The Trigger

The problems posed to an event trigger at the SLC are not different than at existing e^+e^- colliders; indeed, many of the complications are relaxed at the SLC. The trigger must be efficient over a large solid angle for events of various topologies, ranging from events with two charged prongs ($Z^\circ \to l^+l^-$) or a single energetic photon ($Z^\circ \to \gamma\nu\nu$) to high-multiplicity events ($Z^\circ \to$ jets). Efficiency must be maintained while effectively eliminating cosmic-ray and beam-gas backgrounds and backgrounds from beam-gas scattering and synchrotron radiation which produce many scattered hits in the detector. The familiar cosmic-ray and beam-gas backgrounds of PEP are greatly reduced at the SLC due to its much lower (180 Hz) repetition rate.

The Mark II trigger logic provides flexible, programmable selection of trigger conditions from combinations of criteria derived from each detector subsystem. This trigger has operated with high efficiency for physics at SPEAR and at PEP and will operate with no deadtime at the SLC. The trigger has a two-tier structure to provide primary and secondary trigger decisions; however, this structure is not important for operation at the SLC and will not be discussed here.

The principal trigger condition is derived from charged tracks in the central drift chamber. Hits in the drift chamber are fed to dedicated track finding processors which identify tracks defined by $r-\varphi$ roads. The number of tracks found is passed to the master trigger processor. This process takes 32 μsec and can identify tracks from 100 MeV/c to 50 GeV/c. Charged track definition can include a TOF hit and vertex chamber hits in the appropriate $r-\varphi$ road. Selection of drift chamber layers and other detector elements to be included in the definition of charged tracks is partially programmable. A hit in the drift chamber will be defined as a time coincidence of signals on n or more of the six sense wires in a cell, where n and the acceptance window of the coincidence are programmable. The only modification necessary to the existing charged-trigger logic is the addition of the logic to identify a hit within a cell.

In addition to information about charged tracks, the master trigger processor receives information from the electromagnetic calorimeters and the small angle tagging system. The total energy in each calorimeter module, barrel or endcap, is derived by analog summation of signals in the module. Modules with total energy greater than a preselected energy threshold (currently 1 GeV for the barrel modules at PEP) provide status flags to the master trigger processor. The master trigger processor can be programmed to select any set of logical combinations of charged track, neutral energy, and small angle tagging conditions. Some events (e.g. Bhabhas) always satisfy more than one trigger (the two charged track trigger and the two calorimeter energy trigger), thus providing an important cross-check of the trigger efficiency.

3.9 Data Analysis System

The data analysis system for the Mark II at SLC will be similar to the present system used by Mark II. The data will be logged onto tape by a VAX computer. The VAX will also run the experiment, find calibration constants for the various pieces of hardware, and analyze a sample of the events in realtime to check on the performance of the hardware. A link to the central computer system will be used for file transfer between the VAX and the IBM 3081.

The central IBM 3081 computer will be used for the off-line analysis. At present the raw data tapes are copied onto the archived tapes, and the raw tapes are re-cycled. A fast analysis program (PASS1) is done on some of the data in order to determine new constants (e.g., time-distance relationships in the drift chamber) needed for final (PASS2) production analysis. The PASS2 production program analyzes all the raw data, tosses out background events based on a fast filter algorithm, and writes out the processed data for good events onto PASS2 tapes. Summary disk files are then made for a select class of events (hadrons, QED events). The PASS2 tapes and the summary files are then used by the whole collaboration for detailed physics analysis.

Here we estimate the amount of computer time needed for this experiment. We base our estimate by scaling the Mark II values to the Mark II at SLC environment. Currently, Mark II uses about 250 hours of the IBM 3081 computer time per month, of which about 80 hours per month goes for production analysis and the remainder is used by about 35 members of the collaboration for Monte Carlo and data summary analysis. The Mark II at SLC will require considerably more time, since the track multiplicity at SLC is expected to be double that at PEP energies, the new drift chamber has more hits per track (72 versus 23) and the collaboration is larger.

Assuming that the event analysis time scales with the multiplicity and the number of hits per track, then the event analysis time will be larger by a factor of 6 if we use the current tracking program. It may be possible to speed up the tracking in the new chamber by finding track vectors in each cell first, and then link up track vectors into full tracks. An improvement by a factor of two might be possible here. The event trigger rate is unknown at this time. However, since the trigger rates for Mark II at SPEAR and at PEP were similar (about 3 per second), we use the same trigger rate for SLC. Hence, the SLC production time is expected to need about three times that of Mark II at PEP, or about 250 hours per month.

The size of the collaboration has increased considerably from the SLAC (Group C & E) and LBL groups to SLAC (A, BC, C, & E), LBL, Santa Cruz, Caltech and Hawaii. With the larger number of people doing physics analysis, and the more complex Monte Carlo programs at the higher energy, the non-production analysis time will more than double that of Mark II at PEP, to about 350 hours/month.

The total off-line computer time for production and summary analysis is estimated to be 600 hours of the IBM 3081 computer time per month for the collaboration. The on-line VAX 11/780 system currently used at Mark II will sample far fewer events at SLC because of the increased time to analyze an event. If a faster VAX is available at the time the Mark II is installed at SLC, then this would be the choice for the on-line system. 300K$ has been budgeted for such a machine. An alternative plan would involve the use of 3081 emulators attached to the present VAX.

4. Summary of Detector Properties

This section gives the upgraded Mark II Detector at a glance. For all details and explanations, we refer to the appropriate sections and appendices.

4.1 Magnet

Type	conventional solenoid	
field	strength	5k gauss
	inside magnetic volume	32.2 m^3
geometry	inside coil radius	160.4 cm
	outside coil radius	174.0 cm
coil	material	Al
	thickness of conductor	3.15 cm
	No. of turns	217
	current	6890 amps
	power dissipated	1.77 MW
iron	height	5.85 m
	length	5.33 m
	width	3.96 m
	door thickness	stepped from 10.1 cm to 63.5 cm

4.2 Cylindrical Drift Chamber

Type:	drift chamber	
volume		$r_i = 19.4$ cm , $r_o = 150$ cm
		l = 2.3 m
wires	No. of sense wires	5832
	No. of guard wires	3888
	No. of potential wires	8748
	No. of radial sensing layers	72
	stereo angle	~ ±3.5°
	radial wire spacing	8.33 mm
	max drift length	~3.3 cm
	stagger for ambiguity	±380 μm
	resolution	
Performance:		
	$\Delta r\varphi$ (for sagitta)	<200 μm
	double track resolution	4.16 mm
	ionization measurement	
	(72 samples)	6.9%
	momentum measurement	
	(vertex-constraint)	
	$\sigma(p)p^{-2}$: for $\lvert\cos\vartheta\rvert < 0.7$	0.15% GeV^{-1}
	< 0.85	0.45% GeV^{-1}
	< 0.89	0.9% GeV^{-1}
	tracking efficiency	
	$\lvert\cos\vartheta\rvert < 0.89$	100%

4.3 Time-of-Flight System

Type:	Scintillation counters	
geometry	length	300 cm
	thickness	5 cm
	width	10 cm
No. of counters		96
coverage	radius	1.52 cm
	$\lvert\cos\vartheta\rvert$	<0.7
Performance:	time resolution	$\Delta t \lesssim 200$ psec
	3σ particle separation	
	(dE/dx plus TOF)	e/π: $\lvert\vec{p}\rvert \lesssim 7$ GeV/c
		π/K: $\lvert\vec{p}\rvert \lesssim 1.1$ GeV/c

4.4 Electromagnetic Calorimeter

Electromagnetic calorimetry will be provided as shown in the Table below.

Name	$\cos\vartheta$	Thickness (radiation length)	Type	Granularity
LA Barrel	<0.7	14	Liquid Argon Strips	4 cm
EEC Endcap	0.7-0.95	18	Gas Wire	1.5 cm
Small Angle	0.92-0.999	16	Gas Wire	not decided

A. Barrel

Type:	Lead/Liquid Argon sandwich	
geometry		$r_i = 1.8$ m
		$l = 1.8$ m
	solid angle coverage:	$\lvert\cos\vartheta\rvert < 0.7$
		$\Delta\varphi = 2\pi$ (eight octants)
	modular thickness	Pb 2 mm (0.36 X°)
		Ar 3 mm
	total thickness	14 radiation length
	total weight	8 t/module
Segmentation:	radial	7 layers
	tangential	3.7 cm
	number of layers	ϑ : 2
		φ : 4
		$U(45^{\circ})$: 1
Performance:	energy resolution at 90°	
		E < 15 GeV, $\frac{\sigma}{\sqrt{E}} = 12\%$
		E $\lesssim$ 50 GeV, $\frac{\sigma}{\sqrt{E}} \leq 15\%$
	angular resolution	
		$\sigma_{\vartheta} \approx \sigma_{\varphi} \approx 3.5$ mrad
	π/e misidentification	
	(isolated tracks)	< 1%

B. Endcaps

Type:	lead/drift tube sandwich	
Geometry:		$r_i = 34.3$ cm, $r_o = 147.3$ cm
	thickness	66 cm
	solid angle coverage	$0.71 \lesssim \lvert\cos\vartheta\rvert \lesssim 0.95$
	modular thickness:	Pb 2.8 mm $(0.5\ X^{\circ})$
	drift tubes: Al extrusions	0.9×1.5 cm^2
	total thickness:	18 radiation length
Segmentation:	No. of layers	36
	No. of drift tubes	$\sim 2 \times 9{,}000$
	No. of readout channels	$\sim 2 \times 2{,}500$
	coordinates	x,y,u,v
Performance:	energy resolution	$\frac{\sigma}{\sqrt{E}} \approx 17\%$
	angular resolution	$\sigma_\vartheta \approx \sigma_\varphi \approx 3$ mrad
	π/e misidentification (isolated tracks)	<0.5%

C. Small Angle Monitor

Purpose:	luminosity monitoring extension of calorimetry to very small angles
Type:	drift chamber tracker Pb/drift chamber calorimeter

Detailed design is not completed.

4.5 Muon System

Type:	Steel/proportional tube sandwich	
Geometry:	No. of layers	4
	total thickness	1.05 m
	solid-angle coverage	55% of 4π
	tube geometry	overlapped triangular
Wires:	spacing	2.5 cm
	measured coordinates	ϑ, φ
	ambiguity resolution	~65%
Threshold momenta at $\vartheta = 90°$:		
	layer 1	0.7 GeV/c
	layer 2	0.95 GeV/c
	layer 3	1.4 GeV/c
	layer 4	1.8 GeV/c
Hadron/muon misidentification		<1%

4.6 Precision Vertex Detector

Purpose:	acquisition of precise tracking close to vertex (impact parameter precision $\lesssim 20\ \mu m$)
Type:	small drift chambers (pressurized) silicon microstrip detector CCD array

Development and prototyping of these techniques is presently underway. Choice of technique and detailed design are to be based on this work.

5. Machine Interactions and Backgrounds at SLC

The composition of the SLC arcs and final focus system is not yet finalized. For this reason, it is difficult to present a thorough discussion of background problems at the SLC. The Mark II group meets regularly with the SLC final focus group so that potential conflicts between detector hardware and beamline elements are being avoided. At the present time, there exist no incompatibilities between the detector and the configurations envisaged for the final focus. We have a conceptual design for the support of the SLC beamline, the Mark II small angle monitor (SAM) and vertex detector and we foresee no problems in this area. As discussed in Section 3.7, we have two possible locations for SAM depending on the choice of final focus quadrupole positions. The Mark II does have a subgroup whose function is to study carefully the masking and shielding required at the SLC to keep the backgrounds to an acceptable level. Considerable work is involved in setting up the software to study these problems, but the effort has begun. Neutron backgrounds from the beam dump areas are also being studied. We present below discussions based on previous studies which will give an indication of the type of problems encountered.

A considerable amount of work has been done in studying various types of particle backgrounds which can occur during experiments at the SLC and some estimates have been made for the magnitudes of the following processes: 1) Synchrotron radiation due to beam particles passing through the main bending magnet, or through the "soft" bending magnets; 2) synchrotron radiation emitted when incident beam particles are focussed by the final focus quadrupoles, or when the disrupted beam passes through these quadrupoles after the beams have collided; 3) beam-gas scattering, which can occur on residual gas nuclei anywhere in the vacuum pipe, and is manifested as a beam particle of degraded energy in the case of beam-gas bremsstrahlung, or as a particle with full energy and large betatron amplitude in the case of coulomb scattering; 4) "beamstrahlung", which results from individual $e^\pm$ particles radiating in the magnetic field produced by the opposing bunch; 5) neutron production, resulting mainly from excitation of giant resonances in the nuclei of the absorber material struck by X-rays. The threshold for this is about 10 MeV γ-ray energy, and it occurs at the positions where either the synchrotron radiation from the main bend magnet, or the beamstrahlung, is finally stopped by absorber.

These processes can better be visualized by referring to the sketch shown in Fig. 5.1 of the beam line (a recent modification of the "miniquad" configuration), and to the sketch of the detector and beam magnets given in Fig. 1.1a. Both the beam optics and mask design are based on those given in SLAC-247 with certain modifications, and most of the background estimates are taken from these reports.

The synchrotron radiation and degraded or disrupted beam background studies presently estimate the levels of these backgrounds to be comparable with those of current PEP running. The actual experience at PEP by the Mark II detector is that no SR background is seen inside the detector, and a low-energy shower background resulting from degraded beam is observed with about 1% occupancy. There was initially some SR background coming from the main dipole magnets in the PEP tunnel, but this was a relatively easy problem to eliminate by external shielding. Neutron production by energetic γ-rays will be a new process not experienced at PEP, but the present estimates do not indicate this to be a serious background problem. These estimates are discussed in Appendix III. In

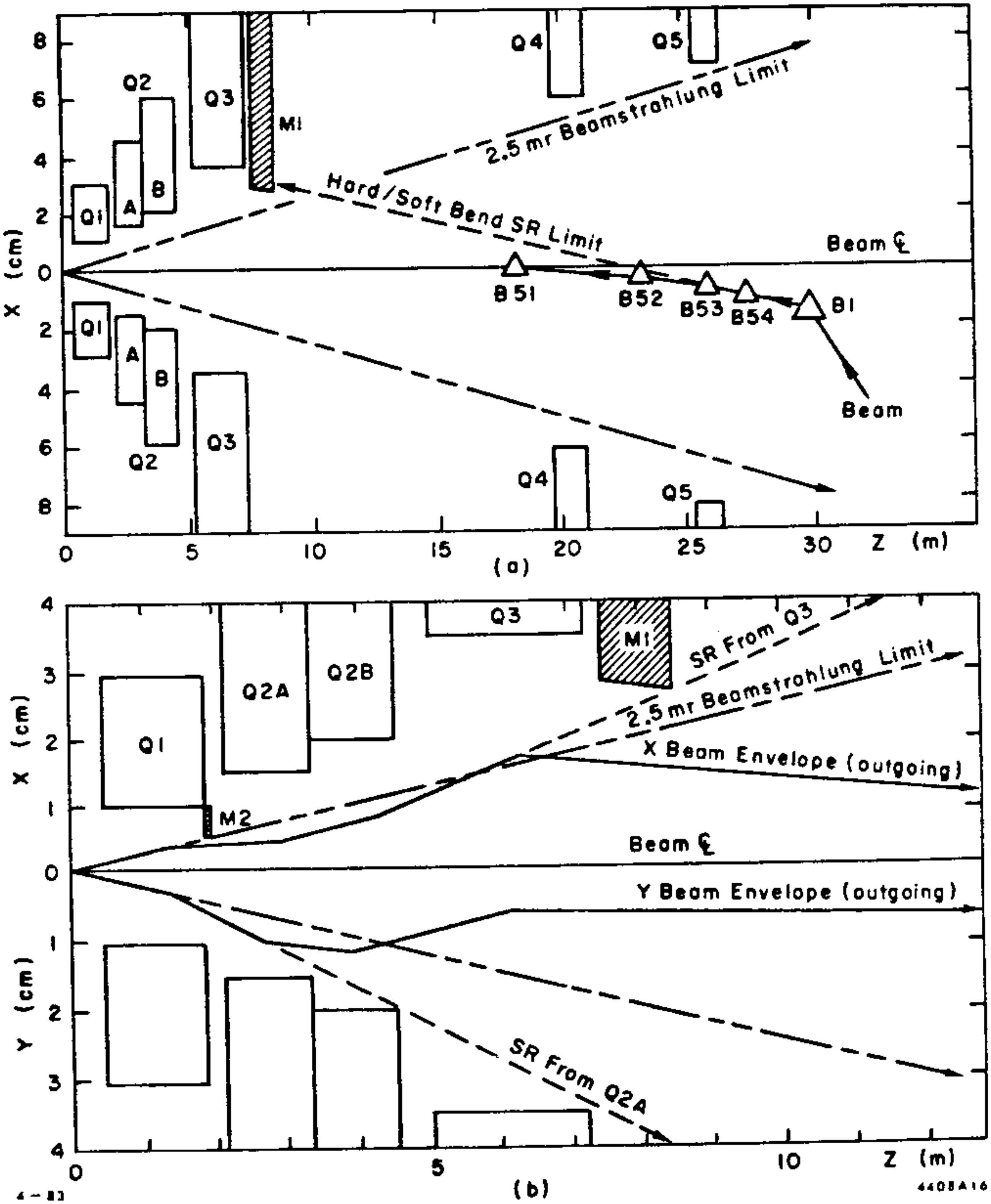

Figure 5.1 Sketch of the beam-line

summary, all of the background processes studied appear to be manageable if sufficient care is taken in the shielding.

Detector Hardening Against Unexpectedly Large Backgrounds

As studies continue, progress can be expected both in the understanding of background processes and in shielding designs. However, if at SLC turn-on the backgrounds prove to be much more severe than predicted, perhaps because the beams have not yet been tuned optimally, what strategies can be used to minimize the effects of unexpectedly large backgrounds and allow the detector to operate?

We can imagine two levels of detector hardening. At the first level, we suppose the backgrounds are only moderately severe, causing an objectionably high flux of low-energy γ's ($\leq$1 MeV) and/or neutrons. To suppress leakage of the low-energy γ's, some shielding may be added around the quadrupole support tubes in the form of an additional steel tube of 1" to 2" wall thickness. Reduction in the flux of neutrons from $|Z| \sim 20$m may be achieved by placing absorber material between Q4 and M1. (The mask, M1, should already be thick enough to eliminate neutron background from this source.) As has been discussed in the section on triggering, the programmable feature of the Mark II trigger provides the flexibility needed to respond to problems of background by restricting the trigger criteria in an optimal way.

At very high background levels the following possibilities for useful data taking are envisaged. We could reduce the sensitivity of the detector components at small radius where backgrounds are expected to be the most intense. Some of the inner layers of the central drift chamber could be deactivated by lowering the wire voltages. Although measurements of momentum and dE/dx would suffer, it is likely that triggering and tracking could still be accomplished effectively. Independently, or in combination with the above, we could use the neutral trigger which is derived from the energy deposited in the calorimeters. The energy threshold could be adjusted until an acceptable trigger rate was achieved. A ~ 5 GeV threshold would yield a very high trigger efficiency for both hadronic events and di-electrons.

6. Schedule

The journey of the Mark II detector to the SLC has two major phases. In the first phase the detector is upgraded and undergoes a 12-15 month test at PEP. The detector is then transported to the SLC IR and reconstituted so as to be ready for SLC collisions in late 1986. These two phases present different problems and involve different schedules. The achievement of these two objectives is covered in this section.

I. The Upgrade and Subsequent Testing at PEP

The major pacing item in the upgrade schedule is the new central drift chamber. The current schedule shows it ready for the installation phase by May 1984 (see Section 3.2 and Appendix I). Long before this time the new coil and time-of-flight counters will be ready. The TOF counters are then strapped to the outer perimeter of the drift chamber and the drift chamber/TOF assembly will be threaded into the coil. This "central package" will then be transported from the heavy assembly building at SLAC down to the PEP interaction region.

The Mark II will roll off the PEP beam line sometime during the spring of 1984. The exact time will be chosen such that there is sufficient time to dismantle the detector so that the new central package, described above, can be installed. The process of dismantling the detector involves the removal of the present central package (with its drift chamber, coil and TOF counters), the vertex drift chamber and the endcap calorimeters. The removal of the vertex chamber and endcap shower counters is straightforward. However, the present central package is captured by the end steel of the flux return. In order to remove the end steel (this will be done on one end only) the top steel must first be removed. Once the steel has been removed the present central package can be removed. The new central package will be installed and the steel reconstituted. The new endcaps will be mounted on the end doors and the new detector elements will be cabled up. In the new PEP configuration we will no longer use the vertex detector because it is too large to fit into the free space between the beam pipe and the drift chamber. In this space we will install the two cylindrical scintillation counters used prior to the installation of the vertex detector. This will be necessary for the detector trigger--in particular, to limit the cosmic ray tragger rate.

During this installation, we will modify the detector end steel so that the new central package will not be trapped. This modification involves cutting the existing end steel so that a removable annulus will permit enlarging the hole in the end steel to facilitate the removal of the central package.

During the summer 1984 shutdown we will also install an automatic door retraction system. The two end doors will retract on permanent fixtures giving access to the drift chamber, TOF and endcaps. A schematic of a possible door retraction system is shown in Fig. 6.1. We expect that with this system, access to both endcap regions will be available an hour after the beginning of an IR access. Currently the end doors are removed using the crane. If both doors require removal, one has to be "parked" on the IR floor. This is both cumbersome and time consuming.

The PEP beam line will be modified to accommodate the new detector elements and the door retraction system. We envisage building a beam pipe similar to that of the MAC detector which has to contend with the same basic set of issues. We will replace the present beam pipe between $Z = \pm 3\,m$. The new section of the beam pipe will be considerably simpler in design than the present beam pipe. We will not have the large cones which optimized the rate and quality of measurement of luminosity and electron tagging over a large forward solid angle. The luminosity monitor itself will still be used; however, in all likelihood we will use smaller defining counters so as to match better the thin window acceptance of the new beam pipe. The effective Bhabha counting rate for luminosity monitoring will be about one third of what it currently is. We will remove the small angle tagging drift chambers which presently track the electrons before they reach the luminosity shower counters. We have considerable

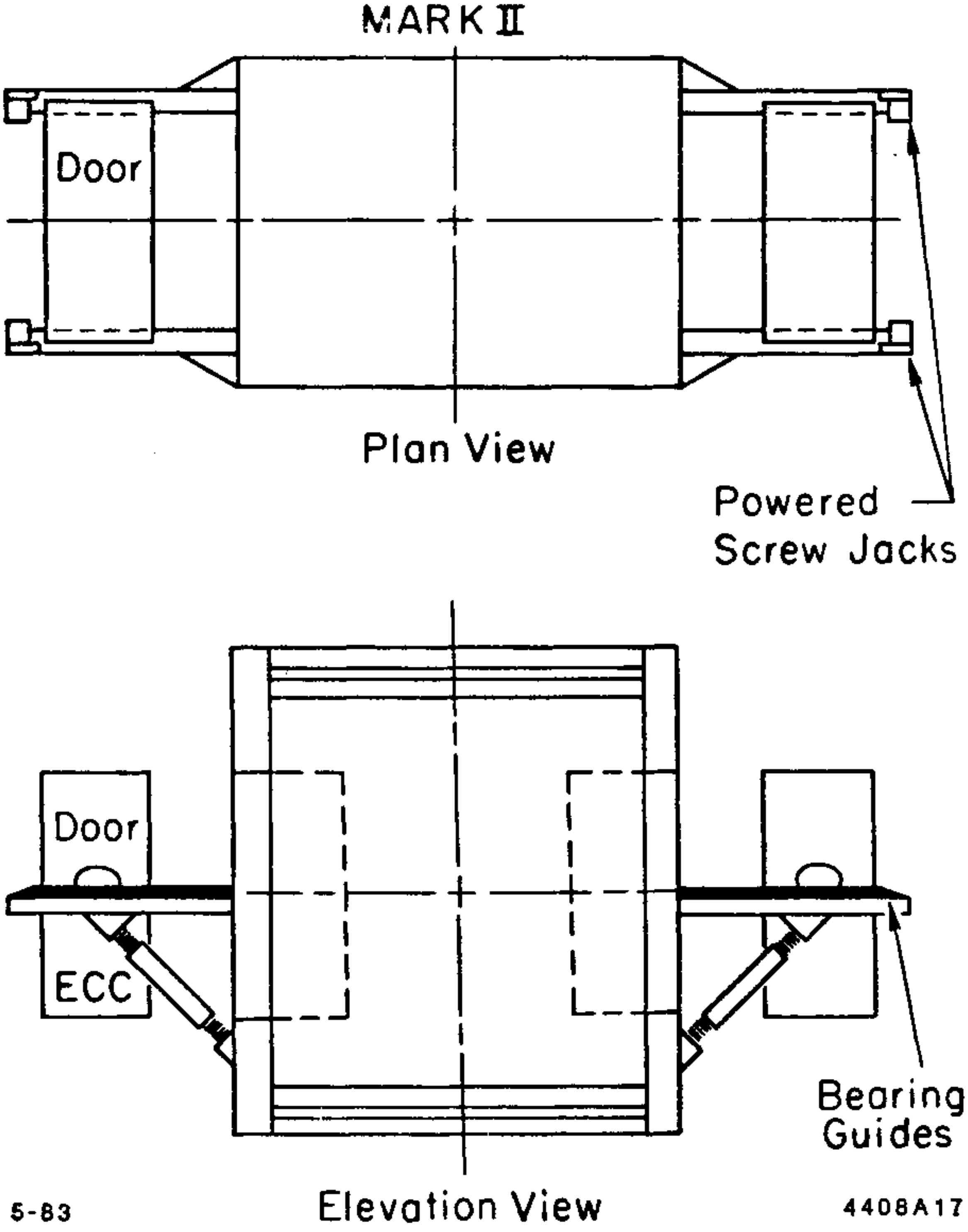

Figure 6.1 Door retraction system

experience with using the wide angle Bhabhas for normalization and the new configuration of the luminosity monitor will not present any experimental difficulties.

The majority of the on-line electronics is housed in a building attached to the Mark II detector called the LEACH. We do not envisage requiring any more floor space for electronics than is available in the LEACH. Approximately six extra racks will be added to the LEACH and by our present reckoning, this is sufficient to house the new electronics. The present schedule for the drift chamber electronics shows the TDC/trigger system ready for the full system by the summer 1984 installation. The TDC modules (see Appendix I) are to be purchased from LeCroy; one third of the total system will be bought and delivered this fiscal year. The schedule for delivery of the total dE/dx electronics is not yet certain; in all likelihood, a major fraction of this electronics will be installed before the end of 1984. The endcap electronics is as yet not designed. Here we envisage using the same digitization electronics as is currently used for the liquid argon modules. It seems reasonable, then, that front end electronics can be designed and fabricated in time for the summer 1984 installation. The flexible Mark II trigger electronics will be used in its present configuration--cards mounted on the rear of the TDCs will provide the necessary summed signals needed for the trigger processors.

As stated earlier, the schedule for the PEP installation is paced by the construction schedule of the drift chamber. If we are able to hold to the present schedule, showing the drift chamber installed in the coil by early June, then we will be ready to take PEP beam by October 1, 1984. If the drift chamber is delayed, we will go back on beam line when we are ready. In the most pessimistic schedule we will return to the PEP beam line during the Christmas shutdown of 1984. The current schedule for the endcaps (see Section 3.3.2) shows them being ready for installation in the summer 1984 shutdown. Their installation is easy and at worst they will be installed during the Christmas 1984 shutdown. To summarize, then, the upgraded Mark II detector will be on the PEP beam line with all its upgraded hardware at the earliest in October 1984 and at the latest in January 1985. The budget impact of this installation is covered in Section 8.

II. The Move to SLC

The present machine schedule shows collisions in the fall of 1986 with the Mark II in its off-line position. The final focus should be understood well enough by the end of 1986 to permit the Mark II to move on beam line and commence data-taking. With this schedule in mind, we envisage going off the PEP beam line during the 1985 Christmas shutdown. The detector will then be broken down in transportable pieces and moved to the SLC IR where it will be reconstituted in the off-line position (see Section 1.2 and Fig. 1.3). Services required to run all systems of the detector will be available in this off-line position. Hence, we foresee being ready for full checkout with cosmic rays beginning no later than September 1986 All items required for the move and reconstitution have been carefully tabulated so that a sound estimate of the associated budget could be presented in Section 6. However, the detailed schedule of this work has not yet been finalized Suffice it to say that we will leave PEP early enough to ensure that we will be ready and checked out when beams first collide at the SLC.

Details of the move are as follows. The Mark II will be taken off the PEP beam line The detector elements will be decabled at the detector end only and the cables will be coiled up and secured to the LEACH. The cryogenic interconnections between the detector and LEACH and the detector and the argon and nitrogen tanks will be removed. The LEACH and detector will then be separated--provision for this already exists--so that they can be moved as separate entities. The muon walls on either side of the detector and on the top and bottom will be taken down and transported to the SLC IR as approximately one hundred 15-ton pieces of steel. The slimmed-down detector will now resemble closely in weight the size of the package which was moved from SPEAR to PEP. Using similar techniques then, the detector and LEACH will be moved to the apron of the SLC IR. The floor of the experimental hall is 17 m below this apron. Several schemes have been proposed for lowering the ~400-ton detector to the pit floor. The Experimental Facilities Division at SLAC, under the guidance of Herb Weidner, has reviewed these methods and have selected a method which they feel is safe and economical. At present we see no obvious objections to this scheme and we are using it as our working decision. The budgeted amount for the lowering is the EFD figure. The LEACH, muon steel, etc., are all lowered to the pit floor using the 25-ton capacity crane. At this point the muon system will be erected and the LEACH will be mated to the detector.

The beam line at the SLC will be one and a half meters higher than at PEP. To accommodate this, an undercarriage will be fabricated for the detector and the LEACH. This undercarriage will provide the means for moving the Mark II on and off beam line. All auxiliary equipment such as gas, cryogenic and magnet power supplies, the VAX, etc., will be relocated to the SLC IR and the detector will be restored to its PEP operating configuration. Full operation both on and off the beam line will be provided for.

The only PEP untested hardware which will be installed at the SLC will be the vertex detector and the luminosity monitor. These will be installed at the SLC IR. The vertex detector will be checked out along with the rest of the detector using cosmic rays. The luminosity monitor will have to await beams for full checkout.

At present only a conceptual design of the beam line components in the IR and their supports exist. We envisage a detachable spool piece, roughly ±2.5 m long, traversing the beam crossing point. Support for this spool piece plus the vertex detector and luminosity monitor will come from two vertical pillars at approximately ± 5 m relative to the interaction point.

We are maintaining close contact with the SLC IR and final focus groups so that design decisions are not being made by any group which will cause foreseeable problems.

The budget for the relocation of the Mark II to the SLC IR is discussed in Section 8.

7. The Collaboration and Responsibilities

The collaboration formed to upgrade the Mark II for use as the first detector at SLC includes much of the original SLAC and LBL groups involved with the Mark II detector at SPEAR and PEP. In addition, the collaboration has been strengthened by the addition of groups from Caltech, U.C. Santa Cruz, University of Hawaii, University of Colorado, Johns Hopkins University, University of Michigan, and added participation from SLAC.

The overall collaboration formed for the upgrade represents a strong group capable of effectively rebuilding the detector for use at SLC. We expect the collaboration to approximately double in size, however, most of this growth is expected to be in the form of expansions of the present groups (mostly from the addition of post-doctoral staff and students). We do plan to consider modest expansion of the collaboration after the second round detector decisions for SLC.

Below we list the present collaboration, including physicists and engineers (E):

LBL

G. Abrams, G. Gidal, G. Goldhaber, J. Haggerty, D. Herrup, J. Kadyk, P. Sheldon, G. Trilling, K. Lee (E), M. Nakamura (E)

Caltech

B. Barish, G. Fox, T. Gottschalk, M. Nelson, C. Peck, R. Stroynowski, R. Cooper (E)

U. C. Santa Cruz

D. Dorfan, C. Heusch, W. Rowe, H. Sadrozinski, T. Schalk, A. Seiden, A. Weinstein, W. Nilsson (E)

University of Hawaii

R. Cence, F. Harris, S. Parker, D. Yount

University of Colorado

E. Fernandez, W. Ford, J. Smith

Johns Hopkins University

B. Barnett, J. Matthews

University of Michigan

C. Akerlof, J. Chapman, D. Meyer, D. Nitz, R. Thun, A. Seidl

SLAC - Group A

W. B. Atwood, H. DeStaebler, R. Pitthan, L. Rochester

SLAC - Group C

A. Boyarski, F. Bulos, J. Dorfan, R. Hollebeek, A. Lankford, R. R. Larson, V. Luth

SLAC - Group E

P. Burchat, D. Burke, G. Feldman, G. Hanson, K. Hayes, W. Innes, J. Jaros, M. Perl

SLAC - BC

J. Ballam, T. Glanzman, C. Field, K. Moffeit

SLAC Engineers

B. Denton (Coordinating Engineer), D. Horelick (Electronics Project Engineer), C. Hoard, D. Hutchinson, D. Porat

The present spokesmen for the group are J. Dorfan, G. Feldman, and G. Trilling. Although much of the responsibility crosses institutional lines there are some specific responsibilities for the upgrade:

Drift Chamber

The Mechanical Design and construction is being coordinated by SLAC Group E (G. Hanson), while the front end electronics are being developed by U. C. Santa Cruz with engineering help from SLAC.

End Cap Calorimeter

The design and construction of this calorimeter is the responsibility of the LBL Group (J. Kadyk). The endcap electronics are undecided at this time.

TOF System

The new time-of-flight system is being designed and constructed at Caltech (B. Barish and R. Stroynowski)

Small Angle Monitor

This small angle detector is the responsibility of University of Michigan (R. Thun)

Precision Vertex Detection

At present, there is a parallel effort to determine the best approach to vertex detection. We expect to make a decision in about two years. These efforts include (i) Pressurized drift chamber (SLAC Group E - J. Jaros), (ii) Silicon microstrip detection (University of Hawaii - S. Parker), and (iii) CCD arrays (University of Michigan - C. Akerlof and SLAC - B. Hollebeek).

In addition, work on other aspects of the upgrade including prototype work, electronics and triggering, data acquisition, data analysis systems, etc. are being worked on by various members of the group.

The short term goals are to build the new drift chamber, endcap calorimeters, and TOF system and install into the Mark II during 1984 for testing at PEP. This is a difficult challenge and will require availability of substantial funds during FY 83 and 84 (see budget - Section 8) and some strengthening of the groups responsible for the PEP upgrade (new postdocs, etc.).

8. Budget

The budget for the Mark II upgrade and move to SLC is considerably better understood now than it was at the time when the Letter of Intent was submitted. A large fraction of the hardware is in the procurement stage and detailed engineering estimates have been made. Fairly detailed schedules for the summer 1984 installation and the move to SLC exist and their associated budgets represent an honest attempt to include all the costs. The areas of the budget which are most uncertain are the cost of building the dE/dx electronics, the yet unspecified vertex chamber, and the endcap electronics.

We have not included in our budgets the cost of Engineering and Fabrication for the support and alignment of any of the components of the final focus. We have, however, included the cost of support stands and walkways on which the beamline will presumably be mounted.

The budget is shown in Table 8.1, broken down by project and fiscal year. The exact apportionment of the 1985 and 1986 budgets is unclear because the choice of vertex detector has not yet been finalized and the SAM schedule is not yet in hand. The $1621K of drift chamber electronics money deferred to FY85 is for the purchase of most $(\sim\frac{5}{6})$ of the dE/dx electronics. Only monies needed for the dE/dx for engineering, procurement of the $\frac{1}{6}$'th of the cables and one crate full of electronics are included in FY84.

We fully expect that some items have been overlooked in our budget estimate. Based on an accessment of each project, we estimate that a contingency of 1.1M$ is appropriate.

TABLE 8.1

Mark II/SLC Budget (K$)

ALL COSTS ARE IN FY83 DOLLARS.

ALL LABOR COSTS INCLUDE A 30% OVERHEAD CHARGE.

	FY83	FY84	FY85	FY86	TOTAL
DRIFT CHAMBER					
Mechanical	730	325			1055
Electronics	480	1439	1621		3540
ENDCAPS					
Mechanical	200	962			1162
Electronics	50	150	200		400
TOF	200	136			336
INSTALLATION (summer 84)	55	587			642
NEW COMPUTER (VAX 790?)			300		300
VERTEX DETECTOR		25	375	100	500
SMALL ANGLE MONITOR			100	100	200
MOVE TO SLC			350	1461	1811
	1715	3624	2946	1661	9946

WE FULLY EXPECT THAT ITEMS HAVE BEEN OVERLOOKED IN THESE BUDGETS.

WE ESTIMATE A CONTINGENCY OF 1,100 K$ IS APPROPRIATE.

APPENDIX I

DETAILS OF DRIFT CHAMBER DESIGN

A. Mechanical Design

1. Cell Design

The design of the new drift chamber is based on a multi-sense-wire cell, shown in Fig. 3.1. This cell contains six sense wires staggered ± 380 μm from the cell axis to provide local left-right ambiguity resolution. The sense wires are 30 μm diameter gold-plated tungsten, tensioned to 113 gm to give 91 μm gravitational sag in the middle of the 2.45 m length. The spacing between sense wires is 8.33 mm.

There are two guard wires made of 100 μm gold-plated stainless steel on either end of the cell for shaping the electric drift field and equalizing the gains on the sense wires. Potential wires (100 μm gold-plated stainless steel) are placed between the sense wires to control the gain of the sense wires, reduce the signal coupling between adjacent sense wires, and reduce the electrostatic deflection of the sense wires. With zero charge on the potential wires the electrostatic deflection of the staggered sense wires is about 72 μm in the middle. This deflection can be almost completely canceled by putting sufficient voltage on the potential wires. This provides a configuration with very stable wire positions but also results in a reduced drift electric field which may not be optimal for achieving saturated drift velocity and small Lorentz angle. We plan to operate the chamber with reduced but not canceled electrostatic deflection The signal coupling between adjacent sense wires is about 7%. (It would be 17% without the potential wires) The potential wires and guard wires are tensioned to have the same gravitational sag as the sense wires.

The field wires have 4.16 mm spacing and are 175 μm diameter beryllium-copper. The end wire has a larger diameter (400 μm) in order to keep the field below 17.5 kV/cm on the surface of the wire to prevent whisker growth. The maximum voltage on the field wires for normal operation is -4.5 kV. The distance between the field wires and sense wires is 3.3 cm in the middle of the cell.

2. Overall Design

The drift chamber consists of twelve concentric cylindrical layers of cells. Alternate layers have their wires parallel to the cylinder axis or at $\sim \pm 3.5^\circ$ to the cylinder axis to provide stereo information. The active length of the chamber is 2.30 m. The overall chamber layout is shown in Fig. 3.2 and the design parameters are given in Table 3.1. There will be a total of 5832 sense wires and 72 samples for dE/dx for tracks traversing the full radial extent of the chamber.

3. Electric Field Uniformity

The uniformity of the electric field in a cell can be seen in Fig. I.1 which shows the drift trajectories [I.1] of electrons produced uniformly along a particle path. A 5 kG magnetic field is used. The drift trajectories are very straight resulting in a linear time-distance relationship. Only one side of each endmost sense wire shows appreciable deviation from linearity, and corrections on the order of 2 ns (100 μm) will need to be made in these regions. This good linearity helps provide good accuracy in both the determination of the track location and the dE/dx measurement and ease of pattern recognition.

4. Position and Momentum Resolution and dE/dx Measurement

We expect to measure positions from drift times to an accuracy of 200 μm or better. The position resolution is determined principally by details

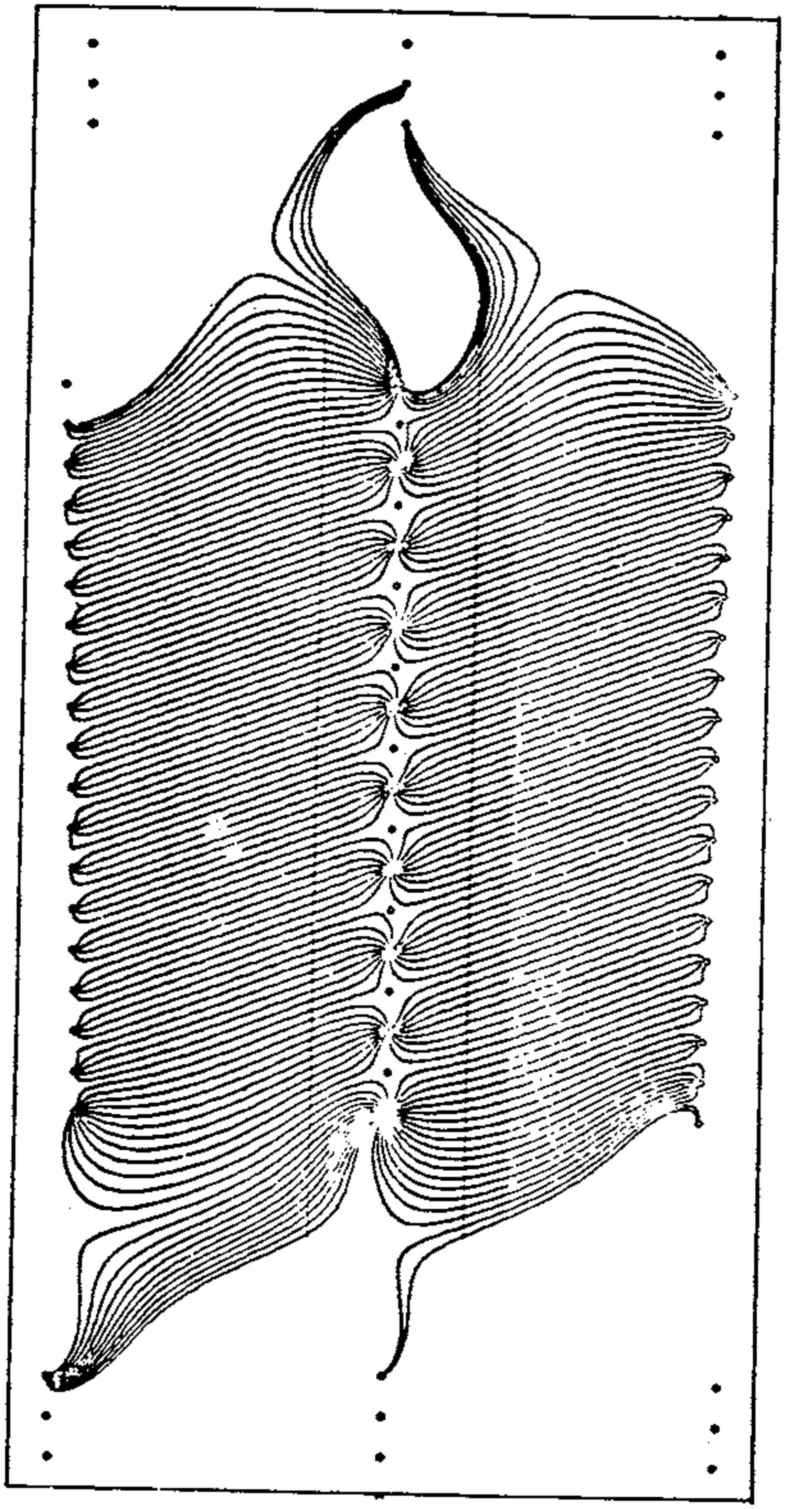

Figure I.1 Drift trajectories of electrons in the drift chamber cell in a 5 kilogauss magnetic field. 1.IP "Figure I.2" Wire stringing scheme for cylindrical drift chamber.

of the electron drift in the gas. We are placing the requirement on our wire positioning accuracy and electronics design that other statistical and systematic contributions to the momentum and position resolutions be small relative to the effect of the above drift time error.

The expected momentum and angular resolutions are shown in Fig. 3.3a and 3.3b and discussed in the main body of the proposal.

For most tracks we expect to measure dE/dx on the basis of pulse heights from 72 samples of 8.33 mm size. The expected performance in terms of charged particle identification capability is discussed in the proposal

5. Gas

We expect to use the gas 89% argon/10% CO_2/1% methane which is used by HRS and Mark III. We plan to run at a gain of 5×10^4 and at a drift electric field of 900 V/cm at which the drift velocity of this gas is saturated.

6. Construction

The wires will be strung between 2-inch aluminum endplates. The endplates will be prestrained to keep the wire tension uniform. They will be held apart by a 2 mm thick beryllium inner cylinder and by a 1/2-inch cylindrical aluminum shell with 1/4-inch panels.

All the wires in one row in a cell are positioned by a one-piece Delrin feed-through, shown in Fig. 1.2. Holes to locate the feed-throughs will be accurately milled in the endplates. The wires are located in machined notches along one side of a central slot, tensioned, and soldered to a printed circuit board attached to the Delrin. We expect to locate wires to ±35 μm. Sources of errors in wire location are the following: feed-through accuracy in machining and placement--15 μm, error in endplate machining

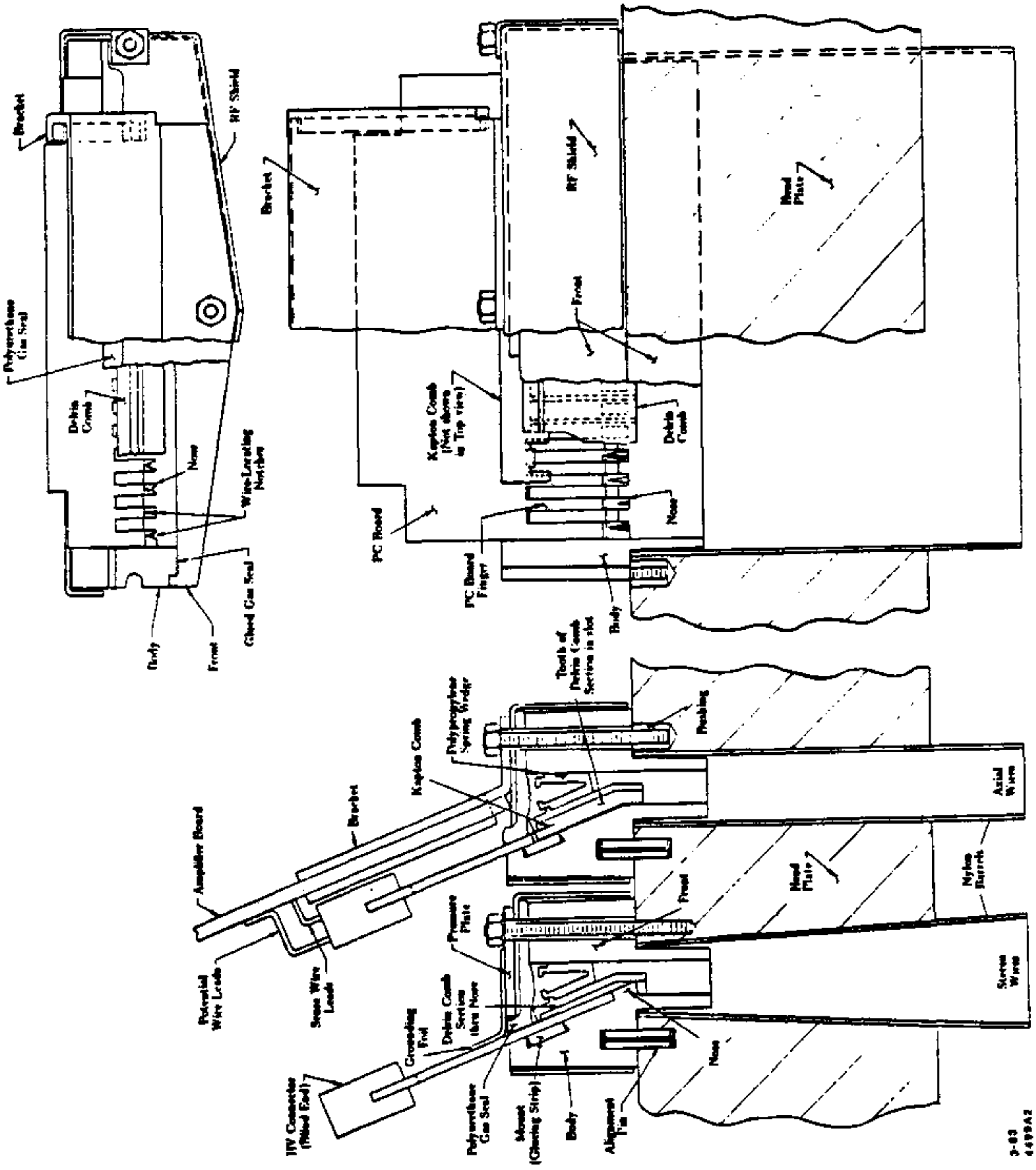

Figure I.2 Wire stringing scheme for cylindrical drift chamber.

and placement--25 μm, and error in wire sag and electrostatic deflection–10 μm. The open slot in the feed-through permits the wires to be strung in groups, allows access for replacement of single wires, if necessary, and provides for visual inspection of the interior. Replacement of wires after the chamber is built can be accomplished by attaching them to a field or potential wire which can be used to pull the wire through the chamber. The feed-through has a cap which is attached with a gasket to form a gas seal. Electrical connections to the wires are made through the printed circuit board.

7. Prototyping

Prototyping efforts are being carried out at SLAC and at U.C. Santa Cruz. A single-cell full-length prototype is being tested at SLAC. Accuracy of location and tensioning of wires, electrostatic properties, pulse shapes, position resolution, and high voltage connections are being investigated. We are building a multi-cell prototype which will be tested in a beam to study the calibrations and corrections needed for dE/dx measurements.

8. Schedule

We plan to start stringing wires in the final chamber in the fall of 1983. The drift chamber will be installed in the Mark II detector at PEP in the summer of 1984. It will be extensively tested and used for data taking at PEP prior to installation at the SLC.

B. Electronics Design

Electronics for the drift chamber must measure drift time and energy loss for multiple tracks without degrading the intrinsic measurement properties of the cell design. Accordingly, we have specified for each electronic channel: time measurement accuracy of 1 nsec RMS (~ 50 μm), energy loss measurement better than 10% RMS (compared with more than 25% from ionization cluster statistics), and multi-hit separation for signals separated by less than 70 nsec (~ 3.5 mm). In addition, we have specified that systematic electronic effects in the energy loss measurement be less than 1%. Finally, this electronics will conform to the existing Mark II trigger and data acquisition architecture. Figure I.3 a block diagram of the electronics system.

1. Front-End Electronics

Low-noise preamplifiers will be mounted and shielded directly on the chamber endplate. This location affords improved signal-to-noise performance with respect to both intrinsic detector noise and environmental noise. Optimal signal-to-noise performance is important to operation with low chamber thresholds at relatively low gas gains. In addition, resistive-coupling networks between sense wires accurately compensate neighboring channels for signals induced on the corresponding neighboring sense wires. Finally, pole-zero filters cancel the 1/t tail of the signal due to positive ion drift, facilitating multiple track measurements. Additional electronics mounted on the magnet flux return contains signal splitters, discriminators for time measurement, and shapers for dE/dx measurement.

2. Drift Time Measurement—TDC Modules

For the drift time measurement we have chosen a digital measurement technique. The digital approach facilitates multi-hit measurements and

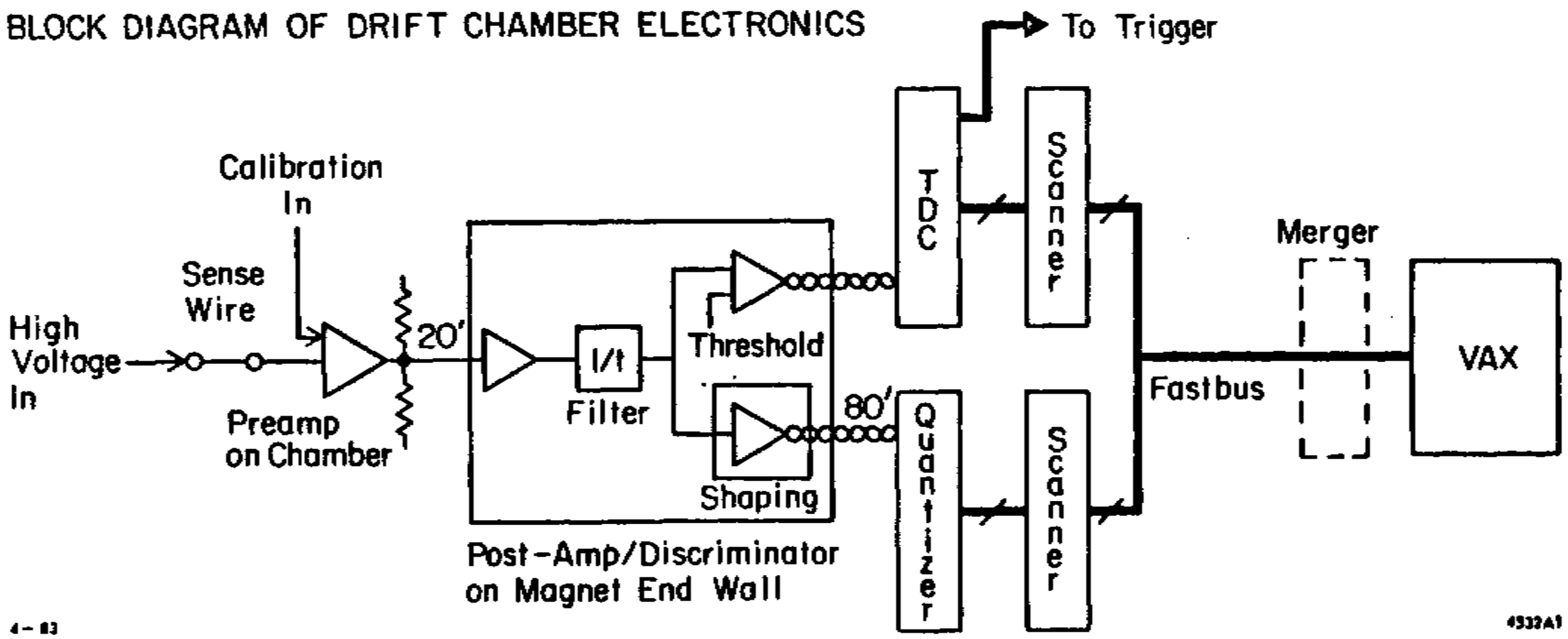

Figure 1.3 Block diagram of drift chamber electronics.

provides an extremely linear and easy-to-calibrate system. High resolution in the digital measurement is provided by a new device—a 250 MHz 256-bit shift register (RCA TCS 192 developed by E. D. Platner of BNL for the MPS II detector). Our application of this device provides 2 nsec bin width which, together with the small differential non-linearity intrinsic to the device, provides RMS resolution of about 1 nsec. The shift register also stores the time measurement until readout.

3. Energy Loss Measurement—Quantizer Modules

For the energy loss measurement we have chosen to use high-speed quantizers (flash ADCs) which digitize the analog waveforms several times throughout their duration. The output data of the quantizers are stored in shift registers (TCS 192) used as high-speed memories. This approach provides multi-hit capability, even for closely spaced tracks; moreover, it measures the time of the hit, facilitating association of each energy loss measurement with its drift time measurement. We are currently studying various prototype systems in order to determine the required sampling frequency and pulse height resolution.

4. Readout Electronics--Scanner Preprocessor Modules

Readout of the TDCs and quantizers is performed by modules which execute a sparse data scan, apply calibration corrections, format the data to conform to the Mark II software structure, and store the reduced data until block transfer to the host VAX computer. Readout by the scanner-preprocessor modules is in parallel via FASTBUS with one scanner-preprocessor per approximately 2000 TDC channels and per 500 quantizer channels. Readout into each scanner-preprocessor memory requires approximately 2 msec/event. Conforming to the new FASTBUS standard reduces cost, improves reliability, and enables rapid readout of long data streams. In addition, it will facilitate further preprocessing of the data, such as on-line association of the drift time and energy loss measurement, slewing corrections, and waveform fitting.

5. Design, Prototypes, and Testing

Electronics is being studied on a full-length prototype chamber. Presently, we are studying the suitability of various preamplifier designs. A commercially available TDC module (LeCroy 1879) is being evaluated for the drift-time measurement. A prototype quantizer module is being debugged prior to test on the chamber. Meanwhile, the concept of dE/dx measurement by waveform sampling is being examined by using currently available comparators and TDCs and by using a transient digitizer. Conceptual designs have been prepared for the scanner-preprocessor modules; however, detailed design work awaits selection of TDC and quantizer modules.

The front-end electronics is being developed by U.C. Santa Cruz with engineering help from SLAC. The quantizer modules are being designed at LBL. The scanner-preprocessor modules are being designed at SLAC along with trigger, calibration, test, and high voltage systems. Final prototypes and system evaluation will be complete by the end of Fiscal Year 1983. Production will begin at that time, with delivery complete by spring 1984. The final six months before summer 1984 installation at PEP will be used for thorough module and system check-out.

APPENDIX II

DETAILS OF LIQUID ARGON CALORIMETERS

The liquid argon calorimeters, shown in Fig. 1.1, have been in use since the early SPEAR running in 1978. Their performance has been excellent and they have greatly enhanced the physics analyses of the Mark II group. Operation of the modules has been smooth and reliable--at no time have we had to remove a module from the detector.

The modules are sandwiches of 2 mm thick Pb (.36 rl) sheets and 3 mm gaps filled with liquid argon. Alternate lead planes are divided into strips to allow spatial localization of showers. There are eighteen cell groupings and the device is 14 rl thick. Preceding the lead assembly is a pair of "massless trigger gaps" which allow discrimination between photons which convert before the shower counter and those which do not. These gaps are larger (8 mm) and run at a higher potential.

The trigger gap strips, which measure the azimuthal coordinate φ, are 3.7 cm wide. The eighteen layers of lead strips are ganged to provide six samples in depth, although the first four samples are interleaved. There are three groups of φ strips, two of ϑ and one at 45°, called U. Fig. 3.6 shows the layout of the modules (a) as well as the arrangement of these strips in depth and the ganging scheme (b). There are 362 electronic channels per module.

A calibration system injects charge onto capacitors (one per channel) which are mounted inside the modules as close to the signal pickoff point as possible. In this way the integrity of the signal collection hardware can be checked and the gain of the electronics can be measured. Liquid argon shower counters operate as ionization devices and hence there is no amplification in the device itself. Therefore, as long as variations in the electronic gains can be reliably monitored, the overall system will have a stable energy scale. In normal operation the electronics are calibrated three times a day and variations in the overall energy scale are kept below ½%.

Fig 3.5 summarizes the response of the modules to charged tracks. One sees small (6%) azimuthal dead space due to module boundaries. The modules cover the range of $\cos\vartheta < 0.68$. The energy resolution has been measured using Bhabhas at SPEAR and PEP. Fig. 3.7a shows the response of the modules to 2 GeV Bhabhas. The broadening on the lower side is due to radiative effects. The resolution obtained from Fig. 3.7a is $\sigma_E / E = 14\% / \sqrt{E}$. It is well documented that the resolution is proportional to $\sqrt{t}$ where t is the thickness of the radiator. The Bhabhas in Fig 3.7a have the average angle of 40°; removing this effect, one gets $\sigma_E / E = 12\% / \sqrt{E}$ at normal incidence for 2 GeV electrons. Fig. 3.7b shows the response of the modules to 14.5 GeV Bhabhas at PEP. The curve corresponds to a resolution of $14\% / \sqrt{E}$. Again, correcting for the angle of incidence, one finds that $\sigma_E / E = 12\% / \sqrt{E}$ for normal incidence and 14.5 GeV electrons. Fig. II.1 shows the energy response of the 8 modules "folded out" in φ for PEP events containing two collinear charged prongs. One readily sees the uniformity of energy response as well as the clear distinction between the $\mu^+\mu^-$ and e^+e^- events.

Fig. II.2a shows the gamma-gamma invariant mass spectrum for events at SPEAR which contain two charged particles and two photons. Fig. II.2b shows the gamma-gamma invariant mass spectrum for photons in events which have been selected by a kinematically fit to the hypothesis $J/\psi \rightarrow \pi^+\pi^-\pi^\circ$ and $J/\psi \rightarrow 2\pi^+2\pi^-\pi^\circ$. These plots give a mass resolution $\sigma_m / m = 15\%$.

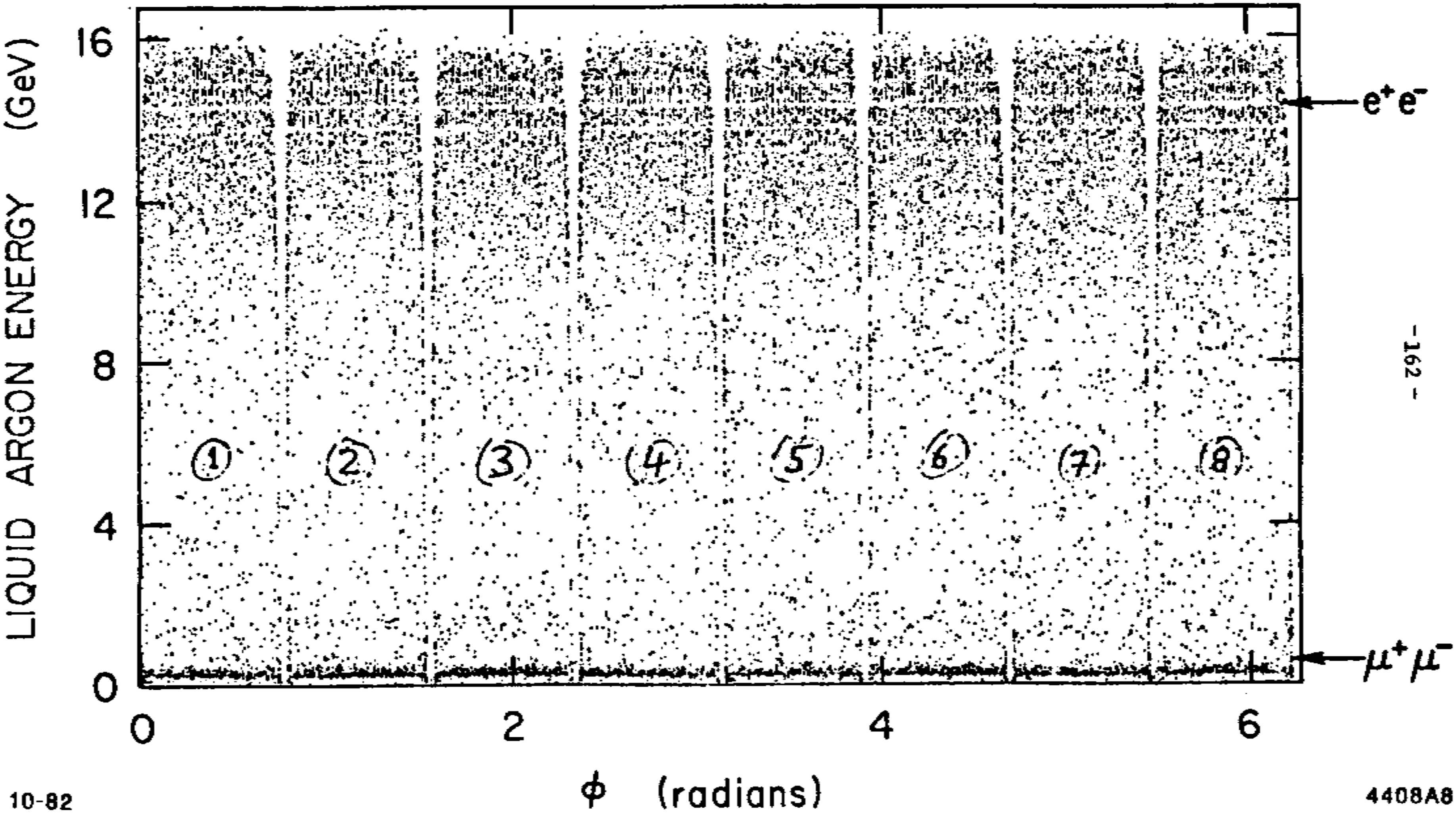

Figure II.1 Energy response of the liquid argon calorimeter modules for PEP events containing two collinear charged prongs.

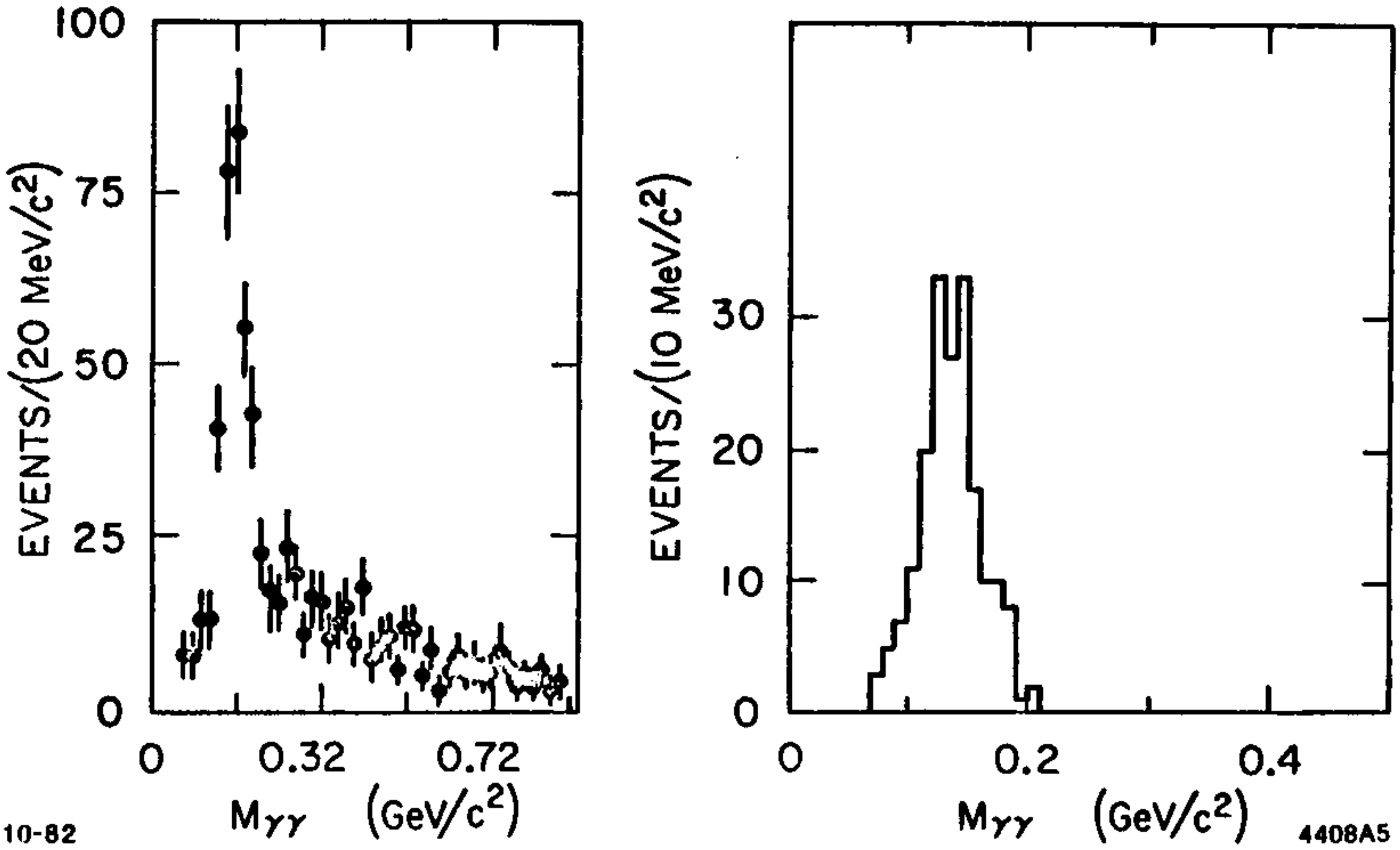

Figure II.2 Gamma-gamma invariant mass for a) events with two charged particles and two photons; b) events selected by kinematical fit $J/\psi \rightarrow \pi^+\pi^-\pi^0$ and $J/\psi \rightarrow 2\pi^+2\pi^-\pi^0$

For high energy (>10 GeV) electrons, leakage out the back of the 14 rl modules becomes sizable. The leakage at 50 GeV is 8.5% and the fluctuation of this leakage is ±40%. Hence, without correction one would get an effective resolution from leakage alone of $\gtrsim 10\%/\sqrt{E}$. Because of the fine sampling in the liquid argon modules, we are able to correct for the leakage by using the simple algorithm $E_{\text{leak}} = A_{\text{leak}} \times E_7$ where E_{leak} = lost energy. E_7 is the energy in the last liquid argon layer and A_{leak} is a constant. Fig. 3.8a shows the simulated (EGS) response of a module to 50 GeV electrons where no leakage correction has been applied. The calculated resolution for this data is $\sigma_E/E = 22\%/\sqrt{E}$. Fig. 3.8b shows the same data corrected with the simple algorithm. Its calculated resolution is $\sigma_E/E = 14\%/\sqrt{E}$. A more complicated algorithm would presumably do better. We include this example to substantiate our claim that for very high energy electrons we expect a resolution $< 15\%/\sqrt{E}$. The angular resolution and hadron rejection properties of the modules are given in the main body of the text

APPENDIX III

BEAM-INDUCED BACKGROUNDS AT SLC

A. Synchrotron Radiation (SR) from Nearby Insertion Quadrupoles

1. Incident Beam

The SR resulting from incident beam bunches traversing the insertion quadrupoles (Q1-Q5) has relatively low intensity, and is limited in size by the maximum angle of the incident beam, 0.3 mrad. Consequently nearly all of the SR from the incident beam produced by Q1-Q3 passes through this triplet in which it is produced without striking any apertures. However, some of the SR produced by the Q4, Q5 doublet at $|Z| \simeq 20$m strikes the aperture limits in and around Q1-Q3, mostly on the opposite side of the IP from where produced, resulting in ~4 γ's is only about 30 keV, however, and this background is not expected to be a problem.

2. Disrupted Beam

The bunch-bunch collision processes can create angular excursions up to about 2.2 mrad in the $e^{\pm}$ trajectories, which then enter the Q1-Q3 triplet at a relatively large radius, resulting in intense SR. For the predicted angular distribution for disrupted beams, a program has calculated a produced flow of 2×10^{12} γ's with an average energy of ~1 MeV each. With the apertures adjusted as in Fig. 5.1b, there should be no γ's striking the beam pipe until about $|Z| \sim 20$m. After putting in the attenuation factors due to solid-angle and scattering, the number of γ's entering the detector is of order one per crossing. Again, this presents no obvious difficulty.

B. SR from Bending Magnets

Referring to Fig. 5.1a, we see the limits drawn for the SR being emitted from the beam trajectories in the hard and soft bend dipole magnets. The mask M1 is arranged to intercept all the hard bend SR, which is a critical energy ~1 MeV (at $E_{beam} = 50$ GeV). Here there will be some giant resonance neutrons produced by the tail of this SR distribution ($E_\gamma \gtrsim 10$ MeV). The SR from the soft bends BS_1 through BS_4 have critical energies about 60-80 keV.A total of about 5×10^{10} γ's are generated in BS_1, as an example. The mask M2, located at $|Z| \sim 2$m, is relatively thin and is intended to collimate these γ's. Some of this SR will inevitably pass through the mask M2 closer to BS_1, and, after passing through the detector, will strike the corresponding mask M2 on the opposite side of the IP, and perhaps also the front of Q1 on that side. It is hoped that by moving M2 close enough to the beam in the horizontal direction, this SR can be intercepted to avoid hitting Q1. SR back-scattered from M2 will have to subsequently scatter at least once more in order to enter the detector. Even so, there will be an estimated 250 low-energy γ's which will scatter into the space just outside the beam pipe for the minimum M2 aperture limit of 5 mm. It should be noted that this fan of SR exists only on the outer wall of the beam pipe, in the horizontal plane, and that M2 may be a movable mask so that it can be optimally positioned.

C. Beam-Gas Bremsstrahlung (BGB) and Coulomb Scattering (CS)

A recent study [1.2] of the BGB process indicates that occupancy per crossing at the detector may be comparable with that experienced at PEP. Even though the charge per bunch in the SLC design is about 1/5 that in PEP recently, the SLC beam optics and aperture sizes are such that this advantage is overcome. There is a calculated beam pipe occupancy of 15-20% at PEP for $|Z| \lesssim 5$m, which is reduced to ~1% in the Mark II by masking. A similar beam pipe occupancy is expected at SLC for an assumed vacuum of 5×10^{09} Torr. Coulomb scattering is estimated [1.3] to be a small fraction of the beam-gas scattering. The detector is well shielded from the beam pipe by the quadrupoles themselves and by their supporting pipe, so that the background suppression is expected to be as effective as at PEP.

D. Beamstrahlung

The flux of energetic γ-rays resulting from individual $e^{\pm}$ radiating in the intense magnetic field of the opposing bunches has been named "beamstrahlung". These very hard γ's are characterized by critical energies ~300 MeV. As discussed in the SLC Workshop Report [1.1] (pp 576, 580-583), the aperture of the nearby quadrupoles (Q1-Q3) is designed large enough to pa[ss unobstructed the largest angle γ-ray trajectory resulting from beamstrahlung (see Fig. 5.1b). These γ's ultimately exit from the beam pipe at $|Z| \sim 20$m. With the present geometry, we estimate that about one γ per crossing of ~0.5 MeV energy will enter the detector

E. Neutron Production

A background source not yet examined in any detail is that of neutrons resulting from giant resonances, induced primarily by the SR from the strong bending magnet B1 striking the back of the mask M1 (see Fig. 5.1a). The tail of this SR energy distribution extends above 10 MeV exciting these resonances. Neutrons of a few MeV energy are emitted The Conceptual Design Report for SLC estimates ~1000 neutrons per crossing enter the detector, and as few as 10 with sufficient shielding (see pp. 176-181 of Ref. 1.4).

We cannot be certain about the effect of this neutron flux on the detector since it is a phenomenon not seen at SPEAR or PEP. The fraction of neutrons detected in the calorimeters will be very small due to the very short range of the low energy recoils. If we assume $T_n \simeq 5$ MeV, or $P_n \simeq 100$ MeV/c, the resulting range in Pb of a proton that takes the full recoil momentum from an n-p collision is 100 mg/cm^2 or ~0.1 mm. In the drift chamber, proton recoils could go as far as 30 cm. Since the recoil momentum will be much less, on the average, and nuclear fragments, rather than p recoils, may emerge, the actual ranges will be much less. The collision cross section in gas is such that about 1% of the neutrons will interact inside the drift chamber.

References

[1.1] Proceedings of the SLC Workshop on Experimental Use of the SLAC Linear Collider, SLAC-PUB-247.

[2.1] A. Ali et al., *Phys. Lett.* 93B (1980) 155.

[2.2] C. Peterson et al., SLAC-PUB-2912 (1982).

[2.3] J. M. Dorfan, *Z. Phys.* C7 (1982) 349. See also SLAC-PUB-2813.

[2.4] The procedure outlined in the text does not include the effects of interacting pions. This is a small effect relative to the main problem of photons overlapping charged particles.However, since we have measured the impact of interacting pions at PEP, we have added this contribution (typically 0.005) into the misidentification numbers quoted in Table 2.3.

[2.5] J. D. Bjorken, SLAC Summer Institute 1976, SLAC-198.

[2.6] G. Ekspong and K. Hultqvist, Stockholm preprint, USIP 82-05 (1982).
G. Barbiellini et al., DESY 79/27 (1979).
J. Finjord, *Physica Scripta* 21 (1980) 143.

[2.7] J. Smith, J. A. M. Vermaseren, and G. Grammer, *Phys. Rev.* D15 (1977) 3280.

[2.8] E. Ma and J. Okada, *Phys. Rev.* D18 (1978) 4219.

[2.9] K. J. F. Gaemers, R. Gastmans, and F. M. Renard, *Phys. Rev.* D19 (1979) 1605.

[2.10] D. A. Dicus, *Phys. Rev.* D21 (1980) 1767.

[2.11] G. Barbiellini, B. Richter, J. L. Siegriest, *Phys. Lett.* 106B (1981) 414.

[3.1] J. Va'vra, SLC Note CN-12

[3.2] M. Atac, et al., *Nucl. Inst. and Meth.*, 205 (1983) 113.

[3.3] Santa Cruz Group – Private Communication

[3.4] M. Nelson, et al., SLAC-PUB-3059

[3.5] K. Winter, et al., *Nucl. Inst. and Meth.* 157, 35 (1978).

[1.1] L. Roberts and J. Va'vra. "A program to calculate electrostatics and ion trajectories in drift chambers."

[1.2] J. A. J. Matthews, SLC Note CN-197.

[1.3] G. Fischer, "SLC Backgrounds from Collider Arc."

[1.4] SLAC Linear Collider Conceptual Design Report, SLAC-223, 1980.